Semiconductors, Vol. 35, No. 12, 2001, pp. 1347–1354. Translated from Fizika i Tekhnika Poluprovodnikov, Vol. 35, No. 12, 2001, pp. 1409–1416.

ELECTRONIC AND OPTICAL PROPERTIES OF SEMICONDUCTORS

Paramagnetic Defects in Silicon Carbide Crystals Irradiated with Gamma-Ray Quanta

I. V. Ilyin*, E. N. Mokhov, and P. G. Baranov

Ioffe Physicotechnical Institute, Russian Academy of Sciences, Politekhnicheskaya ul. 26, St. Petersburg, 194021 Russia

** e-mail: Ivan.Ilyin@pop.ioffe.rssi.ru*

Submitted March 20, 2001; accepted for publication April 2, 2001

Abstract—The results of the first observations of paramagnetic defects in SiC crystals irradiated with gamma-ray quanta are reported. Three types of defects, designated as γ1, γ2, and γ3, were detected in irradiated 4*H*-SiC:Al and 6*H*-SiC:Al crystals using electron spin resonance (ESR) measurements. All these centers have almost the same parameters of the spin-related Hamiltonian with $S = 1/2$ and feature an appreciable anisotropy of the *g*-factors. The γ1 centers are almost coaxial with the local *z*-axis oriented approximately along one of the directions of the Si–C bond that does not coincide with the *c*-axis. The γ2 and γ3 centers have a lower symmetry, although the orientation along the above bonds is clearly pronounced. The values of the largest *g*-factor (g_z) decreases in the sequence from γ1 to γ3. The γ1 signal can be detected at temperatures of 3.5–15 K; the γ2 and γ3 signals are detectable at temperatures of 10–35 and 18–50 K, respectively. The hyperfine interaction of an unpaired electron in the γ1 center with a nucleus of the ^{29}Si isotope is detected for certain orientations of the crystal. The γ1, γ2, and γ3 centers cease to exist at a temperature of 160°C; it is concluded that the ESR signals of these centers are related to defects in the C sublattice. It is assumed that the γ1, γ2, and γ3 centers have a common origin and are related to the low-temperature (γ1) and high-temperature (γ2 and γ3) modifications of the same center. The models of a defect in the form of either a carbon vacancy or a complex incorporating an Al impurity atom and a C atom that occupies the silicon site or interstice are discussed. © *2001 MAIK "Nauka/Interperiodica".*

1. INTRODUCTION

In recent years, interest in silicon carbide (SiC) has been growing. This is related to the need for the development of electronic and optoelectronic devices that can operate at high temperatures, high power, and high radiation levels. A large Si–C bond energy renders SiC stable against high temperatures, aggressive media, and ionizing radiation. Since the diffusivity of the majority of impurities in SiC is low, ion implantation is mainly used to dope this material. Radiation defects formed in SiC during ion implantation are stable at room temperature (in contrast to those in Si); some types of secondary radiation defects are stable at temperatures higher than 2000°C. All this stimulated the initiation of numerous studies concerned with radiation defects in SiC.

Electron spin resonance (ESR) is the most informative method for studying the structure of radiation defects; this has been most clearly demonstrated by identifying the structure of the main radiation defects in silicon in classical studies performed during the last 40 years [1]. The history of using ESR to study the radiation defects in SiC is much less impressive; nevertheless, the structure of a number of native defects in SiC, such as the silicon vacancy or various types of divacancies, has been established quite reliably [2–11]. It is important to emphasize that all the above studies have been concerned with SiC irradiated with electrons, neutrons, or protons. Such irradiation simulates the ion implantation used in production of electronic devices. The challenge is related to the fact that, in the course of ion implantation, defects are formed in a thin (less than 1 μm thick) surface layer; as a result, the sensitivity of traditional ESR is not sufficiently high to detect these defects. As far as we know, there have been no publications in which the detection of paramagnetic radiation defects in SiC crystals irradiated with gamma-ray quanta has been reported. At the same time, gamma-ray irradiation is the most penetrating and, as such, affects to a great extent the various electronic devices under actual conditions of their applications. It is also known that this irradiation easily produces numerous radiation defects in silicon, and this introduces great difficulties in the production of radiation-resistant electronic devices. It should be emphasized that gamma-ray irradiation, in contrast with other types of irradiation, produces defects that are distributed uniformly over volume; this appreciably enhances the reliability of the results of studying these defects because there is no nonuniformity in the distribution of the defects over the crystal bulk.

In this paper, we report for the first time the observation of the radiation-defect ESR spectra in the *p*-4*H*- and *p*-6*H*-SiC crystals doped with aluminum and irradiated with gamma-ray quanta.

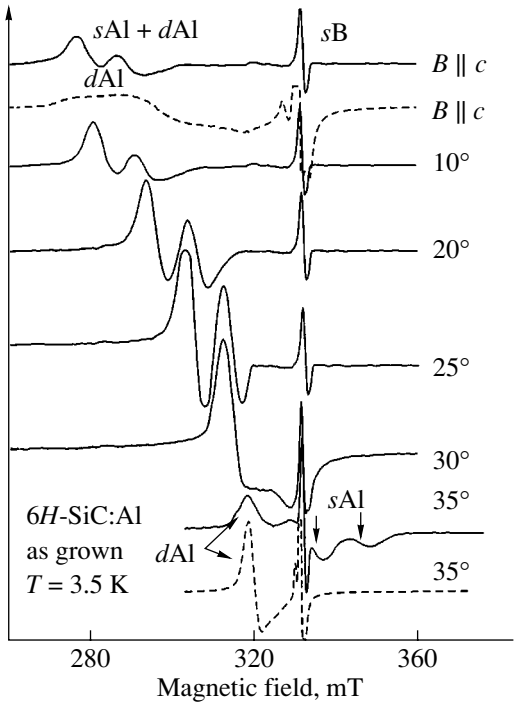

Fig. 1. The electron spin resonance (ESR) spectra measured at 4 K in an unirradiated 6*H*-SiC:Al crystal for several orientations of the crystal with respect to the magnetic field *B* in the $\{11\bar{2}0\}$ plane (the corresponding angles are indicated at the curves). The designations of *s*Al, *d*Al, and *s*B are introduced for the shallow Al level, deep Al level, and shallow B level, respectively. The dashed lines correspond to the ESR spectra in a 4*H*-SiC:Al crystal with an increased Al concentration; for this crystal, the ESR signals related to the shallow Al level were almost not observed. Vertical arrows indicate an additional superfine structure.

2. EXPERIMENTAL

We studied *p*-4*H*- and *p*-6*H*-SiC crystals doped with aluminum and grown by the sandwich-sublimation method at a temperature of 2150°C [12] and at a growth rate of 0.8 mm/h. We also studied commercial 6*H*-SiC crystals produced by the Cree Corporation. The aluminum concentration was about 10^{17} cm^{-3} in all the crystals that were subjected to gamma-ray radiation for two weeks. The gamma-ray source was the ^{60}Co isotope with the gamma-quantum energy of 1.12 MeV and the integrated flux of 10^{13} cm^{-2}. The 4*H*- and 6*H*-SiC crystals in the shape of platelets with the plane perpendicular to the hexagonal *c* axis were oriented to be rotated in the $\{11\bar{2}0\}$ and {1100} planes. The experiments were performed using a Jeol ESR spectrometer at a frequency of 9.2 GHz; the samples were installed in a laboratory-made flow-through helium cryostat, which made it possible to vary temperature in the range of 4–300 K. All the ESR spectra were recorded without signal accumulation and resulted from a single scan.

3. RESULTS

The ESR signals corresponding to the shallow- and deep-level aluminum acceptors and the shallow-level boron acceptors were observed in the studied 4*H*- and 6*H*-SiC crystals [13–17]. The shallow Al level is formed by an Al atom that resides at the Si site with regularly arranged neighbors [13, 14]; in our opinion, the deep Al level is related to a complex that consists of an Al atom at the Si site and a C vacancy at the nearest site along the *c* crystal axis [14, 16, 17]. Boron is an uncontrolled impurity and commonly manifests itself in the ESR spectra of *p*-SiC crystals as a shallow B level; however, for high Al concentrations on the order of 10^{19} cm^{-3}, the ESR signals related to the deep B level are also observed [16]. In Fig. 1, we show the ESR spectra observed in a 6*H*-SiC:Al (Cree) crystal before gamma-ray irradiation and recorded for several orientations of the crystal with respect to the magnetic field. The signals related to the shallow Al level and designated as *s*AL, the deep Al level (*d*Al), and the shallow B level (*s*B) are distinguishable in the spectra. Both signals overlap at a low temperature (≈4 K) for the magnetic-field orientations close to the *c*-axis ($\theta = 0°$); in contrast to this, for $\theta = 35°$, these signals are observed in different magnetic fields owing to dissimilar values of the *g*-factors. For the orientation with $\theta = 35°$, a poorly resolved hyperfine structure (HFS) can be observed in the *d*Al signal; this structure originates owing to the interaction of an unpaired electron with the ^{27}Al isotope nucleus [14]. In the studied crystals, the intensities of the *s*Al ESR signals are comparable to or exceed those of the *d*Al; therefore, the ESR spectra observed for a 4*H*-SiC crystal doped heavily with Al (the Al concentration $\approx 5 \times 10^{19}$ cm^{-3}) [16] are also shown in Fig. 1 (see dashed lines for the orientations of $\theta = 0°$ and $\theta = 35°$). In this crystal, the intensities of the *d*Al ESR signals are higher by more than two orders of magnitude than those of *s*Al signals; as a result, only the *d*Al signal is distinguishable in the spectrum for the $\theta = 0°$ orientation. For such crystals, electron–nuclear double resonance (ENDOR) has been used to establish uniquely that the ESR signals are related to Al [17]; the ENDOR data are consistent with the magnitude of the hyperfine interaction observed in the ESR spectra.

The ESR spectra were observed at a temperature of 7 K in a gamma-irradiated 4*H*-SiC crystal and recorded for different orientations of the crystal in a magnetic field. The field was rotated in the $\{11\bar{2}0\}$ crystallographic plane. In addition to the *s*B signals (on the right), an ESR line is distinguishable in the spectrum recorded for the $B \parallel c$ orientation and shown in Fig. 2; this line splits into four lines if the sample is rotated in the $\{11\bar{2}0\}$ plane. This splitting indicates that the paramagnetic defect has several equivalent orientations in the SiC lattice. The directions of the local symmetry axes for the center can be determined from the extrema in the angular dependence of ESR signals. In Fig. 2, one

of such extremum is observed for an angle of the magnetic field with the *c*-axis of the crystal close to 70°. In SiC, the angle θ = 70° corresponds to the angle between the *c*-axis and the direction of the Si–C bonds. Thus, this center has a specific local axis directed approximately along the Si–C bonds, which are not oriented along the *c*-axis of the crystal. It is notable that the intensity of the ESR signal decreases drastically in the lowest magnetic fields for the angles close to θ = 70°. There are, in total, six magnetically nonequivalent directions in hexagonal crystals, whereas only four such directions exist in the $\{11\bar{2}0\}$ plane. For the $B \parallel c$ orientation, all these directions are equivalent; as a result, a single ESR line is distinguishable in the spectrum. We also observed similar ESR signals in the 6*H*-SiC crystals.

Three different types of signals were detected in the ESR spectrum of crystals of both polytypes (4*H*- and 6*H*-SiC) subjected to gamma-ray irradiation. The temperature dependence of the ESR signals observed in a 4*H*-SiC crystal with the $B \parallel c$ orientation can be deduced from the spectra shown in Fig. 3. It can be seen that the signal denoted by γ1 is observed at temperatures of 4.5–15 K, the second signal (γ2) is distinguishable in the range of 10–35 K, and the third signal (γ3) is observed at temperatures of 18–50 K. Thus, the γ1 and γ2 signals are observed simultaneously in a comparatively narrow temperature range of 10–15 K, whereas both the γ2 and γ3 signals are observed in a wider range of 18–35 K. In addition, it should be noted that the linewidths of the γ1 and γ2 signals increase substantially before the disappearance of these signals (Fig. 3), whereas the positions of the ESR lines remain almost unchanged.

Angular dependences of ESR signals for the γ1, γ2, and γ3 centers in the (a) 6*H*-SiC and (b) 4*H*-SiC crystals are shown in Fig. 4. It is noteworthy that the crystals were rotated in different planes: in the $\{11\bar{2}0\}$ plane for 4*H*-SiC and in the {1100} plane for 6*H*-SiC. The symbols *1*, *2*, and *3* are used to represent the experimental angular dependences for the γ1 (measured at 7 K), γ2 (at 23 K), and γ3 (at 34 K) centers. These dependences can be described using the following spin-related Hamiltonian with the spin $S = 1/2$:

$$H = \mu_B(g_x H_x S_x + g_y H_y S_y + g_z H_z S_z).$$

Here, μ_B is the Bohr magneton and g_x, g_y, and g_z are the *g*-factors corresponding to the directions *x*, *y*, and *z* of the local symmetry axes of the center.

The calculated (theoretical) angular dependences of the γ1, γ2, and γ3 signals are plotted in Fig. 4 as the solid, dashed, and dotted lines, respectively. The calculations were performed using the R-Spectr program [18] and the values of the *g*-factors, listed in the table where the values of the Eulerian angles for six magnetically equivalent orientations of each center are also given.

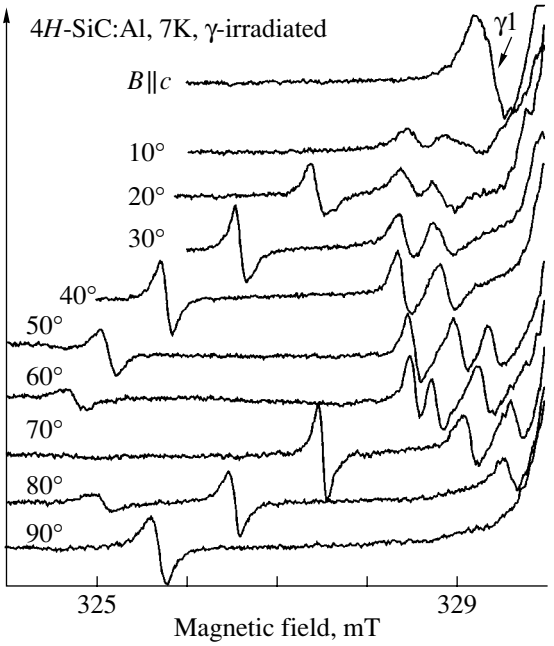

Fig. 2. The ESR spectra observed for a gamma-irradiated 4*H*-SiC crystal at a temperature of 7 K; the spectra were recorded for various orientations of the crystal with respect to the magnetic field *B* (the corresponding angles are indicated at each curve). The magnetic field was rotated in the $\{11\bar{2}0\}$ plane.

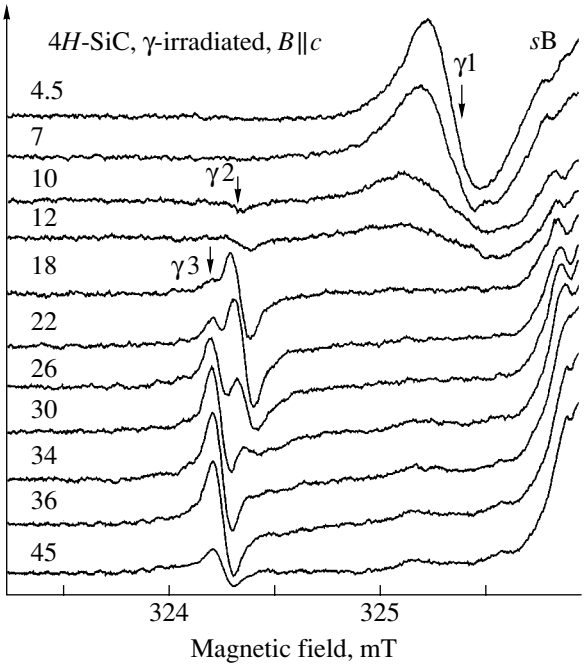

Fig. 3. The ESR spectra measured at various temperatures (indicated at each of the spectra and expressed in K) for a gamma-irradiated 4*H*-SiC sample with the $B \parallel c$ orientation.

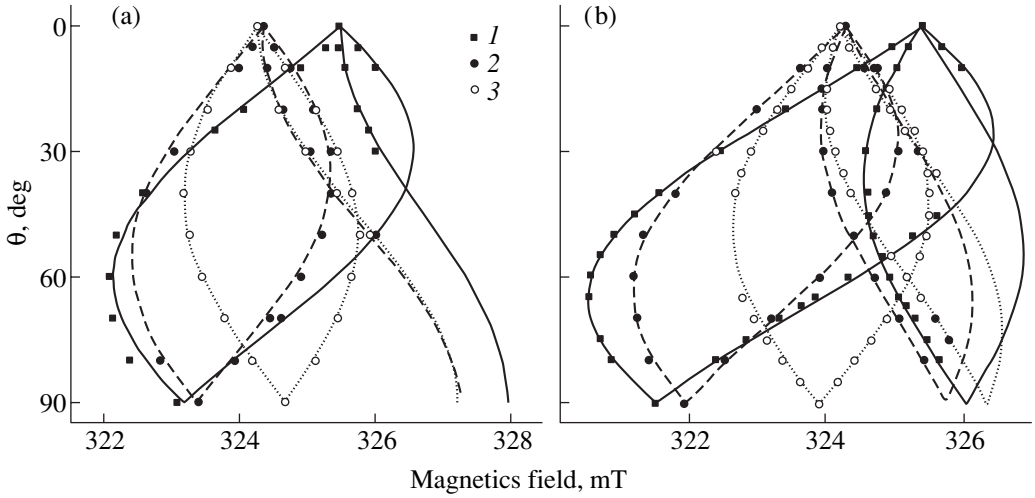

Fig. 4. Angular dependences of ESR signals for the γ1, γ2, and γ3 centers in the (a) 6*H*-SiC and (b) 4*H*-SiC crystals. The crystals were rotated in the $\{11\bar{2}0\}$ plane for 4*H*-SiC and in the {1100} plane for 6*H*-SiC. Experimental angular dependences correspond to (*1*) γ1 (the measurement temperature of 7 K), (*2*) γ2 (23 K), and (*3*) γ3 (34 K) signals. The solid, dashed, and dotted lines represent the results of calculations using the data listed in the table.

When determining the Eulerian angles, we oriented the laboratory reference frame so that its *Z*-axis (henceforth, we use capital letters to denote the axes of the laboratory reference frame) was parallel to the *c*-axis of the crystal, the *X* axis was perpendicular to the *Z*-axis and was lying in the $(11\bar{2}0)$ plane, and the *Y* axis was perpendicular to the $(11\bar{2}0)$ plane. We used the following definition of the Eulerian angles [18]: the first angle α corresponds to a rotation about the *Z*-axis, the second angle β represents a rotation about the new *Y*-axis, and the third angle γ corresponds to the rotation about the new *Z*-axis. Thus, the direction of the *Z*-axis in the laboratory reference frame can be represented by the three Eulerian angles (0, 0, 0). Six magnetically nonequivalent directions along the Si–C bonds, which do not coincide with the *c*-axis of the crystal, are specified in the ideal 6*H*-SiC lattice by the combinations of the following Eulerian angles (α, β, and γ) expressed in the degrees of circle: (0, 110, 0), (120, 110, 0), (240, 110, 0), (0, 250, 0), (120, 250, 0), and (240, 250, 0).

It can be deduced from the values of the Eulerian angles listed in the table that orientations of the γ1, γ2, and γ3 centers are different and do not completely coincide with directions of the Si–C bonds. However, it is evident that all deviations from ideal axes and also the differences between the γ1, γ2, and γ3 centers are comparatively small; therefore, it may be stated that, at the

The ESR signal parameters for the γ1, γ2, and γ3 centers in the gamma-ray irradiated 4*H*- and 6*H*-SiC crystals

	γ1				γ2				γ3			
	4*H*		6*H*		4*H*		6*H*		4*H*		6*H*	
g_x	2.006		2.006		2.015		2.015		2.014		2.013	
g_y	2.000		2.000		2.002		2.000		2.002		2.002	
g_z	2.044		2.041		2.040		2.042		2.036		2.031	
	α	β	α	β	α	β	α	β	α	β	α	β
1	0	115	0	116	0	115	−4	115	30	124	0	130
2	119	115	118	116	121	115	124	115	115	124	121	130
3	241	115	242	116	239	115	236	115	245	124	239	130
4	0	245	0	244	0	245	4	245	30	236	0	230
5	119	245	118	244	121	245	124	245	115	236	121	230
6	241	245	242	244	239	245	236	245	245	236	239	230

Note: The Eulerian angles α and β are listed for each of the six magnetically nonequivalent centers and are expressed in the degrees of arc; the angles γ are equal to zero.

qualitative level, all these centers have a common origin. The γ1 centers have a symmetry close to axial with respect to the local *z*-axis oriented approximately along one of the directions of the Si–C bond, which does not coincide with the *c*-axis. The γ2 and γ3 centers have a lower symmetry; nevertheless, the preferential direction along the above bonds is quite pronounced. The value of the largest *g*-factor (g_z) decreases in the sequence from γ1 to γ3.

An additional structure was observed for some of the orientations in the ESR spectra for the γ1 signal in the 4*H*-SiC crystal (in which the signals are most intense). This structure can be seen in Fig. 2 for the line at 327.5 mT at θ = 70° and is shown on the expanded scale in Fig. 5. A well resolved outer pair of components with splitting of ~ 1.2 mT and a more intense poorly resolved pair of satellites with a smaller splitting of ~ 0.3 mT are observed. It is most likely that the additional structure is brought about by hyperfine interaction with the ^{29}Si nuclei (in natural silicon, there is 4.7% of the ^{29}Si isotope with a nuclear spin of $I = 1/2$; at the same time, the content of the ^{13}C isotope with the same nuclear spin of $I = 1/2$ in natural carbon is much lower and amounts to a mere 1.1%). The ratio between the intensities of the center line and the additional components can be used to obtain the data on the origin of the HFS. Apparently, the outer pair of the hyperfine components with larger splitting emerges owing to interaction with one or two equivalent silicon atoms. We may assume that satellites with smaller splitting originate due to the interaction of an unpaired electron in the defect with a large number of equivalent silicon atoms residing in a more remote coordination shell. We simulated the ESR spectrum assuming that the HFS with larger splitting is caused by interaction with one or two equivalent silicon atoms, whereas the HFS with smaller splitting is due to successive interaction with 6–12 equivalent silicon atoms. In Fig. 5, the dotted line represents the result of simulating the ESR signal for interaction with two equivalent silicon atoms with the HFS constant equal to 1.23 mT and with nine equivalent silicon atoms with the hyperfine splitting amounting to 0.32 mT. It can be seen that the result of simulation adequately describes the observed ESR signal; however, it should be noted that the agreement between the simulation and experiment could be improved if we consider interactions with several remote nonequivalent coordination shells of silicon and carbon. We do not present here the results of corresponding calculations because there is evidently no sufficient body of experimental data for choosing the correct combination of silicon and carbon atoms. In our opinion, the comparatively effective interaction with two equivalent silicon atoms (1.23 mT) supports the assumption that the defect resides in the carbon sublattice. These two silicon atoms can reside at the C–Si bonds lying outside the $\{11\bar{2}0\}$ plane, in which the magnetic field is rotated and the local *z*-axis of the center is located. Thus, interaction

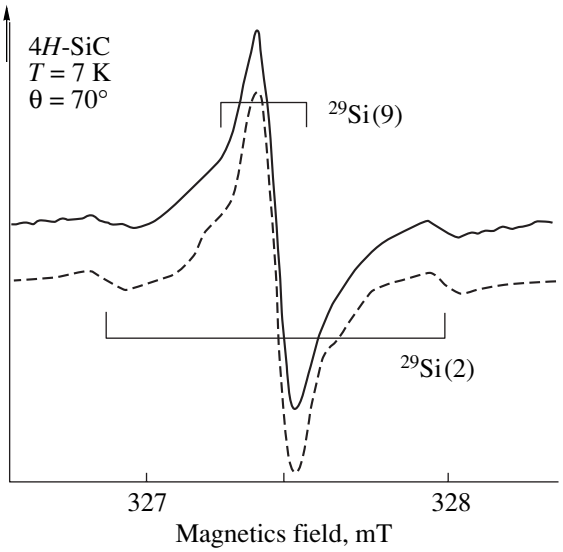

Fig. 5. The ESR line at 327.5 mT (see Fig. 2) recorded for a gamma-irradiated 4*H*-SiC crystal at a temperature of 7 K for θ = 70° and represented on an enlarged scale. The dashed line represents the simulated ESR spectrum calculated in the cases of hyperfine interaction of unpaired electron with two equivalent Si atoms (the magnitude of the hyperfine interaction is 1.23 mT) and with nine equivalent Si atoms (0.32 mT).

with a silicon atom located at the local *z*-axis can be much larger; however, we failed to detect the corresponding structure due to the low intensity of the ESR signal in the $B \parallel z$ orientation.

We studied the effect of isochronous heat treatment on the γ1, γ2, and γ3 centers in the 4*H*- and 6*H*-SiC crystals. The crystal was rapidly heated to a specified temperature above 300 K, kept for 10 min at that temperature, then rapidly cooled to a low temperature at which the highest intensity of the ESR signal corresponding to the γ1, γ2, or γ3 centers was observed, and the ESR spectrum was measured. The process was then repeated at a higher heat-treatment temperature. It was found that the γ1, γ2, and γ3 centers respond similarly to the heat treatment: the intensity of the ESR signal decreases rapidly as the annealing increases, and the signal ceases irreversibly to be detectable after heat treatment at a temperature of ~ 160°C. This temperature corresponds to the annealing off of radiation defects in SiC, which are formed in the carbon sublattice and are typically represented by isolated carbon vacancies.

4. DISCUSSION

The 4*H*- and 6*H*-SiC polytypes have common hexagonal symmetry with the *c* symmetry axis. Each Si atom is surrounded by four C atoms and vice versa. When considering the second coordination shells for the lattice sites in 4*H*-SiC, we can recognize two nonequivalent sites in the lattice, one of which is quasi-cubic (*q*) and the second is hexagonal (*h*). For a *q* site, 12 atoms

in the second coordination shell are arranged in the same way as in the zinc blende cubic structure. For the *h* sites, these atoms are arranged as in the hexagonal wurtzite structure. These sites are distributed uniformly between the carbon and silicon sublattices. There are three such nonequivalent sites in 6*H*-SiC; two of them are quasi-cubic (k_1 and k_2) and the third is hexagonal (*h*). The single type of the γ1-, γ2-, and γ3-center signals was observed in the ESR spectra of both the 4*H*- and 6*H*-SiC crystals irradiated with gamma-ray quanta. As can be seen from the table, the parameters of the ESR spectra for these centers are almost the same in the 4*H*- and 6*H*-SiC crystals. The most important difference between these centers consists in the fact that the low-temperature (γ1) centers have nearly axial symmetry in reference to the local *z*-axis oriented approximately along one of the Si–C-bond directions, which does not coincide with the *c*-axis; in contrast with this, the high-temperature γ2 and γ3 centers have a lower symmetry, although the orientation along the aforementioned bonds is clearly pronounced. Large deviations of g_z from the *g*-factor for a free electron are evident for both centers; the value of the largest *g*-factor (g_z) decreases in the sequence from γ1 to γ3.

Assuming that the ESR signal parameters should differ for the defects formed at dissimilar lattice sites of SiC, we have to choose one of two possible explanations.

The first reasonable explanation is based on the assumption that the γ1, γ2, and γ3 centers correspond to different sites occupied by the defect in the crystal; we refer to the *k* and *h* sites in 4*H*-SiC and the k_1, k_2, and *h* sites in 6*H*-SiC. Since the ESR spectra of the three types are observed for 4*H*-SiC with only two different sites in the crystal lattice, we should rule out the assumption that the γ1, γ2, and γ3 centers occupy different sites in the lattice.

Thus, we may assume that we observe the ESR signals related to the same lattice site and that the γ1, γ2, and γ3 centers correspond to the low- and high-temperature states of the same center (for example, the distortions in the center symmetry caused by the Jahn–Teller effect may differ for these states). An increase in temperature brings about a certain change in the structure of the center; as a result, the orientation of principal axes of the center changes by several degrees and the symmetry is lowered, although the general anisotropy represented by the difference between the largest and the smallest values of the *g*-factor decreases. It is reasonable to assume that the defect formation under the effect of gamma-ray irradiation is equiprobable for different lattice sites in the crystal; therefore, the fact that the ESR spectrum includes the lines that belong to a single center may be caused by the relative position of the level belonging to this defect (for the paramagnetic state) in reference to the Fermi level. It should be emphasized that the gamma-ray irradiation did not result in appreciable changes in the ESR spectra corresponding to the acceptor levels of Al and B, which substantially distinguishes the gamma-ray irradiation from destructive irradiations of other types that, as a rule, result in pinning of the Fermi level at the radiation defects; i.e., it is highly probable that the Fermi level position does not change much after gamma-ray irradiation. Thus, the level of the detected defect is close to the Fermi level in the *p*-4*H*- and *p*-6*H*-SiC crystals doped with aluminum.

At this stage of the investigation, we may advance only tentative suggestions concerning the structure of the γ1, γ2, and γ3 centers. It is well known that gamma-ray irradiation gives rise to fast secondary electrons in the crystal; these electrons produce radiation defects in the crystal lattice of irradiated samples. In accordance with the energy of the gamma-ray quanta used in this study (1.12 MeV), the average energy of the secondary electrons is low and amounts to about 500 keV; i.e., this energy is equal in its order of magnitude to the threshold energy for the production of radiation defects in SiC.

In contrast with Si where the process of the production of radiation defects is well understood [1], this process in SiC is much more complicated due to the presence of two sublattices (those of Si and C). Correspondingly, we have a much larger number of possible native defects in SiC. Primary defects formed under the effect of irradiation are the Frenkel pairs in the Si and C sublattices; i.e., these defects can be combinations of a silicon vacancy (V_{Si}) and an interstitial Si atom (Si_i) or the combinations of a carbon vacancy (V_C) and an interstitial carbon atom (C_i). It is reasonable to assume that the threshold for the formation of the Frenkel pairs in the Si sublattice is higher than that in the C sublattice because of the difference in masses of the corresponding atoms. The irradiation energy for the formation of closely spaced vacancies and interstitials (Frenkel pairs) in the C sublattice is in the range of 100–150 keV, and that in the Si sublattice ranges from 220 to 300 keV [10]. For higher irradiation energies, spatially separated vacancies and interstitials are mainly produced. In Si, the primary defects are unstable at room temperature [1], and only the complexes formed as a result of capturing the primary defects by impurities or other defects are stable; in contrast with this, the Si and C vacancies in SiC are apparently stable at room temperature and the formation of vacancy complexes occurs at higher temperatures. Nevertheless, as far as we know, there are no indications that the Si and C interstitial atoms cannot be mobile during gamma-ray irradiation at room temperature.

To the best of our knowledge, there have been only a few studies which have been concerned with irradiation of SiC with fast electrons that have energies close to the displacement threshold for the atoms in the main lattice. Two new zero-phonon lines G_1 and G_2, peaked at 2.547 and 2.528 eV, were observed in the luminescence spectra of 6*H*-SiC crystals irradiated

with 400-keV electrons [19]. Zeeman splitting was detected for one of these lines (G_1) in a magnetic field.

In very elegant studies [10], the lines of several types of defects, including the Frenkel pairs in the Si sublattice, were detected in the ESR spectra of 6*H*-SiC crystals irradiated with 300–350-keV electrons.

We failed to detect any known ESR signals related to radiation defects in the gamma-irradiated crystals. However, this cannot serve as conclusive evidence that these defects are not formed under gamma-ray irradiation because either the intensity of the corresponding spectra may be too low or the paramagnetic states of the known defects cannot be detected owing to a specific position of the Fermi level.

Destruction of the γ1, γ2, and γ3 centers at a temperature of ~ 160°C indicates that these defects are most likely formed in the carbon sublattice, which is consistent with low irradiation energies; in this case, the formation of widely separated pairs consisting of the carbon vacancies V_C and interstitial carbon atoms C_i is more probable. Since the C_i atoms are presumably mobile at room temperature, they can be captured by impurities. As a result, the V_C vacancies in some charged state and impurity-containing complexes may be formed. The majority impurity in the crystals is Al. The formation of complexes with Al in Si subjected to ionizing radiation has been studied thoroughly [20]; it has been shown that an interstitial Si atom pushes the Al atom out of a lattice site, which gives rise to a paramagnetic center in the form of an interstitial Al atom (similar atoms have also been observed for other impurity elements of Group III). It is also conceivable that, under certain conditions, a paramagnetic complex consisting of a vacancy and an element of Group III can be formed in Si [21]. Since an Al atom in the aforementioned process occupies the Si site, a composite complex, involving a carbon atom at the Si site C_{Si} (an antisite defect) and an interstitial Al atom, may be formed.

We discuss first the possible relation of the ESR spectra reported in this study to the carbon vacancies. It is pertinent to compare the V_{Si} vacancy in silicon with the carbon vacancy V_C in SiC because, in both cases, electrons reside at the silicon orbitals. Two paramagnetic states of the vacancy, V_{Si}^+ and V_{Si}^-, have been observed. In both cases, $S = 1/2$; the *g*-factors are highly anisotropic and are equal to $g_z = 2.0151$, $g_x = 2.0028$, and $g_y = 2.0038$ for V_{Si}^+, and $g_z = 2.0087$ and $g_x = g_y = 1.9989$ for V_{Si}^- [1]. As for SiC, only a single charge state of the carbon vacancy (V_C^+) has been reported [2, 6]; in this case, the anisotropy of the *g*-factors has been also observed, with the largest *g*-factor value being along the ⟨111⟩ axis. Theoretical calculations predict that a pronounced Jahn–Teller effect should be observed for carbon vacancies, with this effect being enhanced as the negative charge of the vacancy increases [22]. Such an effect also exists for vacancies in silicon, and this results in an appreciable enhancement of the *g*-factor anisotropy. According to calculations, the magnitude of the Jahn–Teller effect in SiC is much larger than that in Si [22]. We may assume that an increase in the magnitude of the Jahn–Teller effect results in an enhancement of the *g*-factor anisotropy for the negatively charged state of the divacancy (V_C^-); consequently, the ESR signals observed in this study may be related to V_C^-. Important information can be derived from studies of the hyperfine interaction. However, due to the comparatively low intensity of ESR signals, we managed only to observe the hyperfine structure in a narrow range of orientations; the values of these orientations support, to an extent, the assumption that the ESR spectra of new centers are related to the carbon vacancy. Nevertheless, on the basis of obtained data, it is difficult to explain such a large excess of g_z over the pure spin-related *g*-factor ($\Delta g \sim 0.04$, see table) without considering the involvement of an impurity.

Thus, it is also quite reasonable to assume that the γ1, γ2, and γ3 centers are formed as a result of the capture of mobile primary defects (C_i) by the impurity Al atoms, the concentration of which is very high in the crystals studied. The involvement of Al in the complex may account for a large shift of the *g*-factor in reference to the *g*-factor of the free electron. However, the ESR spectrum does not feature an HFS related to Al, which has a single stable isotope with the nuclear spin $I = 5/2$ (if a hyperfine interaction occurs, it contributes only to the linewidth; i.e., its magnitude amounts to less than 0.05 mT); this makes the involvement of Al in the complex very problematic. There are data on the ESR signals of Al- and B-related centers with deep levels in the band gap; according to the suggested model, these centers are neutral complexes consisting of the impurity at the silicon lattice site and the carbon vacancy located at the neighboring lattice site lying along the *c*-axis [14]. In these centers, the hyperfine interaction with Al (B) is weak because there is no direct spin density at impurities; however, this interaction is much stronger (on the order of 1 mT for Al) than the upper limit for the impurity–vacancy interaction derived from the linewidths of ESR lines related to the γ1, γ2, and γ3 centers. Thus, an impurity can be involved only indirectly in these centers, similarly to the role of boron in the boron–vacancy complex in Si [21], in which case a hyperfine interaction has not been observed. The obtained data on the ESR spectra do not rule out the possibility that interstitial carbon or the antisite defect are involved in the complex; the reason for this is that the hyperfine interaction with an individual C atom cannot be detected for the EPR signal intensities observed owing to a low concentration of ^{13}C atoms.

5. CONCLUSION

For the first time, we observed the paramagnetic defects formed under the effect of gamma-ray irradiation in SiC crystals. Three types of signals related to defects, denoted in this study as γ1, γ2, and γ3, were detected in the ESR spectra of gamma-irradiated Al-doped *p*-4*H*- and *p*-6*H*-SiC crystals. These centers have almost the same parameters of the spin-related Hamiltonian with the electron spin $S = 1/2$ and feature a pronounced anisotropy of *g*-factors; the deviation of these *g*-factors from the free-electron *g*-factors is as large as ~ 0.04. The γ1 centers have nearly axial symmetry relative to the local *z*-axis oriented approximately along one of the directions of the Si–C bond that does not coincide with the *c*-axis. The γ2 and γ3 centers have a lower symmetry, although orientation along the aforementioned bonds is clearly pronounced; the value of the largest *g*-factor (g_z) decreases in the sequence from γ1 to γ3. The ESR signal intensities for the γ1, γ2, and γ3 centers are temperature-dependent; the γ1 signal was distinguishable at low temperatures (3.5–15 K), whereas the γ2 and γ3 signals were observed at higher temperatures of 10–35 and 18–50 K, respectively. Thus, there are comparatively narrow temperature ranges in which two specific ESR signals can be observed simultaneously; in addition, the ESR signals of these centers broaden significantly before their disappearance with increasing temperature. A hyperfine interaction of an unpaired electron in the γ1 center with the ^{29}Si isotope nuclei was detected for some crystal orientations. The γ1, γ2, and γ3 centers cease to exist at 160°C; it was concluded that the ESR signals of these centers are related to the defects produced in the C sublattice under the effect of gamma-ray irradiation. It is assumed that the γ1, γ2, and γ3 centers have a common origin and are related to the low- (γ1) and high-temperature (γ2 and γ3) modifications of the same center. We discussed the models of the defect in the form of a negatively charged carbon vacancy or of a complex consisting of an Al impurity atom and a C atom that resides either at the Si lattice site or at the interstice.

ACKNOWLEDGMENTS

We thank V.V. Emtsev and D.V. Poloskin for letting us use the facility for gamma-ray irradiation of SiC crystals and for their helpful participation in discussions, and we also thank I.O. Chernoglazova, who performed a number of measurements and calculations.

This study was supported in part by the Russian Foundation for Basic Research, project no. 00-02-16950.

REFERENCES

1. G. D. Watkins, in *Deep Centers in Semiconductors*, Ed. by S. T. Pantelides (Gordon and Breach, New York, 1986), p. 147 and references therein.
2. H. Itoh, A. Kawasuso, T. Ohshima, *et al.*, Phys. Status Solidi A **162**, 173 (1997).
3. L. A. de S. Balona and J. H. Loubser, J. Phys. C **3**, 2344 (1970).
4. V. S. Vaĭner and V. A. Il'in, Fiz. Tverd. Tela (Leningrad) **23**, 3482 (1981) [Sov. Phys. Solid State **23**, 2025 (1981)].
5. N. M. Pavlov, M. I. Iglitsin, M. G. Kosaganova, and V. N. Solomatin, Fiz. Tekh. Poluprovodn. (Leningrad) **9**, 1279 (1975) [Sov. Phys. Semicond. **9**, 845 (1975)].
6. N. T. Son, W. M. Chen, J. L. Lindstrom, *et al.*, Mater. Sci. Forum **264–268**, 599 (1998); N. T. Son, P. N. Hai, and E. Janzen, Mater. Sci. Forum **353–356**, 499 (2001).
7. A. Zywietz, J. Furthmueller, and F. Bechsted, Phys. Rev. B **59**, 15166 (1999).
8. T. Wimbauer, B. K. Meyer, A. Hofstaetter, *et al.*, Phys. Rev. B **56**, 7384 (1997).
9. H. J. von Bardeleben, J. L. Cantin, I. Vickridge, and G. Battistig, Phys. Rev. B **62**, 10126 (2000).
10. H. J. von Bardeleben, J. L. Cantin, L. Henry, and M. F. Barthe, Phys. Rev. B **62**, 10841 (2000).
11. E. Sorman, N. T. Son, W. M. Chen, *et al.*, Phys. Rev. B **61**, 2613 (2000).
12. E. N. Mokhov and Yu. A. Vodakov, Inst. Phys. Conf. Ser. **155** (3), 177 (1997) and references therein.
13. L. S. Dang, K. M. Lee, and G. D. Watkins, Phys. Rev. Lett. **45** (5), 390 (1980).
14. P. G. Baranov, I. V. Ilyin, and E. N. Mokhov, Solid State Commun. **100**, 371 (1996).
15. A. V. Duijn-Arnold, J. Mol, R. Verberk, *et al.*, Phys. Rev. B **60**, 15829 (1999) and references therein.
16. I. V. Ilyin, E. N. Mokhov, and P. G. Baranov, Mater. Sci. Forum **353–356**, 521 (2001).
17. B. K. Meyer, A. Hofstaetter, and P. G. Baranov, Mater. Sci. Forum **264–268**, 591 (1998).
18. V. G. Grachev, Zh. Éksp. Teor. Fiz. **92**, 1834 (1987) [Sov. Phys. JETP **65**, 1029 (1987)].
19. D. Volm, B. K. Meyer, E. N. Mokhov, and P. G. Baranov, Mater. Res. Soc. Symp. Proc. **339**, 705 (1994).
20. G. D. Watkins, Phys. Rev. B **1**, 1908 (1970).
21. G. D. Watkins, Phys. Rev. B **13**, 2511 (1976).

Translated by A. Spitsyn

Semiconductors, Vol. 35, No. 12, 2001, pp. 1355–1360. Translated from Fizika i Tekhnika Poluprovodnikov, Vol. 35, No. 12, 2001, pp. 1417–1422.

ELECTRONIC AND OPTICAL PROPERTIES OF SEMICONDUCTORS

Interaction of Hydrogen with Radiation Defects in *p*-Si Crystals

O. V. Feklisova*, N. A. Yarykin*, E. B. Yakimov*, and J. Weber**

** Institute of Problems in Microelectronics Technology and Ultrahigh-Purity Materials, Russian Academy of Sciences, Chernogolovka, Moscow oblast, 142432 Russia*

e-mail: feklisov@ipmt-hpm.ac.ru

*** Institut für Tieftemperaturphysik, Technische Universität Dresden, D-01062 Dresden, Germany*

Submitted March 12, 2001; accepted for publication April 3, 2001

Abstract—Interaction of hydrogen with radiation defects in *p*-Si crystals was studied by deep-level transient spectroscopy. Hydrogen was introduced into the electron-irradiated crystals using wet chemical etching in a solution of nitric and hydrofluoric acids at room temperature with subsequent annealing at 380 K under reverse bias applied to the formed Schottky diodes. It is found that the passivation of radiation defects is accompanied with the formation of new electrically active centers with the concentration profile dependent on the hydrogen concentration. It is shown for the first time that hydrogen passivates the electrical activity of the C_sC_i centers. Based on the data about the spatial distribution of defects and the kinetics of passivation, the plausible origin of the newly formed centers is analyzed. The radii of hydrogen capture by divacancies, the *K* centers, the C_sC_i complexes, and new centers were determined. © *2001 MAIK "Nauka/Interperiodica".*

INTRODUCTION

Hydrogen from the majority of commonly used reagents and even water vapor can easily penetrate during various stages of technological treatments into silicon crystal owing to its high hydrogen diffusivity even at room temperature [1]. Due to the high chemical activity of hydrogen, it can readily react with impurities and crystal-lattice defects and passivate the electrical activity of a number of defects with shallow and deep levels [2]. The mechanism of interaction of shallow-level acceptors with hydrogen is well understood [2]; the mechanism of such interaction is less clear in the case of other defects. It has been found recently [3–6] that, in addition to passivation of electrical activity, interaction of hydrogen with defects and impurities may result in the formation of new electrically active centers; the latter represent intermediate products of a sequence of transformations that result in the complete passivation of the electrical activity of these defects and impurities.

Intrinsic point defects and their complexes with impurity atoms are formed in silicon crystals at various stages of technological treatments; therefore, a study of the interaction of these defects with hydrogen is not only of pure scientific interest but also of practical importance. In the case of hydrogen introduced in silicon crystals with existing radiation defects or introduced by implanting silicon samples with protons, a number of new types of defects that were not observed in the hydrogen-free samples were detected [7–10]. Thus, for example, the majority defect arising in *n*-Si and having the level *E*(0.32) in most of the publications is related to hydrogenation of the vacancy–oxygen complexes (the *A* centers) [9–11].[1] In *p*-Si, the situation is more complex, and the origin and structure of either of the observed defects arising as a result of the interaction of hydrogen with radiation defects has not been identified [7, 12].

In this paper, we report the results of studying the interaction of hydrogen with radiation defects in *p*-Si using deep-level transient spectroscopy (DLTS). It is shown that the concentrations of all radiation defects decrease as a result of hydrogenation; in addition, this process is accompanied with the formation of new electrically active defects. Based on data on the spatial distribution of new defects and on the kinetics of radiation-defect passivation, we analyzed the plausible origin and structure of the formed defects. We estimated the radii of the hydrogen entrapment for various radiation defects.

EXPERIMENTAL

We used a set of *p*-Si crystals that were grown by the Czochralski (Cz) and crucibleless floating-zone (FZ) methods and which had various concentrations of boron (from 6×10^{14} to 3×10^{15} cm^{-3}), oxygen, and carbon. The samples were irradiated at room temperature with 2–6-MeV electrons; the dose range was 10^{14}–10^{16} cm^{-2}. Hydrogen was introduced into the crystals in the course

[1] Henceforth, designations like *E*(0.32) or *H*(0.30) indicate the positions of the energy levels. The letter *E* signifies that the energy is measured from the conduction-band bottom, whereas the letter *H* indicates that the energy is measured from the valence-band top. The numerical energy values in brackets are given in electronvolts.

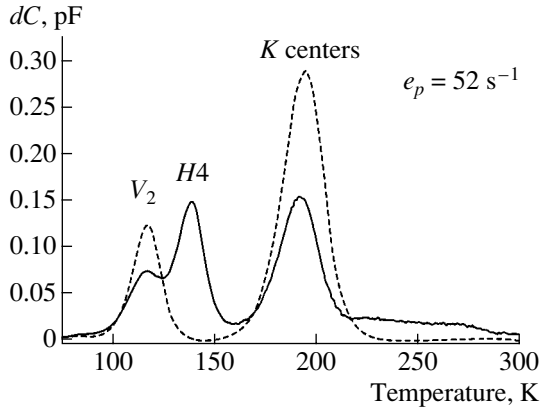

Fig. 1. The DLTS spectra of irradiated *p*-Si crystal grown by the Czochralski method and subjected to wet chemical etching (dashed line) with subsequent annealing with a reverse bias applied at T = 380 K (the solid line).

of wet chemical etching in a solution of hydrofluoric and nitric acids (HF : HNO_3 = 1 : 7) at room temperature; the etching rate was 2–4 μm/min.

Schottky barriers were formed by the thermal deposition of Al in vacuum. Ohmic contacts were deposited on the back side of the samples using an Al + Ga paste. The concentration profiles of charge carriers were determined from capacitance–voltage (*C–V*) characteristics. The deep-level spectra were measured using the DLTS in the temperature range of 40–300 K; a conventional setup with a phase-sensitive amplifier as a correlator was used. The filling 1-ms pulses were applied to the diodes during the measurements of the deep-level spectra. The spatial distribution of the deep-level centers was measured under a constant reverse bias and under varying amplitude of the filling pulse in the computerized DLTS setup; nonuniform distribution of doping impurity was taken into account when calculating the concentration profile.

RESULTS

It is known that intrinsic point defects [vacancies (*V*) and interstitial atoms (*I*)] are generated in silicon irradiated with high-energy electrons. Interstitial atoms can be involved in the substitution reactions with some impurities [13] by pushing the latter to the interstices (C_i and B_i). These secondary defects that migrate in silicon can, in turn, be involved in various chemical reactions and form defects that are stable at room temperature [14]; these defects include C_iO_i carbon–oxygen centers (*K* centers) with *H*(0.36), B_iO_i boron–oxygen pairs with *E*(0.25), B_iB_s boron–boron centers with *H*(0.30), and metastable C_sC_i carbon–carbon complexes with *E*(0.1/0.17) and *H*(0.05/0.09). Vacancies are transformed into vacancy–oxygen *V–O* complexes (*A* centers) with *E*(0.17) and divacancies V_2 with *E*(0.23), *E*(0.4), and *H*(0.21). The ratio between concentrations of stable radiation defects in silicon depends heavily on the type and concentration of impurity in the as-grown crystal.

The DLTS makes it possible to observe only the centers capturing the majority charge carriers; i.e., only the centers with levels in the lower half of the band gap can be tested in the *p*-Si crystals. The conventional DLTS spectrum of irradiated *p*-Si crystals includes the peaks related to the donor level of divacancy V_2 with *H*(0.21), the carbon–oxygen complexes C_iO_i (the *K* centers), and the metastable carbon–carbon complexes C_sC_i in the FZ-Si samples.

The effect of hydrogenation on the energy spectrum of deep levels in silicon grown by the Czochralski method and irradiated with high-energy electrons is illustrated in Fig. 1. Immediately after wet chemical etching, no changes are observed in the DLTS spectra of these samples; only the levels corresponding to conventional radiation defects (divacancies and the *K* centers) (Fig. 1, the dashed line) are detected. This is explained by the fact that the hydrogen penetrating into the surface layers is captured quite effectively by boron in the *p*-Si crystals. Simultaneously, electrically inactive B–H pairs are formed [15]. The B–H bond becomes unstable at temperatures of 340–380 K. Therefore, annealing at such temperatures under the conditions of applied reverse bias [reverse-bias annealing (RBA)] stimulates the penetration of released hydrogen to a greater depth where it can react both with boron and with other defects. The extent of hydrogen penetration can be determined from a characteristic dip formed in the concentration profile of electrically active boron obtained by *C–V* measurements in the course of isothermal RBA [15].

The RBA induced the following changes in the DLTS spectra of irradiated Cz-Si samples: the amplitudes of the peaks related to radiation defects decreased and a new peak *H*4 with *H*(0.28) emerged (Fig. 1, the solid curve). *H*4 centers were formed in all Cz- and FZ-Si crystals as a result of RBA at T = 340–380 K. It is noteworthy that any new centers with deep levels were not formed in unirradiated crystals subjected to hydrogenation. In Fig. 2, we show the concentration profiles of electrically active boron, radiation defects, and the *H*4 centers after wet chemical etching with subsequent annealing at T = 380 K under the conditions of applied reverse bias. It can be seen that, as the RBA duration increases, the concentrations of *K* centers and divacancies decrease in the hydrogenated region. The concentration of new *H*4 centers first increases, then passes through a maximum, and finally decreases. All changes in the concentration profile of *H*4 centers occur in the region saturated with hydrogen. In addition, it was found that the total concentration of *K* and *H*4 centers features a flat distribution profile (Fig. 2b); i.e., a decrease in the *K*-center concentration is approximately equal to the increase in the *H*4-center concentration.

Carbon–carbon complexes C_sC_i are formed (along with *K* centers and divacancies) as a result of irradiation in silicon grown by the crucibleless floating-zone

method; the C_sC_i complexes can be reliably identified on the basis of their metastable behavior [16]. Figure 3 illustrates the DLTS spectra measured for irradiated FZ-Si, in which case only the peaks related to radiation defects are detected after wet chemical etching (dashed curve). Using the same annealing procedure with the application of reverse bias, we found that the signal related to all radiation defects diminishes and the signals related to the *H*4 and *H*3 centers become distinguishable (Fig. 3, the solid curve). The special features of the formation of *H*4 centers in the course of RBA in these samples are similar to those observed in the Cz-Si crystals; i.e., as the duration of RBA increases, the *H*4-center concentration increases with the subsequent formation of a minimum in the region with high hydrogen concentration, whereas the *H*4-center concentration profile correlated closely with hydrogen concentration. However, a balance between the decrease in the *K*-center concentration and the formation of *H*4 centers was not observed in the FZ-Si crystals; in some cases, the concentration of the formed *H*4 centers exceeded twofold the initial concentration of the *K* centers. The *H*3-center concentration increased with increasing RBA duration and, in some cases, exceeded appreciably the initial concentrations of the K centers and divacancies. It can be seen from Fig. 3 (the solid line) that the concentration of the C_sC_i complexes also decreases. As far as we know, this is the first experimental observation of the effect of hydrogen on the electrical activity of these complexes. At present, we cannot relate the disappearance of the C_sC_i complexes to the emergence of any other level. Therefore, it remains unclear whether a C_sC_i–H complex is formed in this situation or whether hydrogen stimulates the decomposition of the C_sC_i pair. However, we note that theoretical calculations [17] are indicative of the possible formation of a hydrogen-containing complex based on the C_sC_i center.

We emphasize once again that all observed variations in the spectrum of radiation defects and new *H*3 and *H*4 centers are restricted to the hydrogenated zone of the crystal.

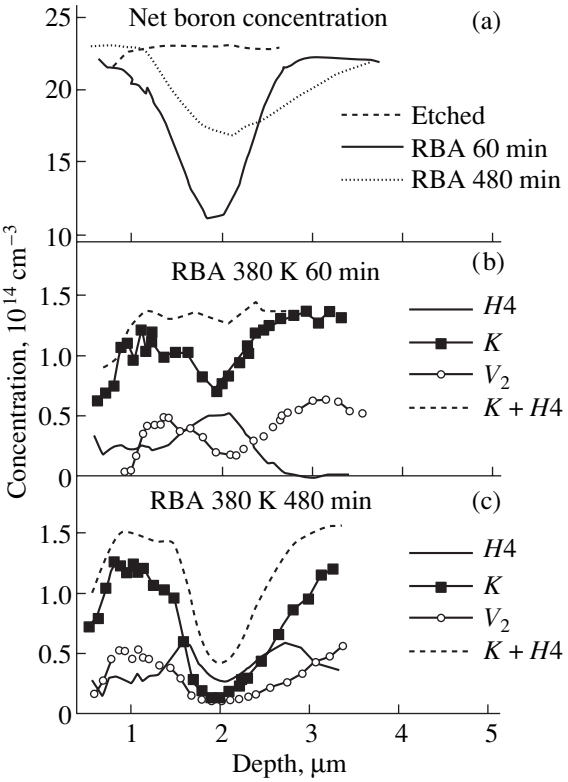

Fig. 2. The concentration profiles of (a) electrically active boron and [(b), (c)] the centers with deep levels in an irradiated Cz-Si crystal subjected to wet chemical etching with subsequent reverse-bias (4 V) annealing (RBA) for 60 and 480 min.

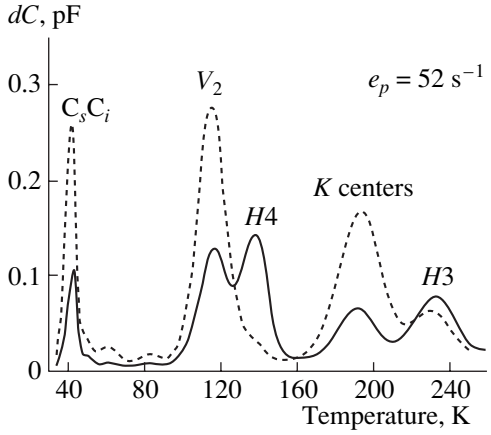

Fig. 3. The DLTS spectra of irradiated *p*-Si crystal grown by the crucibleless floating-zone method and subjected to wet chemical etching (dashed line) with subsequent reverse-bias annealing at T = 380 K (the solid line).

DISCUSSION

We now analyze the reactions of the successive attachment of hydrogen to a defect with concentration N_0. Assuming that the products of this interaction are stable at the temperatures used in the experiments, we can mathematically represent the interaction of the defect with hydrogen and the formation of new complexes at an arbitrary point in the crystal as [18]

$$\frac{\partial N_0}{\partial t} = -4\pi D r_0 N_0 [\mathrm{H}], \quad (1.1)$$

$$\frac{\partial N_i}{\partial t} = 4\pi D (r_{i-1} N_{i-1} - r_i N_i)[\mathrm{H}], \quad (1.2)$$

where N_i is the concentration of complexes containing i hydrogen atoms; r_0 and r_i are the radii of capture of a hydrogen atom by the complexes containing no hydrogen atoms and i hydrogen atoms (i = 1, 2, 3, …), respectively; and [H] and D are the concentration and

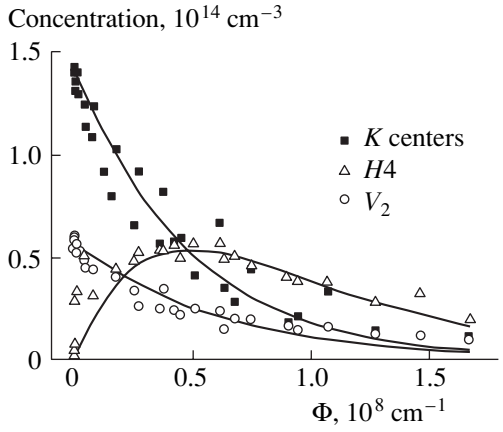

Fig. 4. The kinetics of the defect transformation in an irradiated Cz-Si crystal in the course of annealing with a reverse bias applied at $T = 380$ K. The values of Φ were calculated using both formula (3) and the concentration profiles for electrically active boron.

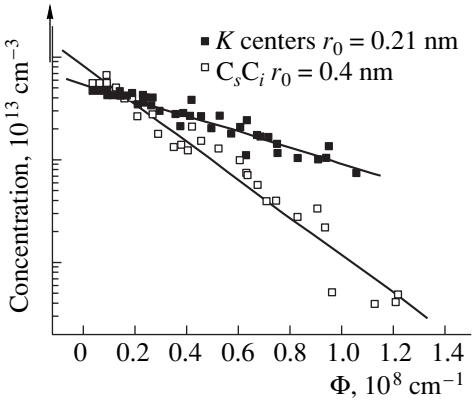

Fig. 5. The transformation kinetics for the K centers and the C_sC_i complexes in an FZ-Si crystal in the course of annealing with reverse bias applied at $T = 380$ K.

diffusion coefficients of hydrogen. In order to solve Eqs. (1.1) and (1.2), we need to know the values of D, r, and [H]. However, this problem can be obviated if we transform the system of Eqs. (1.1) and (1.2) into the form

$$\frac{\partial N_0}{\partial \Phi} = -r_0 N_0, \tag{2.1}$$

$$\frac{\partial N_i}{\partial \Phi} = r_{i-1} N_{i-1} - r_i N_i, \tag{2.2}$$

where

$$\Phi = \int_0^{t_0} 4\pi D[\mathrm{H}]\,dt. \tag{3}$$

Under the conditions of dynamic equilibrium between [H] and [B–H], the concentration of mobile (not bound by boron) hydrogen can be defined as

$$[\mathrm{H}] = \frac{\nu_{\mathrm{BH}}}{4\pi D r_{\mathrm{BH}}} \frac{[\mathrm{B}]_0 - [\mathrm{B}]}{[\mathrm{B}]}, \tag{4}$$

where ν_{BH} is the dissociation rate for the B–H pairs at a specified temperature, $[\mathrm{B}]_0$ is the total boron concentration, and [B] is the concentration of electrically active boron (not passivated by hydrogen). The values of r_{BH} and ν_{BH} were experimentally determined previously [15] and were found to be equal to $r_{\mathrm{BH}} = 4$ nm and $\nu_{\mathrm{BH}} = 3 \times 10^{-3}$ s^{-1} at 380 K. By substituting (4) into (3), we can determine the values of Φ from experimental data at specific points in relation to the RBA duration t_0. Profiling by the DLTS method allows us to determine the concentrations of radiation defects and new centers after each RBA stage. We can reconstruct the distribution of electrically active boron from the C–V measurements, and we can calculate the values of Φ using (3) and (4) after each RBA stage. We can then put into correspondence the values of the defect concentration measured experimentally at an arbitrary point of the crystal and the value of Φ at the same point and obtain the dependence of $N_{0,i}$ on Φ: $N^{\mathrm{exp}}(\Phi)$. By comparing the obtained dependences $N^{\mathrm{exp}}(\Phi)$ with theoretical dependences $N^{\mathrm{theor}}(\Phi)$ that are solutions to Eq. (2.1) for N_0 and Eq. (2.2) for N_i and by varying the values of $r_{0,i}$ as free parameters, we can estimate the radius of capture of a hydrogen atom by a defect. In Fig. 4, we show the dependences of the K-center, divacancy, and $H4$-center concentrations on the value of Φ; the concentrations were measured at several depths in the vicinity of the dip in the concentration profile for electrically active boron in the Cz-Si crystals. For the K centers and divacancies, the solid lines in Fig. 4 were calculated in accordance with Eq. (2.1) using r_0 as an adjustable parameter for attaining the best fit to the experimental data.

The use of the above scheme for determining the radii of capture of hydrogen by the defects makes it possible to compare the parameters of reactions for various defects. According to our estimations, the radii of capture of hydrogen by divacancies in both the Cz- and FZ-Si crystals were in the range of 0.14–0.17 nm. For the K centers, these radii ranged from 0.14 to 0.21 nm. Possibly, the larger spread of radii is caused by the fact that another defect with almost the same activation energy can contribute to the peak corresponding to the K centers in the DLTS spectrum [19]; in this case, the hydrogenation kinetics is more complex. Nevertheless, it should be noted that the values of the radii of the hydrogen capture by the K centers and divacancies are almost the same. The passivation kinetics for the C_sC_i complexes in FZ-Si is illustrated in Fig. 5, where the kinetics of passivation of the K centers is also shown for the sake of comparison. The best fit of the curve calculated in accordance with Eq. (2.1) to the experimental

data was attained for the radius of hydrogen capture by the C_sC_i complexes equal to $r_0 \approx 0.4$ nm, which exceeds the corresponding radii for the *K* centers and divacancies by a factor of about 2–3.

We now analyze the processes of the formation of the new hydrogen-containing complexes *H*3 and *H*4. The concentration of the *H*3 centers was found to be comparable to that of the main radiation defects in all studied FZ-Si crystals; however, these centers were practically absent in many Cz-Si samples (cf. Figs. 1, 3). The centers *H*(0.51) resembling the *H*3 centers were observed after the implantation of either boron or hydrogen ions [12]; it was inferred that these centers are complexes of interstitial boron and hydrogen [12]. In our experiments, the formation of *H*3 centers was observed in the boron-doped irradiated samples in the zone with a high hydrogen concentration after annealing at 380 K. This is consistent with the previous inferences [12]; however, the issue of the source of interstitial boron remains unresolved, especially for the FZ-Si crystals depleted in oxygen.

The *H*4 centers were formed in all studied irradiated samples. The formation of centers similar to *H*4 has been observed previously [7]; it has been established that these centers are related to hydrogen, although their microscopic structure has not yet been identified [7]. Assuming that an *H*4 complex is the product of the interaction of hydrogen with radiation defects, we consider the most probable defects acting as the sources of the *H*4 centers. The concentration of the *H*4 centers at its peak exceeded that of the divacancies in the crystal bulk in almost all of the studied crystals; in addition, the *H*4 centers were formed as a result of the hydrogenation of the crystals in which divacancies V_2 were previously annealed out. Therefore, we exclude divacancies from further consideration. On the other hand, a decrease in the concentration of the *K* centers was completely compensated by an increase in the *H*4-center concentration in the Cz-Si crystals at the early stages of RBA (Fig. 2b); therefore, it is reasonable to assume that the *H*4 centers are complexes of the *K* centers and hydrogen atoms [20]. The behavior of the *H*4-center concentration in the course of RBA may be described in the following way: At the first stages of RBA, hydrogen, released as a result of the dissociation of the B–H pairs, is captured by the *K* centers and forms the C_iO_i–H complexes (*H*4); when the concentration of these complexes increases, they react with hydrogen on their own and are transformed into other (probably, electrically inactive) defects by attaching another hydrogen atom. Since this process has a higher rate in the zone with the highest hydrogen concentration, a dip in the *H*4-center distribution becomes distinguishable (Fig. 2c).

The dependence of the *H*4-center concentration in the Cz-Si crystals on the quantity Φ is well described using Eq. (2.2), under the assumption that these centers originate from the *K* centers if the values of $r_0 = 0.21$ nm and $r_1 = 0.2$ nm are used for the radii of capture of the first and second hydrogen atoms, respectively, by the *K* centers (Fig. 4). This can also serve as an additional argument in favor of the above assumption concerning the relation between the *H*4 and *K* centers.

As mentioned above, there is no balance between the increase in *K*-center concentration and the *H*4-center formation, so that the concentration of the forming *H*4 centers exceeds even the initial *K*-center concentration. It is difficult to account for this result in the context of the suggested structure of the *H*4 center as a complex of a *K* center and a hydrogen atom. In order to explain this fact, we provide several suggestions.

First, another level close in energy to *H*4 can contribute to the peak denoted as *H*4 in the DLTS spectrum. However, formation of this level should also be controlled by the presence of hydrogen. It is known [21] that hydrogen can stimulate the modification of defects in silicon. We may assume, for example, that the B_iC_s or B_iB_s complexes can play the role of the products of such a modification in the irradiated *p*-Si samples; these complexes have an activation energy close to that of *H*4: *H*(0.29) for B_iC_s and *H*(0.30) for B_iB_s [22]. The formation of B_iC_s complexes, distributed uniformly over the crystal bulk with a concentration exceeding that of the *K* centers, was observed after annealing at ~200°C. The temperature position of the peak corresponding to B_iC_s differs by several degrees from that of the peak related to the *H*4 centers. However, the resolution of the conventional DLTS setups gives no way of separating these two peaks reliably if both types of centers are present in the sample. The peak of the B_iC_s complexes is even closer to the DLTS signal related to the *H*4 centers.

Second, additional *K* centers or directly the hydrogenated *K* centers (i.e., the *H*4 centers) can be formed as a result of hydrogen-stimulated modification of some defects in the FZ-Si crystals. In this situation, we should assume that the mobile isolated atoms of interstitial carbon C_i or the C_i–H complexes (these are also mobile according to [17]) are formed under the effect of hydrogen; these atoms and complexes can be entrapped by oxygen. As shown above, the C_iC_s complexes that cease to exist as a result of RBA can serve as the sources of C_i or C_i–H. However, certain contradictions remain in this scheme as well; for example, it is unclear how the *H*4 centers can be formed with a concentration that exceeds even the total concentration of the *K* centers and the C_sC_i complexes.

Third, we may assume that the *K* centers are not the sources of *H*4 centers at all; rather, the latter are formed from other defects; e.g., the *A* centers that are produced with fairly high concentration during irradiation. However, in this case, the distinct correlation between the *K*- and *H*4-centers in the Cz-Si crystals remains unexplained. In addition, *E*4 centers with *E*(0.32) emerge in the irradiated *n*-Si crystals as a result of wet chemical etching; according to [9, 11], it is these centers that are the complexes of the *A* centers and hydrogen atoms.

The transformation of *A* centers into *E*4 centers in proton-implanted *n*-Si crystals exposed to light has also been observed [10]. Further studies are required to confidently resolve the issue concerning the origin and structure of the *H*4 centers.

CONCLUSION

We used the DLTS to study the effect of hydrogenation on the energy spectrum of defects in *p*-Si crystals subjected to wet chemical etching with subsequent reverse-bias annealing (RBA). We found that the hydrogenation of radiation defects is accompanied with the formation of new electrically active centers (*H*4 and *H*3). Based on the analysis of concentration profiles for the defects after wet chemical etching and RBA, we assume that the *H*4 centers are complexes of *K* centers and hydrogen atoms; however, the formation of the *H*4 centers in the Cz-Si crystals differs from that in the FZ-Si crystals. This study of the hydrogenation kinetics of radiation and newly formed defects makes it possible to estimate the radii of entrapment of hydrogen by the defects; this was done for divacancies, *K* centers, C_sC_i complexes, and *H*4 centers.

ACKNOWLEDGMENTS

This study was supported in part by the Russian Foundation for Basic Research (project no. 00-02-04002) and the Deutsche Forschungsgemeinschaft (grant no. 436 RUS 113/166/0).

REFERENCES

1. C. H. Seager, R. A. Anderson, and J. K. G. Panitz, J. Mater. Res. **2** (1), 96 (1987).
2. S. J. Pearton, J. W. Corbett, and M. Stavola, *Hydrogen in Crystalline Semiconductors* (Springer-Verlag, Berlin, 1992).
3. J.-U. Sachse, E. Ö. Sveinbjörnsson, W. Jost, *et al.*, Phys. Rev. B **55**, 16176 (1997).
4. J.-U. Sachse, J. Weber, and H. Lemke, Mater. Sci. Forum **258–263**, 307 (1997).
5. E. Ö. Sveinbjörnsson and Ö. Engström, Phys. Rev. B **52**, 4884 (1995).
6. N. Yarykin, J.-U. Sachse, J. Weber, and H. Lemke, Mater. Sci. Forum **258–263**, 301 (1997).
7. K. Irmscher, H. Klose, and K. Maas, J. Phys. C **17**, 6317 (1984).
8. A. Hallen, B. U. R. Sundquist, Z. Paska, *et al.*, J. Appl. Phys. **67**, 1266 (1990).
9. O. Feklisova and N. Yarykin, Semicond. Sci. Technol. **12**, 742 (1997).
10. Y. Tokuda, Jpn. J. Appl. Phys. **37**, 1815 (1998).
11. A. R. Peaker, J. H. Evans-Freeman, P. Y. Y. Kan, *et al.*, Physica B (Amsterdam) **273–274**, 243 (1999).
12. S. Fatima, C. Jagadich, J. Lalita, *et al.*, J. Appl. Phys. **85** (5), 2562 (1999).
13. G. D. Watkins, *Radiation Damage in Semiconductors* (Dunod, Paris, 1965).
14. G. D. Watkins, Mater. Res. Soc. Symp. Proc. **469**, 139 (1997).
15. T. Zundel and J. Weber, Phys. Rev. B **39**, 13549 (1989).
16. W. Song, X. D. Zhan, B. W. Benson, and G. D. Watkins, Phys. Rev. B **42**, 5765 (1990).
17. P. Leary, R. Jones, and S. Öberg, Phys. Rev. B **57** (7), 3887 (1998).
18. N. Yarykin, J.-U. Sachse, H. Lemke, and J. Weber, Phys. Rev. B **59** (8), 5551 (1999).
19. P. M. Mooney, L. J. Cheng, M. Süli, *et al.*, Phys. Rev. B **15** (8), 3836 (1977).
20. O. Feklisova, N. Yarykin, Eu. Yakimov, and J. Weber, Physica B (Amsterdam) **273–274**, 235 (1999).
21. S. V. Koveshnikov, S. V. Nosenko, and E. B. Yakimov, Fiz. Tekh. Poluprovodn. (Leningrad) **22** (5), 922 (1988) [Sov. Phys. Semicond. **22**, 581 (1988)].
22. P. J. Drevinsky, C. E. Caefer, S. P. Tobin, *et al.*, Mater. Res. Soc. Symp. Proc. **104**, 167 (1988).

Translated by A. Spitsyn

Semiconductors, Vol. 35, No. 12, 2001, pp. 1361–1365. Translated from Fizika i Tekhnika Poluprovodnikov, Vol. 35, No. 12, 2001, pp. 1423–1427.

ELECTRONIC AND OPTICAL PROPERTIES OF SEMICONDUCTORS

Electrical Properties of the Proton-Irradiated Semi-Insulating GaAs:Cr

V. N. Brudnyi* and A. I. Potapov

Kuznetsov Physicotechnical Institute, pl. Revolyutsii 1, Tomsk, 634050 Russia

** e-mail: brudnyi@ic.tsu.ru*

Submitted December 13, 2000; accepted for publication April 26, 2001

Abstract—The *n–p* conversion of the conduction type and a decrease in resistivity to 10^2 Ω cm at 300 K were revealed upon proton irradiation (5 MeV, 300 K, $D \approx 2 \times 10^{17}$ cm^{-2}) of semi-insulating GaAs:Cr ($\rho \approx (3–4) \times 10^8$ Ω cm). Temperature dependences of ρ for heavily irradiated samples indicate a hopping conduction in the temperature range of 400–120 K, with the transition to the conduction with variable-range hopping at $T \leq 120$ K. The effects of electronic switching were found in low-resistivity proton-irradiated GaAs:Cr at about 20 K. The isochronous annealing of radiation defects in the temperature range of 20–750°C was investigated. © *2001 MAIK "Nauka/Interperiodica".*

INTRODUCTION

Starting from the first study, in which an increase in the electrical resistivity of GaAs upon bombardment with H^+ ions (3 MeV) was demonstrated [1], proton irradiation has found a wide application in the formation of high-resistance interelement insulation regions in GaAs-based electron schemes and the fabrication of integrated optics elements, among others. It was demonstrated later that variations in the electrical, recombination, and optical properties of GaAs as a result of high-energy irradiation are conditioned by the trapping of free carriers by deep levels of radiation defects. These are so-called electron (*E*) and hole (*H*) traps, which are radiation defects with the largest concentration in GaAs irradiated at ~300 K [2]. It was demonstrated that, depending on the initial doping level of the material, proton bombardment leads to an increase in the resistivity of GaAs to maximum values $\rho_{max}(D) \approx (10^5–10^9)$ Ω cm at 300 K [3, 4]. For all types of high-energy irradiation, the Fermi level for GaAs attains the limiting (steady-state) position near $F_{lim} \approx E_V + 0.6$ eV, which is identical to the local electroneutrality level position for this material [5]. Subsequent proton irradiation (overirradiation) of such material leads to a decrease in the resistivity of the irradiated samples (compared to maximum resistivity values $\rho_{max}(D)$, which are achieved on the first irradiation) and, finally, to the formation of low-resistivity GaAs layers [4, 6]. This study is devoted mainly to the investigation of the properties of such overirradiated GaAs.

EXPERIMENTAL

The special feature of this study is the investigation of the influence of proton beams on the electrical properties of the Czochralski-grown semi-insulating *n*-GaAs:Cr ($\rho \approx (3–4) \times 10^8$ Ω cm and $\mu_H \approx 1500$ cm^2 V^{-1} s^{-1} at 300 K). The choice of GaAs:Cr was governed by several reasons.

(1) This material is used as the substrate for integrated circuits.

(2) This material is used in high-energy physics for the production of nuclear radiation detectors, specifically, for measuring high-intensity proton beams.

(3) The starting Fermi level in GaAs:Cr is located deep in the band gap and nearby F_{lim} for the material irradiated, which makes it possible to minimize the influence of trapping the free carriers by radiation defects on the electrical properties of the samples irradiated. This offers possibilities for the investigation of the electrical properties of the nearly intrinsic material with a high density of deep local states of radiation defects in the band gap of the crystal. In this case, the position of the Fermi level in the band gap varies only slightly due to irradiation. It should be noted that low-resistivity layers in the semi-insulating GaAs were obtained through bombardment by inert gas ions [7].

Bombardment with hydrogen ions ($E = 5$ MeV) was carried out in a cyclotron at $T \approx 320$ K and at current density $j \approx (1–5) \times 10^{-8}$ A/cm^2. In terms of the mean projected range of H^+ ions (5 MeV) in GaAs, which is about 125–130 μm, the samples with a thickness of $d \approx 90$ μm were chosen for investigations. The ion range was determined from measurements of intensity distribution of the edge cathodoluminescence over the cleavage of the layer irradiated using an electron microprobe with a diameter less than 5 μm. In order to obtain a more uniform distribution of radiation defects along the damaged layer depth, irradiation was carried out from both sides. In this case, integrated fluxes are combined. This offered the possibility of using bulk samples and thereby excluding the influence of the substrate on

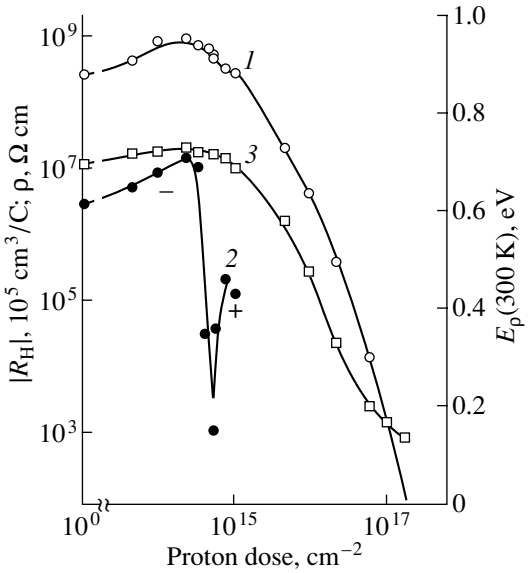

Fig. 1. Variation in (*1*) resistivity ρ, (*2*) Hall constant R_H, and (*3*) activation energy of resistivity $E_ρ$ in the expression $ρ(T) \propto \exp[E_ρ(D)/kT]$ for the proton-irradiated (5 MeV) semi-insulating GaAs. Measurement temperature was $T \approx$ 300 K.

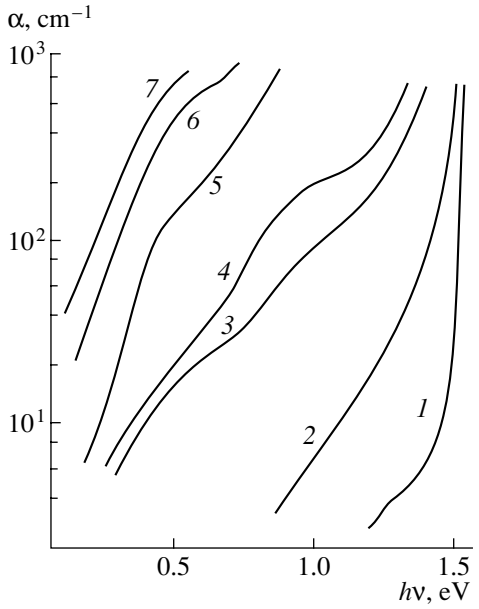

Fig. 2. Optical absorption spectra for the proton-irradiated GaAs:Cr. Measurement temperature $T \approx$ 80 K. Integrated fluxes $D =$ (*1*) 0, (*2*) 10^{14}, (*3*) 10^{15}, (*4*) 3×10^{15}, (*5*) 3×10^{16}, (*6*) 1×10^{17}, and (*7*) 2×10^{17} cm^{-2}.

measured characteristics, which is important for the investigation of a high-resistivity material. In this case, the high efficiency of defect formation due to proton irradiation allows for the obtaining of material with a high density of radiation defects.

EXPERIMENT AND DISCUSSION

The dependences of the resistivity $ρ(D)$, the Hall constant R_H, and the activation energy $E_ρ$ in the expression $ρ(T) \propto \exp[E_ρ(D)/kT]$ on doses D at about 300 K for the material investigated are shown in Fig. 1. Two regions of the variation of electrical resistance and activation energy can be seen in curves $ρ(D)$ and $E_ρ(D)$.

(1) An initial increase in ρ from $(3–4) \times 10^8$ Ω cm to

$$ρ(D)_{max} \approx 1/2en_i(μ_nμ_p)^{1/2} \approx (10^9–2 \times 10^9)\ \Omega\ \text{cm}$$

and the corresponding increase in $E_ρ(D)$ from ≈0.67 eV to $E_ρ(D) \approx E_g/2$ for low H^+ ion doses ($D \lesssim 2 \times 10^{14}$ cm^{-2}).

(2) A decrease in ρ to 10^2 Ω cm and, correspondingly, a decrease in $E_ρ$ to 0.1 eV with the subsequent irradiation of the material with proton doses as high as $D = 2 \times 10^{17}$ cm^{-2}.

Measurements of the Hall effect and thermoelectric power at about 300 K indicate the *n–p* conversion of the conduction type for GaAs:Cr for $D \approx 8 \times 10^{14}$ cm^{-2} due to a Fermi level shift to the limiting (steady-state) position. For GaAs, this value is close to $E_V + 0.6$ eV [5]. In this case, the irradiated material remains of the *p*-type conduction upon further proton bombardment, in accordance with thermoelectric-power measurements at about 300 K.

It is obvious that the variations in the shape of the $ρ(D)$ curves for $D \gtrsim 10^{15}$ cm^{-2} (at about 300 K) correspond to the change in the mechanism of electron transport. Instead of free-carrier transport, the charge is transported according to the hopping mechanism over deep states of radiation defects due to their high density in the overirradiated samples. Deep-level transient spectroscopy (DLTS) measurements for *n*-GaAs demonstrate that the total rate of introducing the *E* and *H* traps into GaAs by protons with energy $E = 5$ MeV is about 10^3 cm^{-1} [8]. For $D \approx 10^{15}$ cm^{-2}, this allows for the estimating of the total concentration of radiation defects as approximately 10^{18} cm^{-3} and, correspondingly, for $D \approx 2 \times 10^{17}$ cm^{-2}, as approximately 10^{20} cm^{-3}. This implies a constant rate of introducing the radiation defects for large H^+ ion doses. In this case, the rate of introducing the *E*5 deep traps (E_C – 0.90 eV), close to which the Fermi level for the irradiated GaAs is pinned, is about 50 cm^{-1}. This corresponds to the trap concentration of about 10^{19} cm^{-3} for $D = 2 \times 10^{17}$ cm^{-2}.

In general, these estimates are confirmed by the data of optical investigations, which demonstrate a high density of states (DoS) in the band gap of proton-irradiated samples (Fig. 2). Optical absorption curves $α(hν)$ take an exponential-like shape, except for specific features close to 0.5 and 0.1 eV. In this case, the contribution of band bending to the $α(hν)$ quantity for the material under investigation should be significant for the edge absorption region only, since the Fermi level shift

for the irradiated regions compared to the Fermi level position for starting GaAs:Cr is less than 0.2 eV. One would expect that the dependence $\alpha(h\nu)$, as a whole, reproduces the DoS distribution in the band gap of the proton-irradiated GaAs:Cr. Assuming that the cross-section of absorption by deep levels is about 5×10^{-17} cm^2 [9], we can use the value of $\alpha(h\nu)$ close to 0.6 eV to estimate the band-gap DoS as approximately 1.6×10^{19} cm^{-3} for $D \approx 2 \times 10^{17}$ cm^{-2}. By the order of magnitude, this value is close to the extrapolated values of the density of $E5$ traps ($E_C - 0.90$ eV) obtained from DLTS measurements.

A high density of deep local centers, whose energy is close to the energy corresponding to $F_{\lim}$ for the proton-irradiated GaAs:Cr, gives rise to hopping conduction (Fig. 3). Thus, for starting crystals, the activation portion of the type $\rho(T) \approx \rho_1 \exp(E_1/kT)$ at $T > 200$ K, where $E_1 \approx 0.67$ eV, is pronounced in temperature dependences of ρ. For low irradiation doses, E_1 increases to the value close to $E_g/2$ (Fig. 3, curve *2*), which corresponds to a certain deepening of the Fermi level due to introducing the radiation defects. In this case, the $1/\rho_1 \approx 10^3$ Ω^{-1} cm^{-1} is close to the value of the so-called lowest metal conductivity for GaAs $\sigma_m \approx$ 550 Ω^{-1} cm^{-1} [9, 10]. This portion of $\rho(T)$ is conditioned by the thermal excitation of charge carriers from deep levels (Cr, radiation defects), which are positioned close to the Fermi level, to the conduction band of the crystal. For lower temperatures, the second activation portion $\rho(T)$ is found. This portion is characteristic of hopping conduction over deep-level centers. The contribution of hopping conduction to the total charge transport increases with increasing the proton dose. In this case, the parallel shift of low-temperature curves $\rho(T)$ to the region of smaller ρ values is observed (Fig. 3, curves *3*–*6*). For these samples, the Fermi level is already pinned close to its limiting value $F_{\lim} \approx E_V +$ 0.6 eV, whereas the material itself is almost completely compensated.

For $D \approx 2 \times 10^{17}$ cm^{-2}, the hopping conduction is dominant in the temperature range from ≈400 to 20 K (Fig. 4). At least two regions of the variation in $\rho(T)$ can be distinguished in curves $\rho(T)$ for these samples at $T <$ 400 K. In the temperature range of 400–150 K, the dependence of the form $\rho(T) \approx \rho_3 \exp(E_3/kT)$ is observed, where $\rho_3 \approx$ (1–2) Ω cm and the E_3 value is about 0.1 eV. This region corresponds to the hopping conduction of carriers over the defect band with the width of about E_3. On decreasing the temperature below 120 K, the local activation energy of electrical conductivity $E_l = \partial \ln\rho/\partial(kT)^{-1}$ decreases, which is indicative of the transition to conduction with variable-range hopping.

In order to investigate the mechanism of hopping conduction in the region of the variable activation energy E_l, the dependences $\rho(T) \propto \exp[(T_0/T)^p]$ were constructed. It was already noted in previous investigations that the choice of the p exponent is a complex

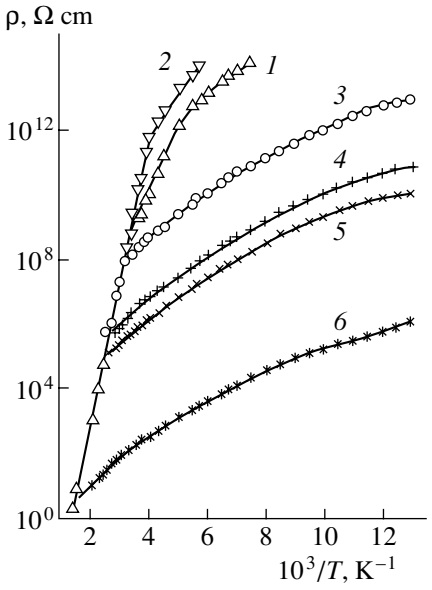

Fig. 3. Temperature dependences of resistivity ρ for the proton-irradiated GaAs:Cr. Integrated fluxes D = (*1*) 0, (*2*) 5×10^{12}, (*3*) 4×10^{15}, (*4*) 1×10^{16}, (*5*) 1.7×10^{16}, and (*6*) 1.5×10^{17} cm^{-2}.

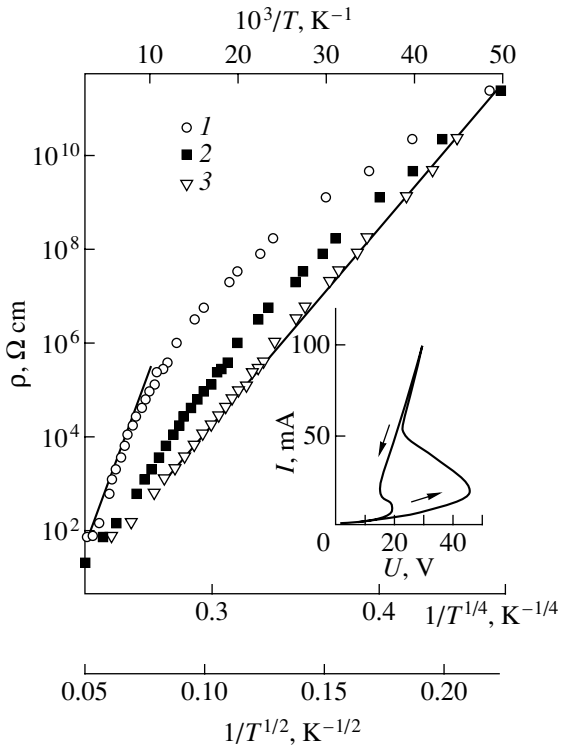

Fig. 4. Temperature dependences of ρ [(*1*) $\rho(T) \propto T^1$, (*2*) $\rho(T) \propto T^{1/2}$, and (*3*) $\rho(T) \propto T^{1/4}$] for the proton-irradiated GaAs:Cr at $D \approx 2 \times 10^{17}$ cm^{-2}. Solid lines denote the portions corresponding to $\rho(T) \propto \exp(0.1/kT)$ for curve *1* and $\rho(T) \propto \exp[(7 \times 10^7/T)^{1/4}]$ for curve *3*. The current–voltage characteristic for the sample irradiated ($T \approx 20$ K) at a load resistance of 350 Ω is shown in the inset.

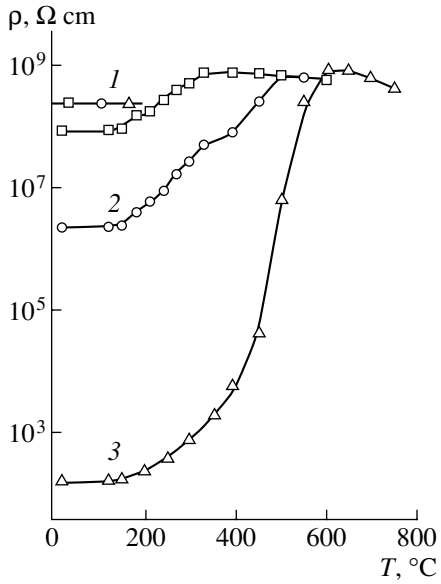

Fig. 5. Isochronous 10-min annealing of proton-irradiated GaAs:Cr. Measurement temperature is 300 K. Integrated fluxes $D = (1)\ 4\times10^{15}$, $(2)\ 1\times10^{16}$, and $(3)\ 1.5\times10^{17}$ cm^{-2}.

problem [11]. Figure 4 demonstrates curves $\rho(T)$ with the p value equal to 1/4 (Mott's law for randomly distributed deep states) and 1/2 (presence of the Coulomb gap in the DoS close to the Fermi level due to the correlation effect). The dependence $\rho(T)$ with the exponent $p = 1/4$ is observed in the range of eight orders of magnitude of varying the ρ value in the temperature range 120–20 K. However, the law of varying $\rho(T)$ remains unknown. The reason is that the curves $\rho(U)$ for high-resistivity samples deviate from Ohm's law for the electrical field $\mathscr{E} \approx 90$ V/cm at $T \approx 20$ K with increasing external bias voltage (U) (see the inset in Fig. 4). This value corresponds to the transition to the region of high electric fields. It is close to the estimated critical strength of the electric field $\mathscr{E}_c = kT/ea \approx 10^2$ V/cm for $a \approx 1$ nm (here, a is the radius of localized states adjacent to the $F_{\lim}$ level [12]). In the region of low temperatures of about 20 K, the phenomena of electronic switching are observed with increasing external bias ($\mathscr{E} > \mathscr{E}_c$). These phenomena consist in the appearance of negative differential resistance of the S type in the static current–voltage characteristic for the overirradiated samples and in the appearance of hysteresis phenomena on applying and decreasing the external bias. These circumstances did not allow for carrying out the measurements of $\rho(T)$ for the material irradiated at liquid-helium temperature.

One would expect that, similarly to amorphous semiconductors, Mott's law is most probable for the description of the low-temperature portion of $\rho(T)$ for an irradiated semiconductor, in which deep-level radiation defects are distributed randomly. For this reason, we used the dependence $\rho(T) \propto \exp[(T_0/T)^{1/4}]$ shown in Fig. 4 to obtain the following estimate:

$$T_0 = A(R/a)^3(E_2/k) \approx 7\times10^7 \text{ K}.$$

Here, $A \approx 21.2$ is the numerical coefficient of the theory [12], and $a \approx 1$ nm was determined from the expression

$$a \approx h/2\pi(2m^*E_i)^{1/2},$$

where $m^* = m_{lh} = 0.08m_0$, and the energy level of the $E5$ trap ($E_C - 0.90$ eV) is taken as the energy of the E_i center. Taking into account that the density of $E5$ levels can be estimated from the relationship $N(E5) \approx 50\ D$ cm^{-3}, this yields $a \approx 1.5$ nm according to the expression

$$\rho_3 = \rho_{03}\exp(1.73/N_{E5}^{1/3}a).$$

Thus, the radius of localization for the $E5$ trap, over which the hopping conduction in the proton-irradiated GaAs:Cr proceeds, is estimated as twofold or threefold for the GaAs lattice constant equal to 0.565 nm. In this case, the average hopping range in the high-temperature limit is approximately 6.5 nm and about 12 nm for low temperatures (at about $T \approx 20$ K). These investigations demonstrate that the electrical properties in a wide temperature range, including 300 K for the proton-overirradiated GaAs:Cr samples, are controlled by carrier hopping conduction over deep states of radiation defects.

The specific features of recovery of electrical properties for the proton-irradiated GaAs:Cr at isochronous annealing in the temperature range of 20–750°C are investigated (Fig. 5). For lightly irradiated samples, the first stage of recovery of ρ in the range of 150–300°C coincides with the anneal of E- and H-traps (supposedly point radiation defects) and corresponds to the return of the Fermi level to the initial preannealing position. For the heavily irradiated samples, due to a high density of radiation defects, the Fermi level, apparently, remains pinned nearby $F_{\lim}$ when the E and H traps are completely annealed off below 300°C. The recovery of ρ, which is observed in the temperature range from ≈200°C to ≈600°C, corresponds to a decrease in the contribution of hopping conduction to the total charge transport due to a decrease in the radiation defect density. In this case, the return of the Fermi level to the position, which is close to its initial position for this material before irradiation, and the reverse n–p conversion of the conduction type occur at annealing temperatures above 600°C. This is attributed to a decrease in the concentration of more complex radiation defects in GaAs, so-called P-traps [$P1$ ($E_C - 0.35$ eV), $P2$ ($E_C - 0.5$ eV), and $P3$ ($E_C - 0.72$ eV)] [13]. These defects keep the Fermi level close to the limiting position $F_{\lim} \approx E_V + 0.6$ eV in the overirradiated material up to the annealing temperatures of 500–600°C. The complete recovery of the electrical properties of such material is not observed even at an annealing temperature as

high as 750°C. This fact is apparently associated with the presence of complex, thermally stable defects of an unknown nature in such material.

CONCLUSION

It is demonstrated that the *p–n* conversion of the conduction type (which follows from the thermoelectric-power measurements) and the further transformation of the semi-insulating GaAs:Cr into low-resistivity *p*-type material are observed upon proton irradiation. In this case, the main variations in ρ (about seven orders of magnitude at about 300 K) are attributed to the appearance of hopping conduction of charge carriers over deep levels of radiation defects. In such low-resistivity layers, the hopping conductivity with the variable activation energy is observed below 120 K, and electronic switching is detected at about 20 K. It is demonstrated that the reverse transformation of the material from a low-resistivity to a high-resistivity (starting) state for the proton-irradiated samples occurs in a wide temperature range. This transformation occurs due to the annealing of the *E* and *H* traps at 200–300°C, and the *P* traps in the temperature range of 400–600°C.

ACKNOWLEDGMENTS

This study was supported in part by the Ministry of Education of the Russian Federation under the Program "Basic Investigations in Nuclear Techniques and the Physics of Ionizing Radiation Beams," grant no. 97-12.9, 2-2.

REFERENCES

1. K. Wohlleben and W. Beck, Z. Naturforsch. A **21** (7), 1057 (1956).
2. D. Pons and J. C. Bourgoin, J. Phys. C **18**, 3839 (1985).
3. J. P. Donnelly and F. L. Leonberger, Solid-State Electron. **20**, 183 (1977).
4. V. N. Brudnyĭ, M. A. Krivov, and A. I. Potapov, Izv. Vyssh. Uchebn. Zaved., Fiz. **25** (1), 9 (1982).
5. V. N. Brudnyi, S. N. Grinyaev, and V. E. Stepanov, Physica B (Amsterdam) **212**, 429 (1995).
6. V. N. Brudnyi, M. A. Krivov, and A. I. Potapov, Solid State Commun. **34**, 117 (1980).
7. V. M. Zelevinskaya, G. A. Kachurin, N. B. Pridachin, and L. S. Smirnov, Fiz. Tekh. Poluprovodn. (Leningrad) **4** (2), 317 (1970) [Sov. Phys. Semicond. **4**, 258 (1970)].
8. V. N. Brudnyĭ, N. G. Kolin, and A. I. Potapov, Izv. Vyssh. Uchebn. Zaved., Fiz. **35** (10), 61 (1992).
9. J. Lucovsky, Solid State Commun. **3**, 299 (1965).
10. T. K. Saxena, S. Bala, S. K. Agarwal, *et al.*, Phys. Rev. B **22**, 2962 (1980).
11. A. G. Zabrodskiĭ, Fiz. Tekh. Poluprovodn. (Leningrad) **11** (3), 595 (1977) [Sov. Phys. Semicond. **11**, 345 (1977)].
12. B. I. Shklovskiĭ and A. L. Efros, *Electronic Properties of Doped Semiconductors* (Nauka, Moscow, 1979; Springer-Verlag, New York, 1984).
13. V. N. Brudnyi, A. V. Gradoboev, and V. V. Peshev, Phys. Status Solidi B **212**, 229 (1999).

Translated by N. Korovin

Semiconductors, Vol. 35, No. 12, 2001, pp. 1366–1368. Translated from Fizika i Tekhnika Poluprovodnikov, Vol. 35, No. 12, 2001, pp. 1428–1430.

ELECTRONIC AND OPTICAL PROPERTIES OF SEMICONDUCTORS

Dynamics of Nonequilibrium Gratings Induced in Silicon Films by Femtosecond Laser Pulses

M. F. Galyautdinov*, V. S. Lobkov, S. A. Moiseev, and I. V. Negrashov

Zavoiskiĭ Physicotechnical Institute, Kazan Scientific Center, Russian Academy of Sciences, Sibirskiĭ trakt 10/7, Kazan 29, 420029 Tatarstan, Russia

**e-mail: Mansur@kfti.knc.ru*

Received March 5, 2001; accepted for publication April 26, 2001

Abstract—Relaxation of the dynamic gratings formed by nonequilibrium charge carriers in thin single-crystal silicon films during femtosecond laser excitation was studied. The case of the ultimate concentration of carriers ($N \approx 10^{21}$ cm^{-3}) is considered. Ambipolar diffusion and Auger recombination contributions to the grating decay are estimated. The observation of a long-lived grating at pump intensity above 5×10^{11} W/cm^2 is reported.

INTRODUCTION

The dynamics of free carriers generated in semiconductors during pico- and femtosecond laser pulse action is attracting considerable interest. This is due to the formation of highly nonequilibrium states of the electron and phonon subsystems. Femtosecond laser pulses with peak intensity $I \approx 10^{11}$ W/cm^2 may generate a highly overheated electron–hole plasma with carrier concentration $N \approx 10^{21}$ cm^{-3} [1–3]. These nonequilibrium states have the lifetime $t_p = 10^{-12}$–10^{-14} s, determined by a number of competing mechanisms [1–7]. Our study of single-crystal Si films is aimed at evaluating the role of the main relaxation mechanisms in the electron–hole plasma decay.

EXPERIMENTAL

We applied the technique based on probe beam diffraction by dynamic grating induced in a sample [4, 5, 8].

A femtosecond, passive mode-locked CPM (colliding-pulse mode-locked), ring dye laser produced by Avesta Ltd. was pumped by all spectral lines of an LGN-512 argon laser. The output pulses propagated through two six-pass FN-70 dye amplifiers pumped by a copper vapor laser. The resulting pulses were bandwidth-limited and had a pulse duration of 80 fs, a repetition rate of 10 kHz, a pulse energy of 2–4 μJ, a peak at 615 nm, and horizontal polarization. The amplified beam was split in a 30/70 ratio. The smaller part was fed to a computer-controlled optical delay line to form a probing beam I_{pr} (Fig. 1). The other part, in turn, was split into two parts of equal intensity to form the pump beams I_1 and I_2. To compensate for the optical path difference produced by splitting, one of the pump beams was delayed in its own optical delay line. Both pump beams were focused by a lens and crossed each other in a sample at an angle θ. As a result, the interference pattern was formed over an area of about 100-μm in size according to the expression

$$I(x, t) = I_0(t)[1 + V\cos(2\pi x/\Lambda)], \quad (1)$$

where $I(x, t)$ is the intensity of light, x is the distance along the direction perpendicular to the bisectrix between I_1 and I_2 directions, V is the modulation depth, λ is the wavelength, and $\Lambda = \lambda/2\sin(\theta/2)$ is the grating period.

The intensity of the probe-beam diffraction by the grating was measured with a photomultiplier (R4220, Hamamatsu) in the photon counting mode and was processed by computer.

Pure silicon (ρ = 10 Ω cm) was used as the sample. Since the absorption of silicon at the laser wavelength is high ($\alpha = 4 \times 10^3$ cm^{-1} at $\lambda = 615$ nm), the thickness of the samples was chosen so that their optical density D was rendered close to unity. In our case, the 10-μm-thick sample has the optical density $D \approx 1.1$.

The diffraction grating is initiated by the light-induced change in the refractive index (Δn) in the interference antinodes. According to the classical Drude model [5], in Si, $\Delta n = 9 \times 10^{-22} N$ for $\lambda = 1.06$ μm, where N is the nonequilibrium free carrier density. In accordance with this, the phase modulation depth in the samples under study should depend on their thickness and their excitation level. For sinusoidal phase grating and in the case of sufficiently thin samples (thickness is less than the skin depth), the first-order diffraction efficiency F_{eff} can be estimated using the well-known formula [4]

$$F_{\text{eff}} \propto J_1(g), \quad (2)$$

where $J_1(g)$ is the Bessel function of the first kind, $g = \pi N \Delta n_{\text{eh}} d/\lambda$ is the Bessel function argument, Δn_{eh} is the change produced in the refractive index by an electron–hole pair, and d is the sample thickness.

The typically attainable density of nonequilibrium carriers in silicon for nano- and picosecond photoexcitation amounts to $N = 10^{18}$–10^{19} cm^{-3} [4–6]. Using these values and formula (2), we estimated F_{eff} at $\approx 5 \times 10^{-3}$–5×10^{-5} for 10-μm-thick Si films. At such F_{eff} values, diffraction is confidently observed in experiments.

The structures under discussion decay via a number of competing mechanisms, the main ones being the ambipolar diffusion and Auger recombination. To investigate the relaxation kinetics, we varied the interference pattern period Λ by changing the angle θ between the beams I_1 and I_2 (Fig. 1). In doing so, we varied the ambipolar diffusion contribution and were thus able to assess its effect on the relaxation process. In the course of the experiment, the sample was kept at room temperature, and the absence of irreversible changes was assured.

RESULTS AND DISCUSSION

Normalized dependences of the diffraction efficiency on the delay time between the pump and probe pulses for three different periods of the interference pattern are plotted in Fig. 2. The angles between the two beams θ, grating periods Λ, and the grating lifetime constants t_p are listed in the table.

At small grating periods Λ, the results obtained are adequately explained in terms of the diffusion model. Under the assumption of electrical neutrality ($N_e \approx N_h \approx N$), we have

$$dN/dt = D_{\text{diff}} d^2N/dx^2, \quad (3)$$

where D_{diff} is the ambipolar diffusion coefficient. According to this model, the grating lifetime is defined by the expression

$$\Lambda = 2\pi\sqrt{D_{\text{diff}} t_p}. \quad (4)$$

Using formula (4), we determined the free-carrier diffusion coefficients for Λ = 0.64 μm. The resulting value $D_{\text{diff}} \approx 14$ cm^2/s is in good agreement with similar data obtained in other studies ($D_{\text{diff}} \approx 10$ cm^2/s [4, 5]).

As the grating period increases, its decay rate decreases, but not as fast as predicted by Eq. (3). Hence, it follows that, in the cases illustrated by curves *2* and *3* in Fig. 2, the grating decay is caused not only by the diffusion but also by the free carrier recombination. Let us evaluate the influence of Auger recombination on the rate of decay for large values of *N*. Taking into account both the diffusion and Auger recombination and assuming that there is electrical neutrality, we describe the relaxation of the electron–hole plasma grating by the following equation [5]:

$$dN/dt = D_{\text{diff}} d^2N/dx^2 - \gamma N^3. \quad (5)$$

Here, γ is the Auger coefficient.

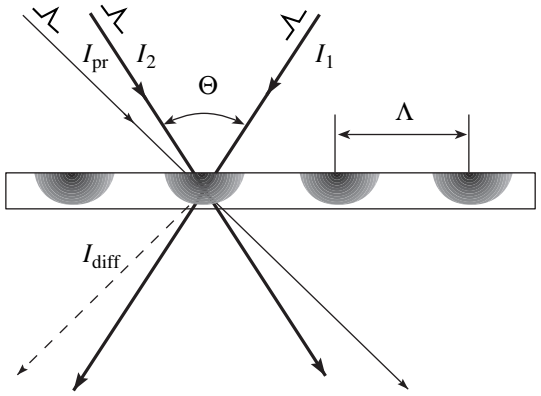

Fig. 1. Schematic representation of the dynamic grating formation.

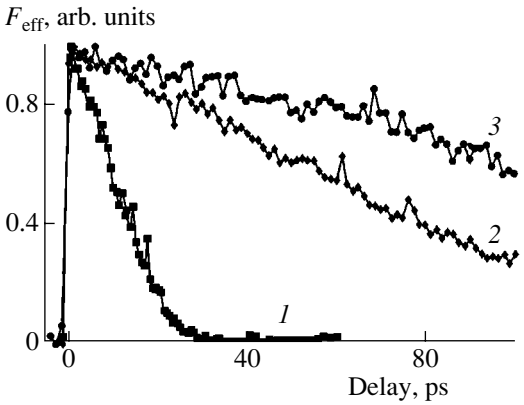

Fig. 2. Diffraction efficiency of the dynamic grating vs. the probe-beam delay for three periods of interference pattern.

For large periods Λ, the dependence *N*(*t*) can be approximated by a simple asymptotic expression

$$N(t) \approx \frac{N(t=0)}{\sqrt{1 + 2t\gamma(N(t=0))^2}}. \quad (6)$$

Using formulas (2) and (6), with only the Auger recombination considered, we can estimate the grating-lifetime constant t_p at large grating periods Λ as

$$t_p = (2\gamma(N(t=0))^2)^{-1}. \quad (7)$$

For $N(t=0) = 10^{20}$ cm^{-3} and $\gamma \approx 4 \times 10^{-31}$ cm^6/s [7], we obtain $t_p \approx 100$ ps, which correlates well with the

Table

Period no.	θ, deg	Λ, μm	t_p, 10^{-12} s
1	57	0.64	14
2	14	2.63	71
3	7	5.26	172

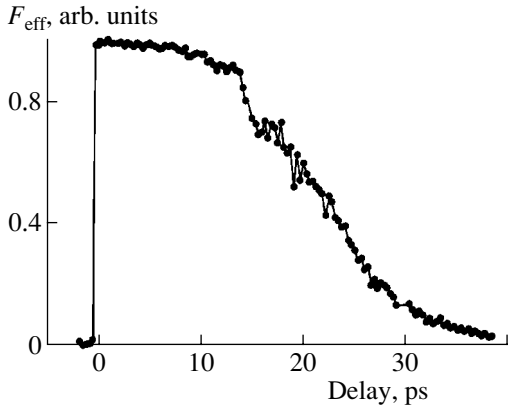

Fig. 3. Diffraction efficiency of the dynamic grating with small period vs. the probe-beam delay at $I \approx 5 \times 10^{11}$ W/cm^2.

diffraction-signal behavior observed in experiment (Fig. 2, curve *3*).

One more special feature of the decay was detected when the pump power exceeded 10^{11} W/cm^2. In this case, we observed an approximately 12 ps delay in the decay of grating with a small period ($\Lambda \approx 0.64$ μm). The corresponding plateau can be seen in Fig. 3. We believe that the delay is caused by the metallization of the semiconductor surface due to the high-density electron–hole plasma ($N > 10^{21}$ cm^{-3}); this case was analyzed in detail by Kopaev [9].

In conclusion, studying diffraction by the dynamic structures induced by light in thin semiconductor films allows for the investigation of highly nonequilibrium electron–hole plasma. We hope that subsequent experiments will clarify the relaxation mechanisms considered above, including the formation and properties of the metallized state of a semiconductor.

ACKNOWLEDGMENTS

This study was supported by the Russian Foundation for Basic Research, project nos. 00-15-96615 and 00-15-97410.

REFERENCES

1. N. I. Koroteev and I. L. Shumaĭ, *Physics of High-Power Laser Radiation* (Nauka, Moscow, 1991).
2. C. V. Sank, R. Yen, and C. Hirlimam, Phys. Rev. Lett. **51**, 900 (1983).
3. A. Tom, G. Aumiller, and C. Brito-Cruz, Phys. Rev. Lett. **60**, 1438 (1988).
4. S. G. Odulov, I. I. Peshko, M. S. Soskin, and A. I. Khizhnyak, Ukr. Fiz. Zh. **21** (11), 1869 (1976).
5. J. P. Woerdman, Opt. Commun. **2** (5), 212 (1970).
6. A. M. Bonch-Bruevich, V. A. Kovalev, G. S. Romanov, *et al.*, Zh. Tekh. Fiz. **38** (4), 677 (1968) [Sov. Phys. Tech. Phys. **13**, 507 (1968)].
7. V. A. Abakumov and I. N. Yassievich, Fiz. Tekh. Poluprovodn. (Leningrad) **11** (7), 1302 (1977) [Sov. Phys. Semicond. **11**, 766 (1977)].
8. V. S. Lobkov, S. A. Moiseev, and E. A. Shtyrkov, Opt. Spektrosk. **64** (1), 79 (1988) [Opt. Spectrosc. **64**, 47 (1988)].
9. Yu. V. Kopaev, V. V. Menyaĭlenko, and S. N. Molotkov, Zh. Éksp. Teor. Fiz. **89** (4), 1404 (1985) [Sov. Phys. JETP **62**, 813 (1985)]; Mikroélektronika **14** (2), 153 (1985).

Translated by A. Sidorova-Biryukova

Semiconductors, Vol. 35, No. 12, 2001, pp. 1369–1371. Translated from Fizika i Tekhnika Poluprovodnikov, Vol. 35, No. 12, 2001, pp. 1431–1433.

ELECTRONIC AND OPTICAL PROPERTIES OF SEMICONDUCTORS

Radiative Recombination via Direct Optical Transitions in $In_{1-x}Ga_xAs$ ($0 \le x \le 0.16$) Solid Solutions

M. Aĭdaraliev, N. V. Zotova, S. A. Karandashev, B. A. Matveev*, M. A. Remennyĭ, N. M. Stus', and G. N. Talalakin

Ioffe Physicotechnical Institute, Russian Academy of Sciences, Politekhnicheskaya ul. 26, St. Petersburg, 194021 Russia

** e-mail: bmat@iropt3.ioffe.rssi.ru*

Submitted April 26, 2001; accepted for publication May 11, 2001

Abstract—Photoluminescence from $In_{1-x}Ga_xAs$ ($0 \le x \le 0.16$) solid solution epilayers LPE-grown on (111)InAs substrates and electroluminescence from *p*–*n* junctions on their bases have been studied in the temperature range 77–450 K. Despite the negative lattice mismatch between epilayer and substrate, radiative recombination in epilayers occurs via direct optical transitions ensuring a high internal quantum efficiency of luminescence (6% at 295 K). © *2001 MAIK "Nauka/Interperiodica".*

1. INTRODUCTION

$In_{1-x}Ga_xAs$ solid solutions of composition $0 \le x \le 0.2$ can be used to fabricate optoelectronic devices emitting in the 2.5–3.8 μm spectral range. The structural and luminescent properties of InGaAs solid solutions, with near-InAs compositions and LPE-grown on InAs substrates, were studied in [1–7]. InGaAs/InAs heterostructures with a negative lattice mismatch between the epitaxial layer and the substrate ($\bar{a}_{sub} > \bar{a}_{epi}$) are characterized by instabilities at the heterointerface, which lead to "island-type" layer growth and cluster formation [8]. This may result in violation of the wave vector conservation law and, correspondingly, in radiative recombination via indirect optical transitions [9]. Since the design of efficient light-emitting diodes (LEDs) and lasers requires semiconductor materials with direct optical transitions that can ensure high quantum efficiency of luminescence, the question as to whether the wave vector is conserved in the InAs/InGaAs system is rather important.

The goal of this study was to reveal the contribution of direct optical transitions to radiative recombination at 77–450 K in epilayers of $In_{1-x}Ga_xAs$ solid solutions ($0 \le x \le 0.16$) and *p*–*n*-structures on their basis, which were LPE-grown on (111)InAs substrates.

2. OBJECTS OF THE STUDY AND EXPERIMENTAL PROCEDURE

InGaAs/InAs heterostructures, LPE-grown on (111)*p*-InAs substrates, were studied. To fabricate *p*–*n* junctions, the melt was doped with Mn in the concentration range 10^{-3}–10^{-4}. Doping with manganese, which has a lower diffusion rate and vapor pressure as compared with conventional acceptors in III–V compounds such as Zn and Cd, allowed fine control over the doping level and the position of the *p*–*n* junction in the structure. The activation energy of the Mn level in $In_{1-x}Ga_xAs$ solid solution ($0 \le x \le 0.2$) is about 20 meV and increases with a further rise in *x* [3]. Epilayers of the *n*-type were nominally undoped and had carrier densities in the range $n \approx 1$–2×10^{17} cm^{-3}; the hole density in *p*-layers was 10^{16}–10^{17} cm^{-3}. The thickness of the InGaAs layer was 5–10 μm. The band gap gradient across the epilayer thickness was negligible [1].

Photoluminescence (PL) spectra were recorded at $T = 77$ K in the reflection configuration (with radiation excited and detected at the surface of a solid solution layer). An LPI-14 semiconductor laser ($\lambda = 0.8$ μm, $P_{pulse} \approx 50$ W) was used for excitation. For electroluminescence (EL) studies, ~100-μm-thick LED chips were mounted, *p*-substrate down, onto TO-18 packages, and voltage was applied to the LEDs through a U-shaped gold contact on the chip surface near the cathode (see Fig. 1 in [4]), which ensured the absence of current lines near the inactive *p*-InAs surface.

3. EXPERIMENTAL RESULTS AND DISCUSSION

Figure 1 presents PL spectra of *n*-type $In_{0.95}Ga_{0.05}As$ and $In_{0.84}Ga_{0.16}As$ epilayers at 77 K. The peak position and the short-wavelength wings of the spectra are well described in terms of the model of direct interband transitions, spherical constant-energy surfaces, and thermalized minority carriers (dashed line) [5]:

$$I(E) \approx \left[E_g + \left(1 + \frac{m_e}{m_h}\right)E\right]^2 \sqrt{E} \exp\left(-\frac{m_e}{m_h}\frac{E}{kT}\right) \times \left(\exp\left(\frac{E-\zeta}{kT}\right) + 1\right)^{-1}, \quad (1)$$

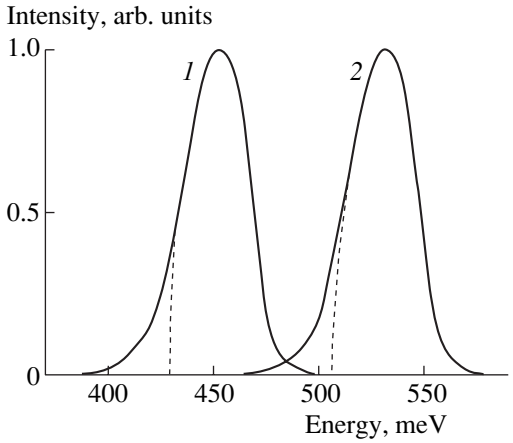

Fig. 1. PL spectra of (*1*) n-$In_{1-0.95}Ga_{0.05}As$ and (*2*) $In_{0.84}Ga_{0.16}As$ epilayers. T = 77 K.

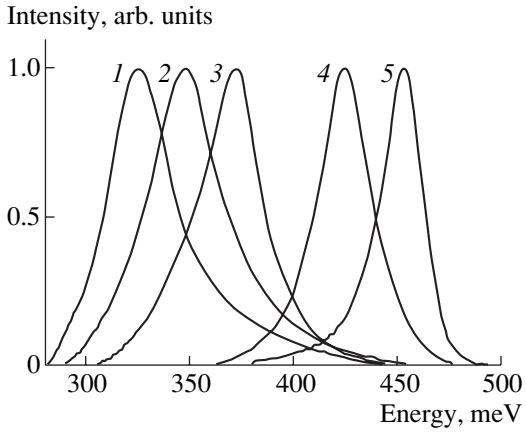

Fig. 2. EL spectra of $InAs/In_{1-0.95}Ga_{0.05}As$ LED. Temperature: (*1*) 450, (*2*) 370, (*3*) 295, (*4*) 160, and (*5*) 77 K.

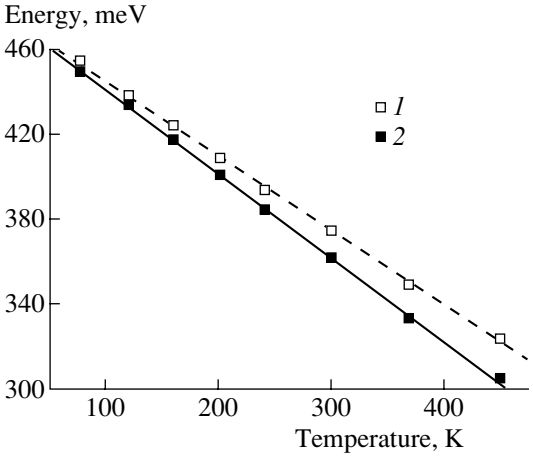

Fig. 3. Temperature dependences of (*1*) EL spectral peak energy $h\nu_{max}$ and (*2*) $h\nu_{max} - kT/2$ for an $InAs/In_{1-0.95}Ga_{0.05}As$ LED.

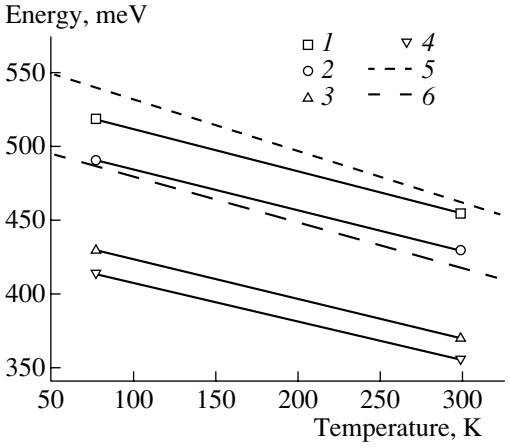

Fig. 4. PL spectral peak energy of n-$In_{1-x}Ga_xAs$ epilayers with x: (*1*) 0.054, (*2*) 0.06, (*3*) 0.12, and (*4*) 0.16, (*5*) E_g, (*6*) $h\nu - kT/2$ (x = 0.12).

where E is the electron energy reckoned from the conduction band bottom, $m_e = 0.03m_0$ and $m_h = 0.4m_0$ are the electron and heavy hole masses, and $\zeta = 30$ meV is the Fermi level for electrons at $n = (1–2) \times 10^{17}$ cm^{-3}. The E_g value obtained from spectrum processing correlates well with the interpolation $E_g(x) = 0.42 + 0.63x + 0.45x^2$ [6].

Figure 2 shows EL spectra of LEDs based on p–n junctions in $In_{1-0.95}Ga_{0.05}As$ in the temperature range 77–450 K. Owing to the high electron mobility, radiative recombination takes place in the p-region of the p–n junction, so the spectra were processed in terms of the model of direct electronic transitions from the conduction band to the manganese acceptor level. The short-wavelength wings of the spectral lines are described by the dependence $I \propto \exp(-h\nu/kT)$, which is typical of direct transitions. The spectral half-width increases with temperature from 20 meV at 77 K to 40 meV at 450 K. For optical transitions with wave vector conservation from the conduction band to an acceptor level, the transition energy must be lower than the EL peak energy ($h\nu_{max}$) by $kT/2$, and its temperature dependence must follow that of the band gap [by virtue of (1)]. Temperature dependences of $h\nu_{max}$ and $h\nu_{max} - kT/2$ are presented in Fig. 3. Indeed, the slope of the dependence, $d(h\nu_{max} - kT/2)/dT = 3.8 \times 10^{-4}$ eV/K, virtually coincides with the temperature variation of the band gap in InAs, the closest analogue of the solid solution: ($dE_g/dT = 3.8 \times 10^{-4}$ eV/K [7]). The EL intensity falls by a factor of 70 with temperature increasing from 77 to 300 K, which is comparable with the decrease in the intensity of luminescence from the binary InAs compound [9].

Figure 4 shows peak energies of the EL spectra of $In_{1-x}Ga_xAs$ layers for the compositions x = 0.054, 0.06, 0.12, and 0.16 (77, 295 K). With temperature increasing

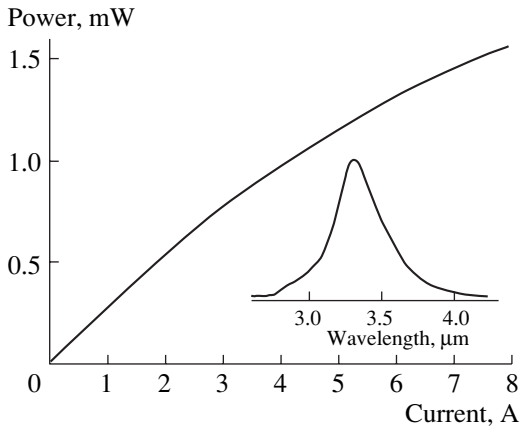

Fig. 5. Light–current characteristic and (insert) emission spectrum of $InAs/In_{0.95}Ga_{0.05}As$ LED. T = 295 K. Pulse width 5 μs, frequency 500 Hz.

from 77 to 295 K, the EL peaks are shifted by the same amount, and the slope of the $h\nu - kT/2$ dependence (Fig. 4, straight line *6*) coincides with that of the temperature dependence of the InAs band gap (Fig. 4, straight line *5*).

Figure 5 shows the emission–current characteristic and the emission spectrum of a *p*-$InAs/In_{0.95}Ga_{0.05}As$ LED (λ_{max} = 3.3 μm) at room temperature. The power obtained in the linear portion of the light–current curve (up to ~1 A) corresponds to external and internal quantum efficiencies of 0.08 and ~6%, respectively.

4. CONCLUSION

The coincidence between the calculated and experimental PL spectra of *n*-type $InGa_{0.05}As$ and $InGa_{0.16}As$ epilayers (77 K), the equal slopes of the temperature dependences of the transition energy and band gap in $In_{0.95}Ga_{0.05}As$ LEDs (77–450 K) and in $In_{1-x}Ga_xAs$ LEDs (x = 0.054, 0.06, 0.12, 0.16) (77, 295 K), and the high internal quantum efficiency of luminescence indicate that the mechanism of radiative transitions in $In_{1-x}Ga_xAs$ solid solutions obeys the wave vector conservation law and remains unchanged in the composition range $0 \le x \le 0.16$ at 77–450 K.

REFERENCES

1. N. V. Zotova, S. A. Karandashev, B. A. Matveev, *et al.*, Fiz. Tekh. Poluprovodn. (Leningrad) **21** (6), 1079 (1987) [Sov. Phys. Semicond. **21**, 658 (1987)].
2. M. Aĭdaraliev, N. V. Zotova, S. A. Karandashev, and N. M. Stus', Fiz. Tekh. Poluprovodn. (Leningrad) **23** (4), 592 (1989) [Sov. Phys. Semicond. **23**, 371 (1989)].
3. N. V. Zotova, S. A. Karandashov, B. A. Matveev, *et al.*, Cryst. Prop. Prep. **12**, 243 (1987).
4. M. Aĭdaraliev, N. V. Zotova, S. A. Karandashev, *et al.*, Fiz. Tekh. Poluprovodn. (St. Petersburg) **34** (1), 102 (2000) [Semiconductors **34**, 104 (2000)].
5. A. Mooradian and H. Y. Fan, Phys. Rev. **148** (2), 875 (1996).
6. G. B. Stringfellow and P. E. Greene, J. Electrochem. Soc. **118** (5), 805 (1971).
7. O. Madelung, *Physics of III–V Compounds* (Wiley, New York, 1964; Mir, Moscow, 1967).
8. M. G. Astles, O. D. Dosse, A. J. Machelan, and P. J. Wright, J. Cryst. Growth **54** (3), 485 (1981).
9. Z. M. Fang, K. J. Ma, D. H. Jaw, *et al.*, J. Appl. Phys. **67** (11), 7034 (1990).

Translated by D. Mashovets

Semiconductors, Vol. 35, No. 12, 2001, pp. 1372–1374. Translated from Fizika i Tekhnika Poluprovodnikov, Vol. 35, No. 12, 2001, pp. 1434–1436.

ELECTRONIC AND OPTICAL PROPERTIES OF SEMICONDUCTORS

Effect of Structural Imperfection on the Spectrum of Deep Levels in 6*H*-SiC

A. A. Lebedev, D. V. Davydov, A. S. Tregubova, E. V. Bogdanova, M. P. Shcheglov, and M. V. Pavlenko

Ioffe Physicotechnical Institute, Russian Academy of Sciences, Politekhnicheskaya ul. 26, St. Petersburg, 194021 Russia

Abstract—Spectra of deep centers in a lightly doped 6*H*-SiC substrate having regions with different degrees of structural perfection were investigated. It is found that the concentrations of the majority of deep centers are independent of the dislocation density in a given region of the sample. The obtained results and published data lead to the conclusion that the concentration of silicon vacancies is independent of the degree of the structural perfection of 6*H*-SiC. © *2001 MAIK "Nauka/Interperiodica".*

One of the main factors hindering the large-scale manufacture of semiconductor devices on SiC substrates grown by the modified Lely method is the insufficiently high quality of this material. The advances of recent years substantially reduced the density of the most undesirable structural defects with respect to device applications, that is, micropipes [1, 2]. Presumably, it will be possible in the near future to lower the content of micropipes to such an extent that their effect on the characteristics of SiC devices will become negligible. Investigations now aimed at lowering the dislocation density are in the forefront. It was shown in [3] that, at a dislocation density $\gtrsim 10^3$ over the working area of a device, the breakdown voltage decreases and reverse currents increase. At the same time, the problem of the influence exerted by dislocations on the type and concentration of deep centers in SiC remains poorly studied even though deep centers can strongly affect the lifetime of minority carriers and their diffusion length, transistor gain, etc.

The aim of this study was to analyze the spectrum of deep centers in relation to the degree of structural perfection of 6*H*-SiC substrates.

Lightly doped substrates grown by the modified Lely method were selected for measurements. The structural perfection of the substrates was assessed by X-ray topography and X-ray diffraction analysis. Topographs obtained by the back reflection method were used to distinguish regions with strongly different degrees of structural perfection in the substrates [4]. Figure 1 shows a topograph of such a sample [$(10\bar{1}.15)$ reflection, CuK_α radiation)]. The topograph reveals a nonuniform distribution of structural defects over the sample area and demonstrates regions with uniform distribution of basal dislocations with a density of $<10^5$ cm^{-2} and highly imperfect regions characterized by pronounced misorientations, the formation of dislocation boundaries, and the presence of a great number of pores.

Schottky diodes were formed by magnetron sputtering of Ni on the wafer surface ($\varnothing \approx 600$ μm) (Fig. 2). X-ray diffraction patterns characterizing the local disordering of the sample structure were recorded at the sites of Schottky diodes. The measurements were made with Schottky diodes formed in areas with highly different degrees of structural perfection. The half-widths of rocking curves (ω) were measured in a double-crystal arrangement for the (00012) reflection in CuK_α radiation. The scatter of the half-widths ranged from 11″ to 70″, which is in good agreement with the topographic data (Fig. 1).

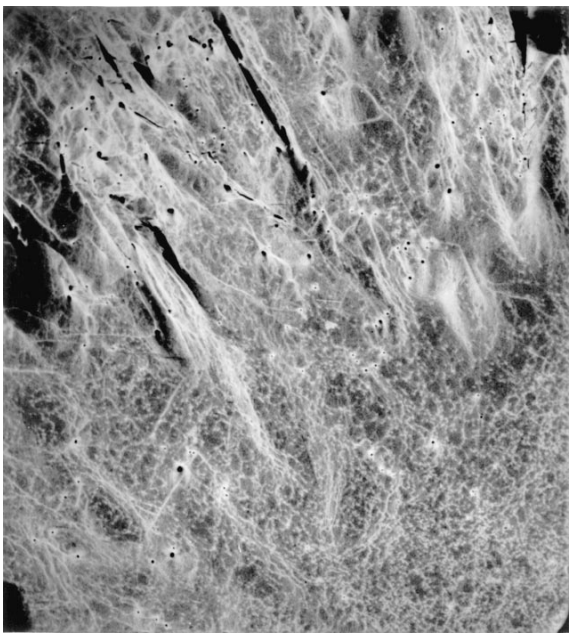

Fig. 1. X-ray topograph of 6*H*-SiC sample. $(10\bar{1}.15)$ reflection, CuK_α radiation.

1063-7826/01/3512-1372$21.00 © 2001 MAIK "Nauka/Interperiodica"

Table 1. Parameters of observed deep levels

Type of center	Reference	Energy position $E_c - E$, eV	Electron capture cross section σ, cm^2	Concentration, 10^{15} cm^{-3}
$E_1^{0/+}$	[8]	0.28	$>2.4\times10^{-15}$	
$E_2^{0/+}$	[8]	0.2	$>5.5\times10^{-15}$	
X_1	[*]	0.305	10^{-12}	0.1–2
X_2	[*]	0.206	4×10^{-14}	0.1–1.6
E_1	[5]	0.403	2×10^{-13}	1.7–3
E_2	[5]	0.455	2×10^{-13}	1.3–2.5
Z_1/Z_2	[5]	0.65	4×10^{-15}	0.7
R	[7]	1.2	2×10^{-15}	3

* This study.

The DLTS measurements were performed using the so-called current DLTS (*i*-DLTS), since the series resistance of the sample was too high below room temperature. The DLTS spectrum revealed five kinds of deep centers, three of which are well known from the literature: E_1/E_2 [5] (or *S* center [6, 7]), Z_1/Z_2 (E_c – 0.65 eV) [5], and *R* [E_c – (1.1–1.2) eV] [6, 7], the other two centers, X_1 and X_2, are new. It is noteworthy that the parameters of these two centers are close to those of the $E_1^{0/+}$ and $E_2^{0/+}$ centers observed in [8]. According to the model proposed in [8], these levels correspond to the donor states of two negative-*U* centers, whose acceptor states are the known centers E_1/E_2. The authors of [8] also mentioned that the signal from the $E_2^{0/+}$ and $E_2^{0/+}$ centers only appeared at the filling pulse duration of $t \lesssim$ 300 ns and also upon illumination of the sample with 470 nm light before the filling pulse. Without additional pulsed illumination and at $t \gtrsim 100$ μs, the DLTS signal from the $E_2^{0/+}$ and $E_1^{0/+}$ centers disappeared, with a peak corresponding to the E_0 center (E_c – 0.2 eV, $\sigma \approx 1.2\times10^{-18}$ cm^2) appearing instead. No illumination was used in our experiments, and the filling pulse duration was $t \approx 1$ ms. Thus, there is no way of maintaining that the X_1 and X_2 centers observed in this study and the $E_1^{0/+}$ and $E_2^{0/+}$ centers described in [8] are identical.

The parameters of all the observed centers and the scatter of their concentrations over the sample area are presented in Table 1.

The concentrations of E_1/E_2, X_1, and X_2 centers and also the densities $N_d - N_a$ in Schottky diodes with different degrees of crystal lattice imperfection (ω) are presented in Table 2. As follows from the obtained data, there is virtually no dependence of the concentration of the E_1/E_2, *R*, and Z_1/Z_2 centers and $N_d - N_a$ on the degree of structural perfection, whereas for the concentration of the X_1 and X_2 centers we have a nonmonotonic dependence on ω, with these concentrations varying dramatically with ω (see Table 2). It should be noted that these variations, having the form of abrupt changes, occurred in antiphase; i.e., we observed a maximum in the concentration of the X_1 center and a minimum in that of the X_2 center at ω ≈ 20″–22″, and, contrariwise, a minimum in [X_1] and maximum in [X_2] at 17″ and 53″.

Apparently, the varied degree of crystal structure imperfection may affect the concentrations of silicon

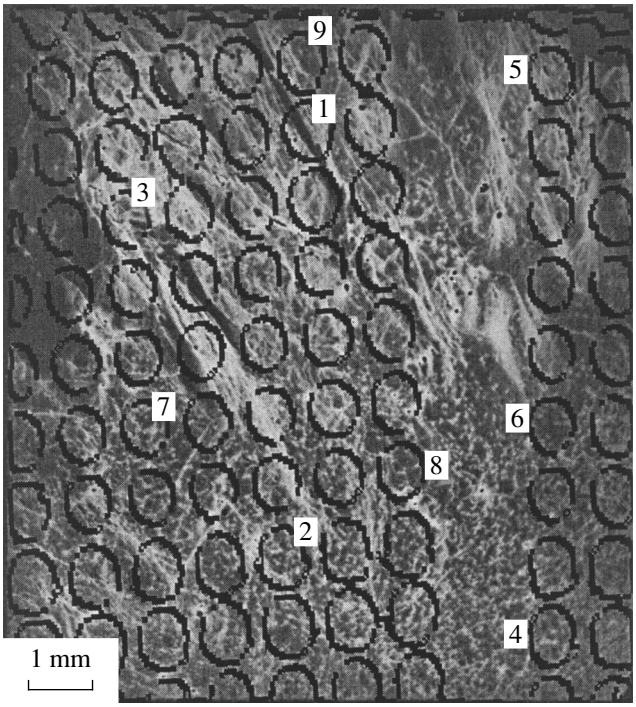

Fig. 2. Map of the arrangement of Schottky diodes projected onto an X-ray topographic image. Circles show locations of Schottky diodes on the wafer. The numbers of Schottky diodes in the map correspond to those in Table 2.

Table 2. Concentrations of X_1, X_2, E_1/E_2 centers and $N_d - N_a$ values in relation to ω

Schottky diode no. (see Fig. 2)	ω	$N_d - N_a$, 10^{15} cm^{-3}	Deep center concentration, 10^{15} cm^{-3}			
			N_{X_1}	N_{X_2}	N_{E_1}	N_{E_2}
7	11″	7.45	–	2	2.1	1.7
2	17″	6.6	≈0.2	1.3	1.8	1.3
8	17″	8.23	≈0.5	1.85	2.6	1.9
4	20″	11.6	1.2	≈0.1	2.1	2.2
6	22″	8.83	1.6	0.8	2.7	2
9	28″	6.6	–	1.4	1.7	1.3
3	53″	8.3	≈0.1	1.5	3	2.5

and carbon vacancies, V_{Si} and V_C. It is known from ESR data that the structure of the Z_1/Z_2 and R centers is a $V_{Si} + V_C$ divacancy [9–11], and that of the E_1/E_2 center, a complex of silicon vacancies [12]. Since the concentration of carbon vacancies is several times that of silicon vacancies [13], the key factor in the formation of all three centers is the concentration of V_{Si}. The fact that the concentration of the given centers was virtually the same at all points of the sample indicates that the V_{Si} concentration depends only slightly on structural defects.

Accounting for the observed variations of the concentrations of the X_1 and X_2 centers with increasing half-width ω is presently difficult because of the lack of any data on the possible structure of these centers.

Thus, two new types of centers have been observed in 6*H*-SiC, X_1 (E_c – 0.3 eV) and X_2 (E_c – 0.2 eV), and their concentrations heavily depend on the structural perfection of a crystal. For other deep centers—*R*, Z_1/Z_2, and E_1/E_2—that are more characteristic of 6*H*-SiC, there is virtually no dependence of this kind. Taking into account the published data on the structure of these centers, we may assume that changes in the dislocation density in 6*H*-SiC have no effect on the concentration of silicon vacancies in this material.

It is of practical importance that the concentration of deep centers that are most typical of 6*H*-SiC is independent of the structural quality of the material, since this enables a better substantiated comparison of results obtained in studying deep centers in different samples (or in regions with different degrees of structural perfection within the same sample).

REFERENCES

1. C. H. Carter, V. F. Tsvetkov, R. C. Glass, *et al.*, Mater. Sci. Eng., B **61–62**, 1 (1999).
2. C. H. Carter, Jr., R. Glass, M. Brady, *et al.*, Mater. Sci. Forum **353–356**, 3 (2001).
3. Q. Wahab, A. Ellison, A. Henry, *et al.*, Appl. Phys. Lett. **76**, 2725 (2000).
4. Yu. M. Tairov and V. F. Tsvetkov, J. Cryst. Growth **43**, 209 (1978).
5. H. Zhang, G. Pensl, A. Dorner, and S. Leibenzeder, in *Extended Abstracts of the Electrochemical Society Meeting, 1989*, p. 714.
6. M. M. Anikin, A. A. Lebedev, A. L. Syrkin, *et al.*, in *Extended Abstracts of the Electrochemical Society Meeting, 1989*, p. 699.
7. M. M. Anikin, A. N. Andreev, A. A. Lebedev, *et al.*, Fiz. Tekh. Poluprovodn. (Leningrad) **25**, 328 (1991) [Sov. Phys. Semicond. **25**, 198 (1991)].
8. C. G. Hemmingsson, N. T. Son, and E. Janzén, Appl. Phys. Lett. **74**, 839 (1999).
9. T. Dalibor, G. Pensl, H. Matsunami, *et al.*, Phys. Status Solidi A **162**, 199 (1997).
10. A. I. Veĭnger, V. A. Il'in, Yu. M. Tairov, and V. F. Tsvetkov, Fiz. Tekh. Poluprovodn. (Leningrad) **15**, 1557 (1981) [Sov. Phys. Semicond. **15**, 902 (1981)].
11. A. A. Lebedev, A. I. Veĭnger, D. V. Davydov, *et al.*, Fiz. Tekh. Poluprovodn. (St. Petersburg) **34**, 897 (2000) [Semiconductors **34**, 861 (2000)].
12. A. Kawasuso, F. Redmann, R. Krause-Rehberg, *et al.*, Mater. Sci. Forum **353–356**, 537 (2001).
13. N. D. Sorokin, Yu. M. Tairov, V. F. Tsvetkov, and M. A. Chernov, Kristallografiya **28**, 910 (1983) [Sov. Phys. Crystallogr. **28**, 539 (1983)].

Translated by M. Tagirdzhanov

Semiconductors, Vol. 35, No. 12, 2001, pp. 1375–1377. Translated from Fizika i Tekhnika Poluprovodnikov, Vol. 35, No. 12, 2001, pp. 1437–1439.

SEMICONDUCTOR STRUCTURES, INTERFACES, AND SURFACES

The Contact of Metal with Silicon Carbide: Schottky Barrier Height in Relation to SiC Polytype

S. Yu. Davydov*, A. A. Lebedev*, O. V. Posrednik, and Yu. M. Tairov****

** Ioffe Physicotechnical Institute, Russian Academy of Sciences, Politekhnicheskaya ul. 26, St. Petersburg, 194021 Russia*

*** St. Petersburg State University of Electrical Engineering, St. Petersburg, 197376 Russia*

Submitted April 12, 2001; accepted for publication April 20, 2001

Abstract—The results obtained in measuring the Schottky barrier height Φ_b^n for a chromium contact with 8*H*-, 6*H*-, 15*R*-, 27*R*- and 4*H*-SiC silicon carbide polytypes with *n*-type conduction are analyzed in terms of a simple model. It is shown that the Φ_b^n value is proportional to the concentration of silicon vacancies in the polytypes. The results of Φ_b^n measurements for palladium and platinum contacts to silicon carbide polytypes are discussed. © *2001 MAIK "Nauka/Interperiodica".*

1. The question of how the Schottky barrier height Φ_b^n can be calculated for a metal–semiconductor contact still remains a topical problem in the theory of semiconductors despite many years of investigations in this field [1]. Of indubitable interest in this connection are the surface-barrier structures based on silicon carbide (see, e.g., [2]). SiC crystals are primarily of interest in that they form a great number of polytypes differing from one another only in the ratio of the number of hexagonal and cubic sites, which can be characterized by the degree of hexagonality *D* [3]. The Φ_b values for various SiC polytypes in contact with one and the same metal are different, which was convincingly demonstrated in [4] for the example of the Cr–SiC system.

Basically, the purely cubic SiC modification (3*C*) differs from the purely hexagonal modification (2*H*) only in the arrangement of third neighbors. Since most of the properties of a solid are determined by the interaction with nearest (at most, second-nearest) neighbors, the polytypism of silicon carbide must affect its properties only in the crystallographic sense, i.e., it must determine the number of irreducible tensor elements characterizing a given physical quantity. It was, however, demonstrated in [4] that the Schottky barrier height Φ_b at the Cr–SiC interface is directly proportional to the degree of hexagonality D. Since crystallography bears no relation to this issue, the dependence of Φ_b on *D* can only be accounted for using the long known fact that the concentration of carbon (V_C) and silicon (V_{Si}) vacancies in silicon carbide exerts a strong, if not decisive, influence on its polytypism [3–6].

To account for the pattern discovered in [4], this study relies upon the model originally suggested in [7, 8] and modified in [9].

2. In terms of the model [7–9], a semiconductor in contact with a metal is characterized by a surface defect state $|d\rangle$ whose energy E_d lies within the band gap. The interaction of the level $|d\rangle$ with the metal can be described by the Hamiltonian

$$H = \sum_k \varepsilon_k c_k^+ c_k + E_i d_i^+ d_i + V\sum_k (c_k^+ d + \text{h.c.}). \quad (1)$$

Here ε_k is the energy of electrons in the metal, *V* is the matrix element of hybridization of a metallic $|k\rangle$ and a defect $|d\rangle$ states, c_k^+ is the operator of electron creation in the state $|k\rangle$, and d^+ is the operator of electron creation in the state $|d\rangle$. On the assumption that the level of the localized defect state $|d\rangle$ is overlapped with the wide conduction band of the metal, its occupation number n_d can be readily found to be

$$n_d = \pi^{-1}\tan^{-1}[(E_d - E_F)/\Gamma], \quad (2)$$

where Γ is the half-width of the defect quasi-level, and E_F is the Fermi level. The electron tunneling between the metal and defects at the contact gives rise to a potential barrier

$$\Delta\phi = -4\pi e^2 \lambda N_d q_q, \quad (3)$$

where 2λ is the thickness of the dipole layer at the contact, N_d is the surface concentration of defect states, and q_d is the charge localized in the $|d\rangle$ state, i.e., $q_d = -n_d$ if the state $|d\rangle$ was unoccupied before the contact formation and $q_d = 1 - n_d$ if it was occupied (in the first case, electrons pass from the metal to the empty defect level, and, in the second, they go from the defect into the metal).

Input data and results of calculation

SiC polytype	8*H*	6*H*	15*R*	27*R*	4*H*
Φ_b^n, eV	0.85	1.15	1.15	1.25	1.50
N_{Si}^s, 10^{13} cm^{-2}	4.48	5.43	6.30	7.11	8.11
N_d, 10^{13} cm^{-2}	2.46	3.58	3.57	3.94	4.86
N_{Si}^s/N_d	1.82	1.52	1.76	1.80	1.67
Φ_b^n/N_d, eV cm^2	0.35	0.32	0.32	0.32	0.31
E_F/E_g	0.70	0.62	0.62	0.57	0.54

Note: E_g values for all polytypes except 27*R* were taken from [4], and for the 27*R* polytype, from [14]; Φ_b^n was taken from [4]; the surface concentrations of silicon vacancies, N_{Si}^s, were calculated using data reported in [6] for the bulk material.

The Fermi level position with respect to the valence band top is given by

$$E_F = \chi + E_g - \phi_m - \Delta\phi, \quad (4)$$

where χ is the electron affinity, E_g is the band gap, and ϕ_m is the metal work function. The Schottky barrier height is E_F for *p*-type semiconductors and $(E_g - E_F)$ for the *n*-type.

3. The results obtained in [4] will be analyzed using the following approach. We assume that the Fermi level E_F is pinned at the defect level E_d. Then, it follows from (2) that $n_d = 0.5$ and the state $|d\rangle$ is originally (before the contact with metal) unoccupied. The presence of such a level, related to a silicon vacancy, has been confirmed by calculation [10]. Thus, $q_d = -0.5$ in expression (3). Now we take from [4] an experimental Φ_b^n value equal in terms of the employed model to

$$\Phi_b^n = \phi_m - \chi + \Delta\phi \quad (5)$$

(the superscript indicates the conduction type of SiC). Then we subtract $(\phi_m - \chi)$ from this experimental value. The electron affinities for SiC polytypes are unfortunately unavailable. Different authors use different χ values lying within the range from 4 to 4.4 eV (see, e.g., [11, 12]). In what follows, we assume for all polytypes that $\chi = 4.4$ eV (here we introduce a certain arbitrariness due to the lack of appropriate experimental data). The work function of chromium $\phi_m = 4.58$ eV [13] (we use values for polycrystals). Using the above values, we find N_d (see table). The calculated results seem to be quite reasonable. First, the Fermi level is found to lie higher than the midgap, as assumed in [4]. Second, the N_{Si}^s/N_d ratio remains approximately the same for all of the polytypes considered. Thus, we are forced to admit that, for the problem in question, the model *d* defects correspond to Si vacancies in silicon carbide (the fact that $N_{\mathrm{Si}}^s/N_d < 1$ is not surprising, since, as noted in [4], the presence of a thin SiO_2 layer at the contact interface lowers the density of surface states). Hence, it follows that silicon vacancies are primarily responsible for the different heights of Schottky barriers in different SiC polytypes. Moreover, it follows from the calculation that $\Phi_b^n \propto N_d$ and, consequently, $\Phi_b^n \propto N_{\mathrm{Si}}^s$. Unfortunately, it is impossible to relate, within our approach, the Schottky barrier height to the degree of hexagonality *D* and thereby substantiate theoretically the linear dependence of Φ_b^n on *D* observed in [4]. It should, however, be mentioned that D is proportional to N_{Si}^s [3, 6].

In order to verify the results obtained above, let us analyze the data of [15] where palladium and platinum contacts to 4*H*-, 6*H*-, and 15*R*-SiC were studied. Since the work functions of Pd and Pt are, respectively, 4.80 and 5.32 eV, then, taking N_d values from the table, we obtain the following results. For palladium contacts to 6*H*-, 15*R*-, and 4*H*-SiC, we have Φ_b^n = 1.37, 1.37, and 1.72 eV, respectively. Current–voltage measurements give, respectively, 1.27, 1.22, and 1.56 eV; virtually the same values are yielded by ballistic electron-emission spectroscopy [15]. For platinum contacts to 6*H*- and 4*H*-SiC, calculation gives Φ_b^n = 1.89 and 2.24 eV, whereas current–voltage measurements yield 1.26 and 1.48 eV, and ballistics, 1.34 and 1.58 eV [15]. The agreement for palladium should be considered satisfactory, whereas, in the case of platinum, our results exceed the experimental values by a factor of 1.5. Among the possible reasons for the discrepancy may be both the different (for platinum and chromium) concentrations of defect states, N_d, and, possibly, the lowered (by some impurities) effective work function of platinum.

Thus, we could relate, using a simple model, the Schottky barrier height Φ_b^n at the interface between a metal and a silicon carbide polytype to the concentration of silicon vacancies and, as a result, obtain a satisfactory calculated Φ_b^n value for the Pd–SiC contact.

To conclude, we note that an alternative approach to the problem of contact between silicon polytypes and various metals, based on the adsorption concept, was formulated in [16, 17], where the barrier height was related to electronegativity. The obtained relationship seems to be rather interesting, since already in [3] the direct proportionality of the effective charge of silicon atoms to the degree of hexagonality *D* was established empirically. On the other hand, it follows from calculations made in [18] for a defect-free crystal that the ionicities of different SiC polytypes differ by less than 0.1%. Consequently, the electronegativity, effective

charge, and ionicity are presumably related to the polytype imperfection. We are going to study this issue further using the approach developed in [1, 16, 17, 19].

ACKNOWLEDGMENTS

This study was supported in part by the Russian Foundation for Basic Research (project no. 00-02-16688) and Scientific Programs RM/M65 and LNE66.

REFERENCES

1. W. Mönch, Rep. Prog. Phys. **53**, 221 (1990).
2. *Proceedings of the 3rd European Conference on Silicon Carbide and Related Materials, ECSCRM-2000, Kloster Banz, Germany*, Ed. by G. Pensl, D. Stephani, and M. Hundhausen (Trans. Tech. Publ., Switzerland, 2001).
3. N. D. Sorokin, Yu. M. Tairov, V. F. Tsvetkov, and M. A. Chernov, Kristallografiya **28**, 910 (1983) [Sov. Phys. Crystallogr. **28**, 539 (1983)].
4. R. G. Verenchenko, V. I. Sankin, and E. I. Radovanova, Fiz. Tekh. Poluprovodn. (Leningrad) **17**, 1757 (1983) [Sov. Phys. Semicond. **17**, 1123 (1983)].
5. Yu. A. Vodakov, G. A. Lomakina, and E. N. Mokhov, Fiz. Tverd. Tela (Leningrad) **24**, 1377 (1982) [Sov. Phys. Solid State **24**, 780 (1982)].
6. A. A. Lebedev, Fiz. Tekh. Poluprovodn. (St. Petersburg) **33**, 769 (1999) [Semiconductors **33**, 707 (1999)].
7. R. Ludeke, G. Jezequel, and A. Tabel-Ibrahimi, Phys. Rev. Lett. **61**, 601 (1988).
8. R. Ludeke, Phys. Rev. B **40**, 1947 (1989).
9. S. Yu. Davydov, A. A. Lebedev, and S. K. Tikhonov, Fiz. Tekh. Poluprovodn. (St. Petersburg) **31**, 597 (1997) [Semiconductors **31**, 506 (1997)].
10. P. Deak, A. Gali, J. Miro, *et al.*, Mater. Sci. Forum **264–268**, 279 (1998).
11. J. R. Waldrop, J. Appl. Phys. **75**, 4548 (1994).
12. A. N. Andreev, A. A. Lebedev, M. G. Rastegaeva, *et al.*, Fiz. Tekh. Poluprovodn. (St. Petersburg) **29**, 1828 (1995) [Semiconductors **29**, 955 (1995)].
13. *Handbook of Physical Quantities*, Ed. by I. S. Grigoriev and E. Z. Meilikhov (Énergoizdat, Moscow, 1991; CRC Press, Boca Raton, 1997).
14. V. I. Gavrilenko, A. M. Grekhov, D. V. Korbutyak, and V. G. Litovchenko, *Optical Properties of Semiconductors: A Handbook* (Naukova Dumka, Kiev, 1987).
15. H.-J. Im, B. Kaczer, J. P. Pelz, *et al.*, Mater. Sci. Forum **264–268**, 813 (1998).
16. W. Mönch, in *Control of Semiconductor Interfaces*, Ed. by I. Ohdomari, M. Oshima, and A. Hiraki (Elsevier, Amsterdam, 1994), p. 169.
17. V. van Elsbergen, T. U. Kampen, and W. Mönch, J. Appl. Phys. **79**, 316 (1996).
18. G. Wellenhofer, K. Karch, and P. Pavonet, Inst. Phys. Conf. Ser. **142** (2), 301 (1996).
19. S. Yu. Davydov and S. K. Tikhonov, Fiz. Tverd. Tela (St. Petersburg) **37**, 2749 (1995) [Phys. Solid State **37**, 1514 (1995)].

Translated by M. Tagirdzhanov

Semiconductors, Vol. 35, No. 12, 2001, pp. 1378–1382. Translated from Fizika i Tekhnika Poluprovodnikov, Vol. 35, No. 12, 2001, pp. 1440–1444.

LOW-DIMENSIONAL SYSTEMS

Ostwald Ripening of Quantum-Dot Nanostructures

R. D. Vengrenovich*, Yu. V. Gudyma, and S. V. Yarema

Fed'kovich State University, ul. Kotsyubinskogo 2, Chernovtsy, 58012 Ukraine

** e-mail: general@chdu.cv.ua*

Submitted January 17, 2001; accepted for publication April 26, 2001

Abstract—We suggest a scenario for the formation of quantum dots during Ostwald ripening of three-dimensional islands grown heteroepitaxially in the Stranski–Krastanow mode. We demonstrate that the size-distribution function narrows down and the variance decreases noticeably if the growth proceeds through dislocation diffusion followed by the detachment of dislocations from island bases. Plausible reasons for termination of the Ostwald ripening of the islands are discussed. © *2001 MAIK "Nauka/Interperiodica".*

Quantum dots (QDs) are heterostructures in which charge carriers are spatially confined in all three dimensions. As a result, the energy separation between electron levels far exceeds the thermal energy [1–3]. This very important property and the real possibility of tuning the energy spectrum by changing the geometric size and shape of QDs are crucial factors in their device application. QD-based light-emitting diodes and lasers are expected to be developed in the near future. However, QDs are difficult to prepare, and this hinders their widespread use.

One of the most common methods of QD preparation is heteroepitaxial growth in the Stranski–Krastanow mode: initially, the growth proceeds in the layer-by-layer [two-dimensional (2D)] mode, and then 3D islands form on the substrate covered with a wetting layer of the deposited material [4–6]. The change in the growth characteristics is explained by the fact that, as the layer thickness increases, the elastic-strain energy in lattice-mismatched systems tends to decrease via the formation of nanostructures in the form of isolated islands (the Ostwald ripening). On the other hand, as the wetting layer attains the critical thickness, plastic deformation can occur via the introduction of matrix dislocations, which also lowers the strain energy. Within thermodynamic approximation, the above-mentioned ways for strain relaxation in the wetting layers are often considered to be mutually exclusive, since completely formed QDs are strained, dislocation-free, coherent islands. Actual QDs apparently form as a result of a complex self-organization process, involving both equilibrium and nonequilibrium kinetic processes and their combination [2].

As the islands grow, the strain energy increases owing to the lattice mismatch between the islands and the wetting layer. Therefore, further strain relaxation may proceed by elastic interaction between strain fields of the islands and the matrix dislocations: the dislocations are captured and pinned near island bases. Thus, under conditions of surface diffusion, the rather slow process of the Ostwald ripening gives way to the faster process of the island growth controlled by dislocation diffusion. The growth rate of the islands growing via dislocation diffusion exceeds that of as yet unrelaxed islands, which grow via surface diffusion. Because of the difference in the growth rate, many of the growing islands begin to dissolve, since the critical radius r_k increases to the value corresponding to the greater, relaxed islands. As a result, the spread of particle radii about a mean value (i.e., the variance) decreases, and, consequently, the island-size distribution narrows down, which has been observed experimentally [7–9].

The heteroepitaxial nanostructures are nonequilibrium systems; therefore, they are described in the kinetic approximation. It is repeatedly emphasized [10–13] that the Ostwald ripening theory most adequately describes late stages of the island growth. In the context of this theory [14, 15], we shall determine the function of the island-size distribution. To simplify calculations, we presume that the islands are disk-shaped with constant height h and various radii r. Under steady-state conditions, the islands grow (or dissolve) owing to the diffusion flux of the material along the dislocation grooves, which form when the dislocations crop out at the surface of the wetting layer. We shall presume that the number of dislocation lines which terminate at the island base, Z, is the same for all islands and is constant in time. Such a mechanism of growth (dissolution) is possible if the matter flux due to dislocation diffusion, j, is much greater than the flux due to surface diffusion; i.e., if the following inequality holds:

$$D_s^{(d)} Zd\left(\frac{dC}{dR}\right)_{R=r} \gg D_s 2\pi r\left(\frac{dC}{dR}\right)_{R=r}. \qquad (1)$$

Here, $D_s^{(d)}$ is the coefficient of diffusion along the dislocation grooves, D_s is the coefficient of surface diffusion, $(dC/dR)_{R=r}$ is the gradient of concentration of the deposited material at the island boundary, Z is the number of dislocations fixed at the island base, and d is the

diameter of the dislocation groove ($d = 2\sqrt{2q/\pi}$ and $b^2 \le q \le 60b^2$, where q is the cross-section area of the dislocation groove, and b is the Burgers vector). Inequality (1) imposes a restriction on the size of the islands growing by the mechanism under consideration. From inequality (1), it follows that

$$r \ll \frac{Zd}{2\pi}\frac{D_s^{(d)}}{D_s}. \quad (2)$$

The growth rate of an isolated island can be determined from the condition

$$\frac{d}{dt}(\pi r^2 h) = j v_m, \quad (3)$$

where the flux of the material j is given by the left-hand side of inequality (1), and v_m is the volume of an adatom. Following Vengrenovich [16], we obtain

$$\frac{dr}{dt} = \frac{A}{r^2}\left(\frac{1}{r_c} - \frac{1}{r}\right), \quad (4)$$

where $A = \frac{ZC_\infty \sigma v_m^2 D_s^{(d)}}{kTh\ln(l)}\sqrt{\frac{2q}{\pi}}$, r_c is the critical radius, k is the Boltzmann constant, T is the temperature, σ is the specific surface energy, C_∞ is the equilibrium concentration at the island boundary, and l is the so-called screening distance [$C(R) = \langle C\rangle|_{R=lr}$, where $l = 2$ or 3]. The adatom concentration at the distance R from the center of the island $C(R) = \frac{\langle C\rangle - C'}{\ln(l)}\ln\frac{R}{r} + C'$, where $\langle C\rangle$ is the average concentration of atoms on the substrate, and C' is the concentration on the island surface.

Equation (4) allows us to determine the maximum radius of the islands growing via the dislocation-related mechanism, r_g. According to Vengrenovitch [17], the following condition should be met:

$$\left.\frac{d}{dr}\left(\frac{\dot r}{r}\right)\right|_{r=r_g} = 0. \quad (5)$$

From Eq. (5), we obtain

$$r_g = \frac{4}{3}r_c. \quad (6)$$

Henceforth, $\dot r \equiv \frac{dr}{dt}$.

Integrating Eq. (4) for $r = r_g$, we determine, taking formula (6) into account, the time dependences of r_g and r_c:

$$r_g = \left(\frac{4}{3}At\right)^{1/4}, \quad (7)$$

$$r_c = \left(\left(\frac{3}{4}\right)^3 At\right)^{1/4}. \quad (8)$$

The function of the island-size distribution is written as [17]

$$f(r,t) = \varphi(r_g)g(u), \quad (9)$$

where $g(u)$ is the distribution of the islands by relative sizes $u = \frac{r}{r_g}$. The quantity $\varphi(r_g)$, appearing in (9), can be determined from the law of conservation of the island-condensate mass M

$$M = \kappa\int_0^{r_g} r^2 f(r,t)dr, \quad (10)$$

where $\kappa = \pi h\rho$, and ρ is the density of the island material. Substituting (9) into (10), we obtain

$$\varphi(r_g) = \frac{Q}{r_g^3}, \quad (11)$$

where $Q = \frac{M}{\kappa\int_0^1 u^2 g(u)du}$.

To determine $g(u)$, we use the continuity equation

$$\frac{\partial}{\partial t}(f(r,t)) + \frac{\partial}{\partial r}(f(r,t)\dot r) = 0. \quad (12)$$

Inserting values of $f(r, t)$ and $\dot r$ into Eq. (12) and going from differentiation with respect to r and t to differentiation with respect to u, we can perform the separation of variables appearing in Eq. (12). Then, Eq. (12) takes the form

$$\frac{dg(u)}{g(u)} = -\frac{3\vartheta_g + 3\frac{\vartheta}{u^4} - \frac{1}{u^3}\frac{d\vartheta}{du}}{u\vartheta_g - \frac{\vartheta}{u^3}}du. \quad (13)$$

Here, we take into account that $\frac{dr_g}{dt} = \vartheta_g\frac{A}{r_g^3}$, $\frac{du}{dr} = \frac{1}{r_g}$, $\frac{du}{dr_g} = -\frac{u}{r_g}$, $\vartheta = \frac{\dot r r^3}{A} = \frac{4}{3}u - 1$, and $\vartheta_g = \vartheta|_{u=1} = \frac{1}{4}$.

Integrating Eq. (13), we obtain

$$g(u) = \frac{u^3\exp\left(-\frac{1}{3(1-u)}\right)\exp\left(-\frac{1}{9\sqrt{2}}\arctan\left(\frac{u+1}{\sqrt{2}}\right)\right)}{(1-u)^{25/9}(u^2+2u+3)^{29/18}}. \quad (14)$$

In Fig. 1, we compare the size distributions calculated for various mechanisms of growth during Ostwald ripening. Curve *1* [$g_1(u) = u(1-u)^{-4}\exp\left(-\frac{2}{1-u}\right)$] corresponds to the island growth controlled by kinetic

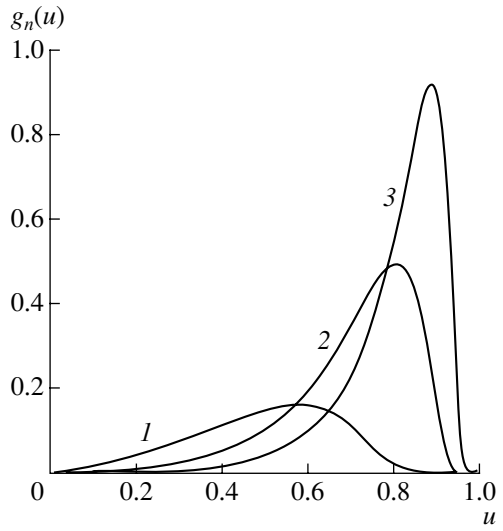

Fig. 1. Size distributions calculated for various mechanisms of the island growth during the Ostwald ripening: the growth controlled by (*1*) kinetic processes at the boundary, (*2*) surface diffusion, and (*3*) dislocation diffusion.

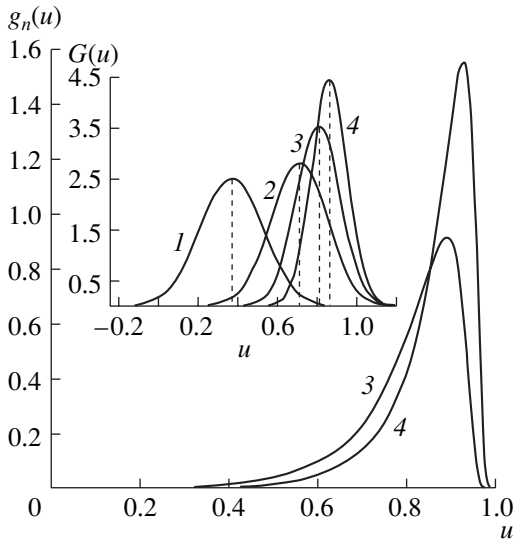

Fig. 2. Size distributions described by (*3*) formula (14) and (*4*) formula (20). The inset shows Gaussian distributions of particles by sizes; curves *1–4* correspond to the four above-mentioned growth mechanisms.

processes at the boundary [16]. Curve *2* [$g_2(u) = u^2(1-u)^{-28/9}(u+2)^{-17/9}\exp\left(-\frac{2/3}{1-u}\right)$] was calculated on the assumption of surface diffusion [16]. Curve *3* corresponds to the distribution (14). The values of the variance $D = \langle u^2\rangle - \langle u\rangle^2$ are $D_1 = 0.0254$, $D_2 = 0.0199$, and $D_3 = 0.0127$, respectively. Thus, distribution (14) (curve *3*) is the narrowest and has the smallest value for the variance. Curves *1* and *2* correspond to the distributions modified for the surface, which were obtained previously by Wagner [15] and Lifshits and Slezov [14], respectively.

The ripening of the islands under the conditions of dislocation-related diffusion, as well as surface diffusion, is, apparently, a fast process resulting in the formation of faceted QDs at the final stage. Therefore, at the considered stage of Ostwald ripening, the system still has high strain energy. During the ripening, this energy decreases further owing to changes in the lattice constant of the island material, and this results in the decrease in the lattice mismatch between the island and the wetting layer [13]. The island lattice adjusts to the lattice of the wetting layer. In turn, the decrease in the strain energy leads to the weakening of the bond between the dislocations and the island. The dislocations start to break away from their pinning sites. Since the adjustment of the island lattice proceeds slowly, the strain relaxation at this stage is also a slow process. This means that the dislocations detach sequentially rather than simultaneously. Now, we cannot consider the number of dislocations Z pinned at the island base as being constant. Assuming that

$$Z = \frac{Z_0 d}{2\pi r}, \tag{15}$$

we can write the rate of the growth (dissolution) of an isolated island as

$$\frac{dr}{dt} = \frac{A_1}{r^3}\left(\frac{1}{r_c} - \frac{1}{r}\right), \tag{16}$$

where $A_1 = \frac{Z_0 d C_\infty \sigma v_{\mathbf{m}}^2 D_{\mathbf{s}}^{(d)}}{2\pi kTh\ln(l)}\sqrt{\frac{2q}{\pi}}$, Z_0 is the initial number of dislocations, and d is the diameter of the dislocation groove.

Repeating the foregoing calculations, we obtain from Eq. (16)

$$r_g = \frac{5}{4} r_c, \tag{17}$$

$$r_g = \left(\frac{5}{4} A_1 t\right)^{1/5}, \tag{18}$$

$$r_c = \left(\left(\frac{4}{5}\right)^4 A_1 t\right)^{1/5}. \tag{19}$$

In this case, the distribution function takes the form

$$g_4(u) = \frac{u^4 \exp\left(-\frac{0.2}{1-u}\right)\exp\left(-\frac{1}{8.6\sqrt{2}}\arctan(0.65u + 0.113)\right)}{(1-u)^\alpha (u+a)^\beta (u^2+bu+c)^\gamma}, \tag{20}$$

where $a \cong 1.65063$, $b \cong 0.34937$, $c \cong 2.42332$, $\alpha \cong 2.6$, $\beta \cong 1.46$, and $\gamma \cong 1.47$.

Figure 2 presents graphical representations of distributions (14) and (20). The inset shows the island-size distributions $G(u)$ for various growth mechanisms; these distributions were assumed to be Gaussian. The values of the mean particle size and the variance are the following: $\langle u_1 \rangle = 0.3692$ and $D_1 = 0.0254$ for curve *1*, $\langle u_2 \rangle = 0.711$ and $D_2 = 0.0199$ for curve *2*, $\langle u_3 \rangle = 0.8091$ and $D_3 = 0.0127$ for curve *3*, and $\langle u_4 \rangle = 0.8644$ and $D_4 = 0.0081$ for curve *4*. We can see that the detachment of the dislocations from the island perimeter during strain relaxation results in further narrowing of the size distribution. In addition, in transferring to the dislocation-related growth mechanism, the most probable size u' corresponding to the maximum of the $g(u)$ function increases, as does the most probable particle size $r' = u'r_g$. For example, $u' = 0.57$ and $r' = 0.57r_g$ for $n = 1$, $u' = 0.81$ and $r' = 0.81r_g$ for $n = 2$, $u' = 0.89$ and $r' = 0.89r_g$ for $n = 3$, and $u' = 0.93$ and $r' = 0.93r_g$ for $n = 4$. As u' increases, $g(u')$ increases, which means that the density of the islands of the most probable size increases.

This growth mechanism is possible if the mass flux to the island along the dislocations still exceeds the flux due to surface diffusion; i.e., in view of (15),

$$D_s^{(d)} d \frac{Z_0 d}{2\pi r} \left(\frac{dC}{dR}\right)_{R=r} \gg D_s 2\pi r \left(\frac{dC}{dR}\right)_{R=r}. \qquad (21)$$

Whence it follows that

$$r \ll \frac{d}{2\pi} \sqrt{Z_0 \frac{D_s^{(d)}}{D_s}}. \qquad (22)$$

If condition (22) is violated, in addition to the flow due to dislocation diffusion, we should also take into account the flow of the material due to surface diffusion.

At this stage, strain relaxation ultimately results in the complete detachment of the dislocations from the island perimeters followed by the take-up of these dislocations by the substrate. As a result, coherent, dislocation-free islands form. They are slightly strained, because the lattices of the islands and the wetting layer are not completely matched.

However, prior to the dislocation detachment, facets of the ripening islands start to develop. Along with the change in the lattice constant of the island material, this faceting leads to an additional decrease in the strain energy of the island condensate on the surface of the wetting layer. By the time when all dislocations will have broken away, all islands will have become faceted. Thus, QDs are coherent, slightly strained, dislocation-free faceted islands. As the facets develop, the rate of the island growth should decrease noticeably, as in the case of metal alloys subjected to dispersion hardening [18]. If the islands are faceted with quasi-equilibrium facets, then the size distribution is stable, and the supersaturation with adatoms is less than the effective value [19] required for the formation of nuclei and for their joining the island facets. Indeed, experimental size distributions often have a fixed density. This means that, at the final stage of the ripening, island growth slows down, and the island facets are quasi-equilibrium.

As found experimentally [20, 21], 3D islands can have, and as a rule do have, a shape that is more complex than a cylindrical one. It is also known that strain in the wetting layer and in the QDs depends heavily on the substrate thickness [22] and the distance to the wetting layer/substrate interface [23], respectively. Our scenario does not take into account these factors and, from this point of view, gives only a qualitative description.

REFERENCES

1. D. Bimberg, M. Grundmann, and N. N. Ledentsov, *Quantum Dot Heterostructures* (Wiley, Chichester, 1998).
2. N. N. Ledentsov, V. M. Ustinov, V. A. Shchukin, *et al.*, Fiz. Tekh. Poluprovodn. (St. Petersburg) **32**, 385 (1998) [Semiconductors **32**, 343 (1998)].
3. V. A. Shchukin and D. Bimberg, Rev. Mod. Phys. **71**, 1125 (1999).
4. Y.-W. Mo, D. E. Savage, B. S. Swartzentruber, and M. G. Lagally, Phys. Rev. Lett. **65**, 1020 (1990).
5. P. Müller and R. Kern, Microsc. Microanal. Microstruct. **8**, 229 (1997).
6. O. P. Pchelyakov, Yu. B. Bolkhovityanov, A. V. Dvurechenskiĭ, *et al.*, Fiz. Tekh. Poluprovodn. (St. Petersburg) **34**, 1281 (2000) [Semiconductors **34**, 1229 (2000)].
7. D. Leonard, K. Pond, and P. M. Petroff, Phys. Rev. B **50**, 11687 (1994).
8. F. M. Ross, J. Tersoff, and R. M. Tromp, Phys. Rev. Lett. **80**, 984 (1998).
9. D. E. Jesson, G. Chen, K. M. Chen, and S. J. Pennycook, Phys. Rev. Lett. **80**, 5156 (1998).
10. J. C. Kim, H. Rho, L. M. Smith, *et al.*, Appl. Phys. Lett. **73**, 3399 (1998).
11. Q. K. K. Liu, N. Moll, M. Scheffer, and E. Pehlke, Phys. Rev. B **60**, 17008 (1999).
12. J. A. Floro, M. B. Sinclair, E. Chason, *et al.*, Phys. Rev. Lett. **84**, 701 (2000).
13. L. G. Wang, P. Kratzer, N. Moll, and M. Scheffer, Phys. Rev. B **62**, 1897 (2000).
14. I. M. Lifshits and V. V. Slezov, Zh. Éksp. Teor. Fiz. **35**, 479 (1958) [Sov. Phys. JETP **8**, 331 (1959)].

15. C. Wagner, Z. Elektrochem. **65**, 581 (1961).
16. R. D. Vengrenovich, Ukr. Fiz. Zh. **22**, 219 (1977).
17. R. D. Vengrenovitch, Acta Metall. **30**, 1079 (1982).
18. V. I. Psarev and R. D. Vengrenovich, Izv. Vyssh. Uchebn. Zaved., Chern. Metall., No. 8, 16 (1966).
19. B. Honigmann, *Gleichgewichts- und Wachstumsformen von Kristallen* (D. Steinkopff, Darmstadt, 1958; Inostrannaya Literatura, Moscow, 1961).
20. Th. Wiebach, M. Schmidbauer, M. Hanke, *et al.*, Phys. Rev. B **61**, 5571 (2000).
21. Y. Wakayama, G. Gerth, P. Werner, *et al.*, Appl. Phys. Lett. **77**, 2328 (2000).
22. N. S. Chokshi and J. M. Millunckick, Appl. Phys. Lett. **76**, 2382 (2000).
23. I. Kegel, T. H. Metzger, P. Fratzl, *et al.*, Europhys. Lett. **45**, 222 (1999).

Translated by N. Izyumskaya

Semiconductors, Vol. 35, No. 12, 2001, pp. 1383–1389. Translated from Fizika i Tekhnika Poluprovodnikov, Vol. 35, No. 12, 2001, pp. 1445–1451.

LOW-DIMENSIONAL SYSTEMS

Kinetics of Exciton Photoluminescence in Low-Dimensional Silicon Structures

A. V. Sachenko, É. B. Kaganovich*, É. G. Manoĭlov, and S. V. Svechnikov

Institute of Semiconductor Physics, National Academy of Sciences of Ukraine, Kiev, 03028 Ukraine

** e-mail: dept_5@isp.kiev.ua*

Submitted March 5, 2001; accepted for publication May 11, 2001

Abstract—Time-resolved photoluminescence (PL) spectra have been measured at 90–300 K in the visible spectral range for porous nanocrystalline silicon films fabricated by laser deposition. The energy and time ranges in which the spectra were taken were 1.4–3.2 eV and 50 ns–10 μs, respectively. The correlation between PL characteristics (intensity, emission spectrum, relaxation times and their temperature dependence), structure, and dielectric properties (size and shape of Si nanocrystals, oxide phase of their coatings, porosity of films) has been studied. A model of photoluminescence is adopted, in which the absorption and emission of photons occur in quantum-size nanocrystals, and in which kinetically coupled subsystems of electron–hole pairs and excitons are involved in the radiative recombination. Possible mechanisms of the exciton Auger recombination in low-dimensional silicon structures are proposed. *© 2001 MAIK "Nauka/Interperiodica".*

1. INTRODUCTION

Nanocrystalline silicon (*nc*-Si) with high-yield photoluminescence (PL) in the visible spectral range at room temperature is, at least, a two-phase nanocomposite, where silicon nanocrystals (NC) (with a size satisfying conditions for quantum confinement) are located in a matrix, most frequently consisting of silicon oxide, including the porous SiO_x (porous silicon, *por*-Si). Starting from the works by Canham and co-authors [1, 2], the relation of the slow PL band in *por*-Si with radiative exciton annihilation has been considered repeatedly (see, e.g., [3, 4]). In the works by Keldysh with co-authors [5], it was shown that excitons have large binding energies in low-dimensional structures, because the former are embedded in a medium with a dielectric constant ε_2 that is lower than ε_1 in NC ($\varepsilon_2 < \varepsilon_1$) (the dielectric enhancement effect). The relation of the slow component of the red PL in *por*-Si with the low-dimensional phase Si:O:H at the NC/SiO_x interface [6] and with electronic states induced by the Si=O bonds for small-size NC ($d < 3$ nm) is discussed in the literature [7]. A model taking into account the modification of quantum states in NC by the surface potential have been considered [8]. There is also no agreement regarding the nature of the fast component of PL and recombination mechanisms responsible for the blue PL. This luminescence is usually traced back to silicon oxide defects [2, 9], but the interband recombination in NC is also discussed [10]. The combined character of the mechanism of visible PL in *nc*-Si, depending on structure features and PL measurement conditions, is discussed in many papers [2, 6–10].

The objective of this study was to ascertain the visible-PL mechanism in the *nc*-Si films obtained using laser-induced evaporation. To this end, we analyzed interrelations between characteristics of the time-resolved visible PL (intensity, radiation spectrum, relaxation times and their temperature dependence) in the 90–300 K temperature range and structural properties (size and shape of the silicon NC, oxide phase of their coating, and film porosity). In addition, exciton mechanisms of radiative and nonradiative recombination in *nc*-Si quantum structures and exciton Auger recombination mechanisms are discussed. Finally, a PL model in which both photon absorption and emission occur in quantum-size Si NC is considered in order to explain the obtained experimental data. Kinetically coupled subsystems of electron–hole pairs and excitons take part in recombination. It is believed that the exciton recombination contribution is large and the PL characteristics are related to the recombination of excitons localized in Si NC, since the exciton ground state binding energies in small NC can reach 1 eV. In addition, the nonradiative recombination in the case under consideration is assumed to be determined by the exciton Auger recombination. The high intensity of the *nc*-Si PL in comparison with the bulk crystal silicon (*c*-Si) results not only from enhancement of the radiative recombination channel, but also from suppression of the nonradiative one. The PL relaxation times lying in the 50 ns–1 ms range, observed at 90–300 K, are shown to be determined by the nonradiative times. The enhancement of the PL intensity, the longer time of its relaxation, and the red shift of the PL spectrum, observed upon oxidation of *nc*-Si, are related to the dielectric enhancement effect and to the more effective suppression of the nonradiative surface recombination channels in larger Si NCs. It is shown that a characteristic feature of the spectra of the fast PL component

(with characteristic time $\tau < 50$ ns) is their wide energy range from 1.4 to 3.2 eV and the presence of three bands: a central- and two side-bands (low- and high-energy ones). It is assumed that the high-energy (blue) band emission may be related not only with the interband recombination (between quantum levels), but also with the SiO_x matrix defects, whereas phonon-assisted transitions also contribute to the low-energy (red) band.

2. MEASUREMENT TECHNIQUE AND SAMPLES

The specific features of our experiment are the following: First, the PL properties of a wide variety of *nc*-Si samples, from silicon oxide films enriched in silicon to *por*-Si via intermediate structures containing Si NCs of various sizes in an SiO_x matrix of various porosity and content. Second, the time-resolved PL method was used. PL excitation was carried out using nitrogen laser radiation (wavelength $\lambda = 337$ nm, pulse duration $\tau_p = 8$ ns), the signal was detected in the photon counting regime. The PL spectra of films were measured during the excitation pulse action. The leading edges of the strobe (duration 250 ns) and the laser pulse were aligned, thus obtaining the PL spectrum at $t < 250$ ns; then the strobe was shifted relative to the laser pulse in order to measure times less than 50 ns. Subsequent PL spectra were measured with the strobe delay of 250 ns. When the *por*-Si PL spectra were measured, both the strobe duration and its delay time were increased.

Three types of *nc*-Si samples served as the objects of the study: samples of the first and second kinds, i.e., films fabricated by pulse laser *c*-Si evaporation in vacuum; and, for comparison, samples of the third type, i.e., conventional *por*-Si layers formed by stain chemical etching (type 3a) [11, 12] and by electrochemical (type 3b) etching of *c*-Si. Films of the first type were deposited from the forward beam of particles of the erosion jet onto a substrate remote from the target in the direction of the normal. Films of the second type were deposited from the reverse beam of particles onto a substrate located at the target plane [14]. Sputtering was carried out by radiation from a YAG:Nd^{3+}-laser working in the Q-switched mode with the wavelength $\lambda = 1.06$ μm, pulse energy 0.2 J, pulse duration $\tau_p = 10$ ns, and pulse repetition frequency 25 Hz. In the first case, *c*-Si was sputtered in an oxygen atmosphere; the pressure in the chamber was varied within the range 1.5×10^{-2}–20 Pa. In the second case, *c*-Si was sputtered in an inert gas atmosphere, helium or argon, at a pressure of about 65 and 6.5 Pa, respectively.

3. RESULTS OF TIME-RESOLVED PHOTOLUMINESCENCE MEASUREMENTS IN *nc*-Si

The analysis of the interrelation between characteristics of the time-resolved PL and sample structure features has shown that the PL properties of samples of the first and third type represent two limiting cases. The first of these is the property of structures with NC Si in the form of quantum dots (QD) in the SiO_x matrix ($x = 1$–2) with minimum porosity ($p \approx 1$–2%). The PL was characterized only by the fast component ($\tau < 50$ ns), and the emission spectrum was in the energy range $h\nu = 1.6$–3.2 eV. The PL intensity I_{PL} grew with a decrease in NC size *d*, and the emission peak shifted into the blue region of the spectrum [13]. The second limiting case consists of properties of *por*-Si (type 3b samples are most characteristic) and structures with the Si NC in the form of quantum wires in the matrix of a very porous SiO_x phase ($p \approx 70$–85%). Along with the fast component, a slow one with relaxation times up to a few milliseconds was present in the PL. The slow component was dominant, and its spectrum was shifted to lower energies (Fig. 1a). Properties of samples of the second type, which are Si NC QDs in a matrix of medium porosity, are intermediate between the above-mentioned limiting cases. Freshly fabricated samples of the second type were characterized by a PL that was more intensive than samples of the first type, but only the fast component was also present in this case. The PL spectrum shifted to the blue region with increasing NC size (Fig. 1b).

The slow PL component ($\tau > 250$ ns) appeared at $T \approx 150$ K, and its intensity increased with decreasing temperature (Fig. 1c). For samples of the second kind, as distinct from those of the first one, the slow PL component contribution increased, relaxation times reached the microsecond scale, and the spectrum shifted into the low-energy range upon oxidation (both in aging in open air and as a result of thermal treatment) (Fig. 1d). For all samples of the second kind, only the shape of the spectrum of the fast component changed with a temperature increase from 90 to 300 K, and its low-energy intensity increased with increasing temperature (Fig. 1e). The spectra of the fast PL component ($\tau < 250$ ns) are not simple: they can be decomposed into three Gaussian bands (central- and side-bands) (Fig. 1b). The low-energy band maximum spectral position hardly changes upon aging in air, but its intensity visibly changes. The central and high-energy peaks are shifted into the red range of the spectrum. The further increase of the observation time ($t > 250$ ns) leads to a dramatic decrease in the intensity of the high-energy band, the central peak is slightly shifted to lower energies, and the PL spectrum shape is described by the single Gaussian function (Figs. 1c, 1d).

A well-defined correlation between the PL intensity increase and the increase of its relaxation time under the action of various technological factors (temperature or thermal treatment time) was observed both for *por*-Si and for oxidized films of the second kind. The PL relaxation times increased with decreasing measurement temperature. The PL quantum yield for film structures reached a few percent at 300 K. The PL relaxation curves had the form of stretched exponentials similar to those characteristic of *por*-Si [2, 6, 12].

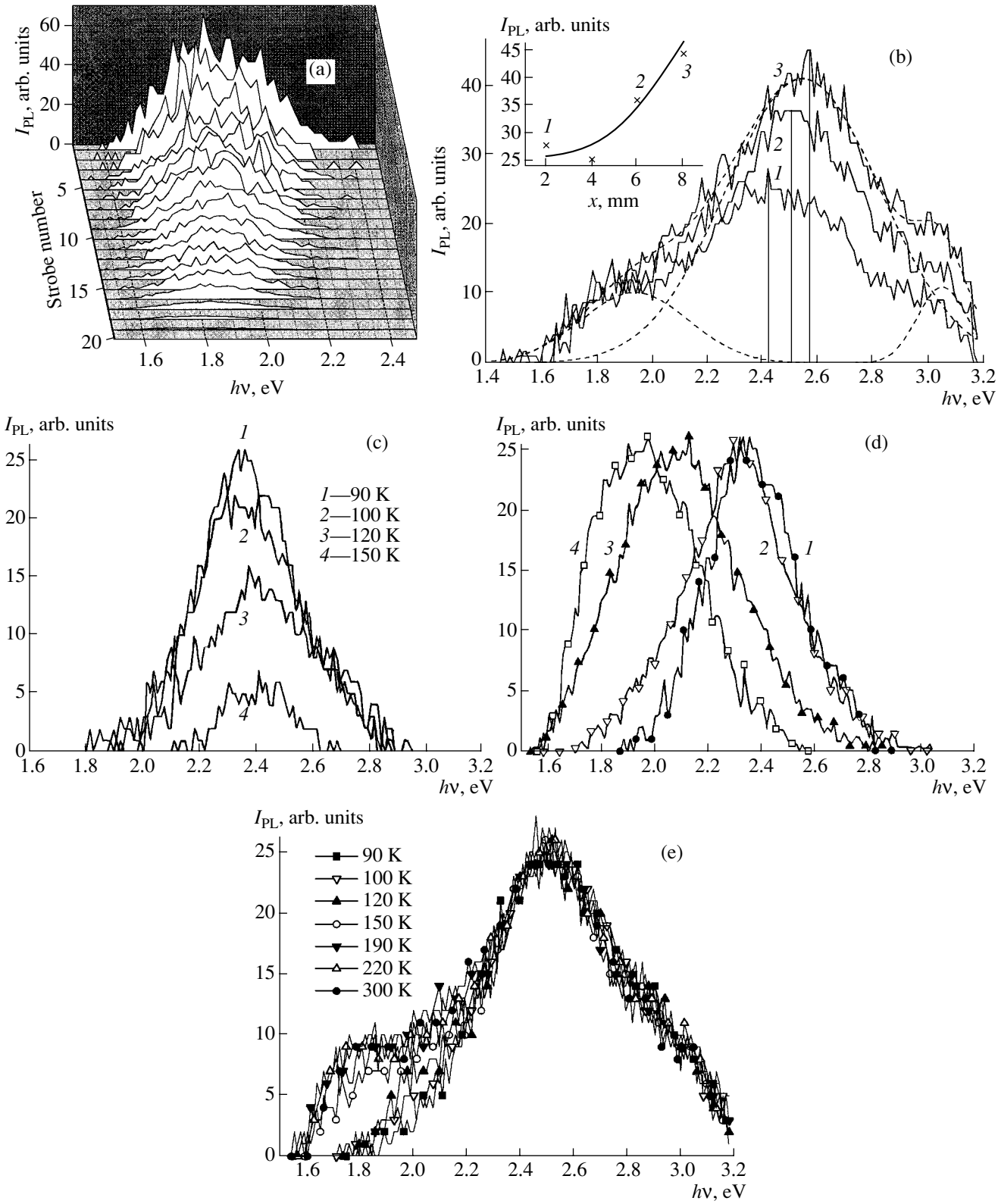

Fig. 1. Time-resolved PL spectra: (a) *por*-Si (maximum times, $\tau \approx 100$ μs); (b–e) samples of the second kind. (b) Freshly fabricated samples with NC size $d_1 > d_2 > d_3$ for *1–3* ($\tau < 50$ ns); a decomposition of curve *3* into three Gaussian functions is presented; inset: the PL intensity dependence on the distance x from the sputtering point. (c) Freshly fabricated sample, measured at 90–150 K ($\tau =$ 250–500 ns). (d) (*1*) Freshly fabricated sample, (*2*) sample aged in air, (*3*) that annealed at 900 K, and (*4*) that annealed at 1300 K; measurement temperature 90 K; PL is measured as an integral over slow components. (e) Freshly fabricated sample; measurement temperature 90–300 K ($\tau < 250$ ns).

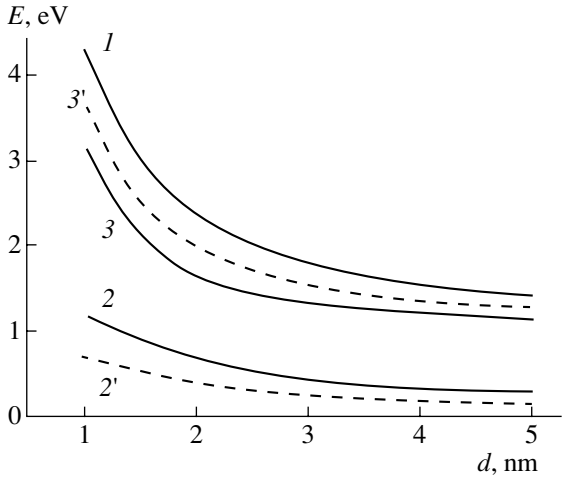

Fig. 2. (*1*) Broadened band gap E_g [18], (*2*, *2*') exciton binding energy E_x [17], and (*3*, *3*') exciton transition energy $E_{h\nu}$ for $\varepsilon_2 = 1$ (*2*, *3*) and $\varepsilon_2 = 2$ (*2*', *3*').

4. EXCITON MECHANISMS OF VISIBLE LUMINESCENCE

According to nonequilibrium thermodynamics, the following relation between the exciton n_x and electron–hole pair n densities and the exciton binding energy E_x is valid:

$$n_x = \frac{n^2}{n_0 \exp(-E_x/kT)}, \quad (1)$$

where n_0 is the statistical weight of the exciton state and kT is the thermal energy.

In the case of the uniform absorption of the interband monochromatic radiation, the continuity equation for the generation-recombination flows of electron–hole pairs and excitons reads as follows:

$$\frac{d(n+n_x)}{dt} = -\frac{n}{\tau_n} - \frac{n_x}{\tau_x} + \alpha I, \quad (2)$$

where

$$\tau_n = \left(\frac{1}{\tau_n^r} + \frac{1}{\tau_n^n}\right)^{-1}, \quad (3)$$

$$\tau_x = \left(\frac{1}{\tau_x^r} + \frac{1}{\tau_x^n}\right)^{-1}. \quad (4)$$

The following notation is assumed here: τ_n and τ_x, τ_n^r and τ_x^r, τ_n^n and τ_x^n are, respectively, total, radiative, and nonradiative lifetimes of electron–hole pairs and excitons; α is the effective absorption coefficient of the exciting light with account of multiple reflections in *nc*-Si; and I is the intensity of light.

In the case under consideration, the light-generated electron–hole pairs form excitons due to the Coulomb attraction; therefore, two kinetically coupled subsystems coexist during the recombination process. The so-called high excitation level case [15] is of particular interest, i.e., when $n_x > n$ and the relaxation of excitation proceeds mainly via the exciton subsystem. As is seen from (1) and (2), this case is more likely the lower the temperature and the higher E_x. This is possible only at very low temperature in the bulk silicon because of E_x smallness. Relation (1) must be satisfied not only for free, but also for bound and autolocalized excitons, for which the binding energy is usually very large (see, e.g., [7]). The condition for a high excitation level in Si NC is satisfied even at room temperature if E_x is large enough.

The quantity E_x depends on the size d and the shape of NC and on the dielectric properties of the matrix in nanostructures. The following data on this dependence are reported in the literature. It is established in [16] that the static dielectric constant of the silicon nanoparticles abruptly falls from 11.7 to 4 as the size decreases from 6–2 nm to 1 nm. The Coulomb interaction in quantum semiconductor wires is considered in [5] within the constant effective mass approximation, and an expression for $E_x(d, \varepsilon_1, \varepsilon_2)$ is derived, which takes into account the dielectric constants of NC and its environment. The exciton binding energy was calculated [4, 17] for quantum wires in environments with different dielectric constants. The calculation in [4] was carried out using the variational method, whereas the authors of [17] used the wave function expanded in a system of linearly independent functions describing the longitudinal (along the wire) and transverse motion of the interacting electrons and holes. The cluster-size dependence of the electronic spectrum of the Si cluster with one Si=O bond is calculated in [7]. Results of the calculation of $E_x(d)$ function for $\varepsilon_2 = 1$ and $\varepsilon_2 = 2$ from [17] are presented in Fig. 2 (curves *2* and *2*'). First of all, it follows from Fig. 2 that exciton binding energy in quantum wires can reach 1.0 eV at $\varepsilon_2 = 1$, which, in its turn, indicates the essential role played by the exciton recombination in *nc*-Si. In order to show how essential the effect of the exciton binding energy on the long-wavelength shift of the PL spectral peak is in comparison with the absorbed energy, Fig. 2 presents energies of related radiative exciton transitions $E_{h\nu}$ (curves *3*, *3*'). They are obtained by taking into account the broadened band gap E_g calculated within the cluster approximation in [18]. It is noteworthy that the exciton binding energy in QDs is larger than in quantum wires, and, therefore, the exciton transition energy will be smaller and its NC size dependence will be flatter, like the one given in [7].

Let us now discuss mechanisms of radiative and nonradiative recombination in Si NC. Since silicon is an indirect gap semiconductor, the probabilities of band-to-band and exciton radiative recombination essentially increase with decreasing Si NC size [19] because of the partial violation of the momentum conservation law. The values τ_n^r and τ_x^r become smaller

than 1 μs at about 3 nm (for a transition from the singlet level). However, the exciton radiative recombination time is much longer for the transition from the triplet state since this transition is forbidden to a first approximation [2]. Thus, it is necessary to explain also the increase in the nonradiative-recombination time in order to understand the nature of the PL intensive red band with the quantum yield of about 1–10%.

As for the "bulk" and "surface" mechanisms of the nonradiative multiphonon recombination, they cannot be unique. The volume of a nanoparticle with a mean diameter of 3 nm is about 10^{-20} cm^3, and the surface area is about 10^{-13} cm^2. Therefore, deep local centers participating in the multiphonon recombination are, as a rule, in no way present in all nanoparticles. The exception is provided by quantum wires with a large number of dangling bonds on the surface, but the passivation of these bonds reduces the surface nonradiative recombination rate practically to zero. This occurs when the concentration of dangling bonds is less than $1/\pi hd$, where h is the wire length and d is its diameter. That is why the Auger recombination becomes the main mechanism of nonradiative recombination in silicon nanoparticles. Nevertheless, the influence of even a small concentration of surface states can be significant because of the large internal surface of *nc*-Si.

Let us assume that the excitation level is high and the PL in the nanostructures occurs by the exciton mechanism. Then, according to (2), the steady state exciton density is $n_x = \alpha I \tau_x$. We will first consider the case when the Auger recombination is due to the interaction of the exciton and a free electron (or hole), i.e., $\tau_x^{-1} = An$, where A is a constant. Taking (1) into account with the PL quantum yield essentially less than unity, we then obtain

$$\tau_x \sim \frac{\exp(E_x/3kT)}{I^{1/3}}. \tag{5}$$

Since $E_x/kT \gg 1$ in Si nanoparticles of the above-mentioned size, their Auger recombination time must be much longer than that in bulk crystals. This implies that the PL quantum yield in nanosize silicon structures must be essentially higher than in the bulk silicon. In addition, E_x and, therefore, τ_x depend not only on the nanoparticle size, but also on the dielectric properties of the environment; this explains the influence of porosity (due to the decrease of ε_2) on the τ_x magnitude.

The PL decay kinetics is determined in the present case by the $n_x(t)$ dependence, which reads

$$n_x(t) = \frac{\exp(E_x/kT)}{[At/2 + n(0)^{-1}]^2 n_0}, \tag{6}$$

where

$$n(0) = \left[\frac{\alpha I n_0 \exp(-E_x/kT)}{A}\right]^{1/3}$$

is the electron–hole pair density at the instant of time when illumination is switched off. As is seen from (6), the relaxation law is essentially nonexponential, and the instantaneous recombination time increases rapidly during the PL relaxation.

The dependence of the PL quantum yield η on illumination intensity is given in this case by

$$\eta \propto \frac{I^{2/3}}{I} = I^{-1/3} \tag{7}$$

and coincides with the corresponding dependence in the case when the nonradiative recombination is governed by the interband Auger recombination. The difference between the above mechanisms consists in dissimilar dependence of the relaxation times on excitation intensity. For example, in the case of the exciton Auger recombination, the relaxation time is proportional to $I^{-1/3}$, while in the case of the interband Auger recombination, it is proportional to $I^{-2/3}$.

Let us now consider the case when the exciton Auger recombination occurs as a result of the inelastic interaction of two excitons. In this case, $\tau_x^{-1} = Bn_x$, where B is a constant, and the relaxation law at high excitation levels has the following hyperbolic character:

$$n_x(t) = [Bt + n_x^{-1}(0)]^{-1}, \tag{8}$$

where $n_x(0) = (\alpha I/B)^{1/2}$ is the exciton density at the instant when the illumination is turned off.

In this case, the dependence of the η value on illumination intensity is determined by the relation

$$\eta \propto \frac{I^{1/2}}{I} = I^{-1/2}. \tag{9}$$

The various relaxation functions derived above and the intensity dependence of the PL at different nonradiative exciton recombination mechanisms can be used for the analysis of the experimental dependences of the PL in *nc*-Si.

5. DISCUSSION OF EXPERIMENTAL RESULTS. MECHANISMS OF VISIBLE LUMINESCENCE IN FILMS UNDER STUDY

The increase observed on the freshly fabricated films of the PL intensity and the spectrum peak shift with the decrease of the NC size indicate a manifestation of size quantization in NC. The complexity of the PL spectra, the presence of bands with different kinetics, and the large width of the bands (Fig. 1b, 1c) indicate not only the scatter of the NC sizes, but also the occurrence of several recombination mechanisms.

It is known from the literature (see, e.g., [2, 4, 6, 20]) that radiative recombination in the oxidized *nc*-Si proceeds via various channels including, along with the singlet and triplet exciton transitions, transitions between quantum levels in NC with the participation of

electron–hole pairs, with the PL relaxation times decreasing with increasing emission energy. These are as long as a few milliseconds for the triplet red band, from a few hundred picoseconds up to a few hundred nanoseconds for the blue band, and up to a few hundred microseconds for the red band in the case of band-to-band recombination. Another channel of recombination is related to defects of the oxide layer [9, 10, 20]. For example, its blue band, with a peak at $h\nu = 2.7$ eV, has characteristic times of about a few nanoseconds [20]; the characteristic times for the other bands are in the range from a few nanoseconds to a few microseconds [10].

The "fastest" spectra observed by us during the action of the laser pulse, i.e., the ones characterized by times of about a few tens of nanoseconds, lie in a very wide range of energies $h\nu = 1.4$–3.2 eV and comprise three bands (Fig. 1e). The "slowest" spectra with characteristic times approaching a few microseconds could be described by one Gaussian function at the energy range $h\nu = 1.4$ (1.6)–2.8 eV (Fig. 1d). It is reasonable to assume that the fast blue band is due not only to the band-to-band recombination in the smallest NC, but, possibly, also to the recombination on local levels related to defects in SiO_2. The band in the energy range $h\nu = 1.4$ (1.6)–2.8 eV is determined by kinetically coupled subsystems of electron–hole pairs and excitons. The increase of the fast PL component intensity at the low-energy range with the temperature increasing from 90 to 300 K (Fig. 1e) is traced back to the contribution of the phonon-assisted radiative transitions.

Since the quantum yield of all studied samples does not exceed a few percent, and we observed a correlated change of the PL intensity and of its relaxation time at $T > 150$ K, the measured PL time is governed by the nonradiative recombination at the studied temperature range.

The presence of only the fast PL component with small intensity in freshly grown films can be explained by the prevalence of the fast surface nonradiative recombination channel. In reality, the NC/SiO_x interface is characterized in these films by a high nonuniformity of the oxygen deposition and, unlike the perfect *c*-Si/SiO_2 interface, contains a large amount of surface defects. According to the experiment, the absence of pores in the films of the first type, as distinct from those of the second type, gives no way of changing the recombination properties of the NC/SiO_x interface by means of oxidation.

A different situation takes place for the porous films of the second type. First of all, the exciton binding energy increases due to oxidation since the dielectric constant of SiO_2 is less than the one for *c*-Si. Therefore, the exciton radiative recombination probability increases. The exciton transition energy decreases (the red shift of the spectrum). The enhanced diffusion of oxygen through pores favors the passivation of the dangling bonds of Si atoms and a decrease in the number of surface nonradiative levels. The number of these states is greater in larger NC, compared with smaller ones, and, therefore, the suppression of the surface nonradiative channel manifests itself more effectively in their PL and, thus, in a longer wavelength range of the PL spectrum. This is an additional factor leading to the red shift of the PL spectra due to oxidation (Fig. 1d) and to the essential PL intensity increase. It is noteworthy that the radiation energy observed for the long-wavelength bands fall within the range of calculated energies for exciton transitions (Fig. 2). The experimental results on the increase of the PL relaxation times are a convincing manifestation of exciton recombination.

The nonradiative recombination mechanism related to the drain of carriers from NC in tunneling through potential barriers [21] is hindered upon oxidation, when the oxide layer thickness increases. The size scatter and the barrier height determine the piecewise-exponential shape of the PL relaxation function. This nonradiative-recombination mechanism also accounts for the observed relaxation times reaching a few milliseconds in *por*-Si, but it is inconsistent with observed temperature dependence of relaxation times. Similarly large times of nonradiative recombination and the nonexponential character of the PL relaxation are characteristic for the exciton Auger recombination considered above. In this case, the nonradiative recombination is determined by the exciton energy transfer to a free electron (hole). The experimentally observed dependences of τ_x and E_x on the NC size and shape and on the dielectric environment point to this mechanism of exciton Auger recombination.

The mainly excitonic nature of the visible PL in the porous *nc*-Si films under study is indicated by the possibility of a consistent explanation, in terms of this mechanism, of the whole set of observed features of radiative and nonradiative recombination and their dependence on fabrication and measurement conditions.

6. CONCLUSION

Thus, the results of the study of films fabricated by laser-induced evaporation are explained within the framework of the model that assumes quantum confinement in Si NC. It is proposed that both the absorption of photons and the emission responsible for the visible PL occur in NC. Both excitons and electron–hole pairs participate in recombination upon excitation of electron–hole pairs by photons with an energy corresponding to band-to-band absorption in Si NC. The porosity of the films ensures the dielectric enhancement effect and determines large exciton binding energies, which, in turn, leads to the dominant role of the PL exciton mechanism. The high efficiency of the visible PL is due to the suppression of the surface nonradiative recombination channel and to the large times of exciton Auger recombination.

REFERENCES

1. L. T. Canham, Appl. Phys. Lett. **57** (10), 1046 (1990).
2. A. G. Cullis, L. T. Canham, and P. D. J. Calcott, J. Appl. Phys. **82** (3), 909 (1997).
3. P. K. Kashkarov, B. I. Kamenev, E. A. Konstantinova, *et al.*, Usp. Fiz. Nauk **168** (5), 577 (1998) [Phys. Usp. **41**, 511 (1998)].
4. M. G. Lisachenko, E. A. Konstantinova, P. K. Kashkarov, and V. Yu. Timoshenko, Phys. Status Solidi A **182**, 297 (2000).
5. V. S. Babichenko, L. V. Keldysh, and A. P. Silin, Fiz. Tverd. Tela (Leningrad) **22** (4), 1238 (1980) [Sov. Phys. Solid State **22**, 723 (1980)].
6. Y. Kanemitsu, Phys. Rep. **263**, 1 (1995).
7. M. V. Wolkin, J. Jorne, P. M. Fauchet, *et al.*, Phys. Rev. Lett. **82** (1), 197 (1999).
8. Fang-shi Xue, Xi-mao Bao, and Feng Yan, J. Appl. Phys. **81** (7), 3175 (1997).
9. A. J. Kontkiewicz, A. M. Kontkiewicz, J. Svejka, *et al.*, Appl. Phys. Lett. **65** (11), 1436 (1994).
10. X. Zhao, O. Schoenfeld, S. Nomura, *et al.*, Mater. Sci. Eng. B **35**, 467 (1995).
11. S. V. Svechnikov, L. L. Fedorenko, and E. B. Kaganovich, Ukr. Fiz. Zh. **39** (6), 704 (1994).
12. L. L. Fedorenko, A. D. Sardarly, E. B. Kaganovich, *et al.*, Fiz. Tekh. Poluprovodn. (St. Petersburg) **31** (1), 6 (1997) [Semiconductors **31**, 4 (1997)].
13. E. G. Manoilov, A. A. Kudryavtsev, S. V. Svechnikov, *et al.*, Thin Solid Films **349**, 298 (1999).
14. L. Patrone, D. Nelson, V. I. Safarov, *et al.*, J. Appl. Phys. **87** (8), 3829 (2000).
15. A. V. Sachenko, V. A. Tyagay, and A. G. Kundzich, Phys. Status Solidi B **88**, 797 (1978).
16. R. Tsu, D. Babic, and L. Ioriatti, Jr., J. Appl. Phys. **82** (3), 1327 (1997).
17. Yu. V. Kryuchenko and A. V. Sachenko, in *Proceedings of the 2nd Russia–Ukraine Workshop "Nanophysics and Nanoelectronics", Kiev, 2000*, p. 96.
18. J. F. Proot, G. Delerue, and G. Alan, Appl. Phys. Lett. **61** (16), 1948 (1992).
19. M. S. Bresler and I. N. Yassievich, Fiz. Tekh. Poluprovodn. (St. Petersburg) **27** (5), 873 (1993) [Semiconductors **27**, 475 (1993)].
20. G. G. Qin and G. Qin, Phys. Status Solidi A **182**, 335 (2000).
21. J. C. Vial, S. Billat, A. Bsiery, *et al.*, Physica B (Amsterdam) **185**, 593 (1993).

Translated by S. Ktitorov

Semiconductors, Vol. 35, No. 12, 2001, pp. 1390–1397. Translated from Fizika i Tekhnika Poluprovodnikov, Vol. 35, No. 12, 2001, pp. 1452–1459.

LOW-DIMENSIONAL SYSTEMS

Renormalization of Energy Spectrum of Quantum Dots under Vibrational Resonance Conditions

A. V. Fedorov*, ^, A. V. Baranov*, A. Itoh, and Y. Masumoto****

** Vavilov State Optical Institute, St. Petersburg, 199034 Russia*

^ e-mail: anatoli.fedorov@online.ru

*** Institute of Physics, University of Tsukuba, Tsukuba 305-8571, Japan*

Abstract—The problem of modification of the energy spectrum of electronic and phonon excitations in semiconductor quantum dots (QDs) under conditions of vibrational resonance is considered. Analytical expressions for the energy of polaron-like states in QDs in the form of a sphere or rectangular parallelepiped, taking into account the size dependence of the electron–phonon interaction, are derived. Experimental data on renormalization of the lowest exciton states in QDs based on CuCl in a NaCl matrix have been obtained with the use of two-photon secondary emission resonance spectroscopy. Comparison with the calculated results demonstrates quantitative agreement indicating the adequacy of the employed theoretical model. It is established that the vibrational resonance strongly modifies the energy spectrum of small QDs. *© 2001 MAIK "Nauka/Interperiodica".*

1. INTRODUCTION

The effects of renormalization of the energy spectrum of electron and phonon excitations due to the electron–phonon interaction in bulk semiconductors are well known. The corresponding theoretical models using "hybrid electron–phonon" or "polaron-like" states as eigenfunctions of the system are also widely known [1]; they predict an appreciable modification of spectra under vibrational resonance (VR) conditions, i.e., at an optical phonon energy equal to the energy gap between the electronic states. However, the direct experimental observation of the predicted renormalization effects is practically absent. This is quite natural, since such resonance can be observed in bulk materials only in exceptional cases, e.g., in the presence of a strong magnetic field [1]. The discrete energy spectrum of semiconductor nanocrystals or quantum dots (QDs) [2] makes them unique objects for studying the VR, especially in a system with a broad size distribution of QDs. In this case, as a result of the size dependence of the electronic state energy, a pair of levels can always be found for which the VR condition is satisfied. By varying the phonon energy, one can successively excite QDs so that the energy gap between this pair of levels changes continuously in the VR range. This feature of the QD ensemble was noticed in [3, 4], where a Fröhlich-type interaction in spherical QDs was studied both experimentally and theoretically. A modification of the spectra can be experimentally observed in the resonance optical excitation of the renormalized states, i.e., under double resonance conditions. In this case, the same excited state of a QD is coupled to the ground state via electron–photon interaction and to another excited state via electron–phonon interaction.

The resonance fluorescence and luminescence, for which the spectral position of bands is determined by the QD electronic spectrum, are of particular interest for observing the VR. For the secondary emission to be reliably detected, optical transitions into absorbing and emitting states must be resolved in the dipole approximation and the homogeneous broadening of the resonance levels must not be too large. The latter assumes that low-temperature experiments are to be carried out when only the higher level in a pair of electron levels resonantly coupled via the electron–phonon interaction is essentially modified. It is this state that must be excited as a result of the interband optical transition. The main part of the secondary emission is induced by interband transitions from a lower QD excited state as a result of the fast interband relaxation. Thus, the VR will reveal itself most distinctly in luminescence spectra formed by the two lowest size-quantization levels for which the homogeneous optical transition line width is the narrowest. Since these states have opposite "parities," two-photon excitation should be used because all optical transitions are dipole-allowed in this case [5].

One of the first attempts to observe the modification of the exciton and phonon spectra in QDs was made when one-photon-excited luminescence was studied in spherical CuCl QDs grown in a glass matrix [3]. However, the experimental data gave no way of making reliable estimates because of low spectral resolution. The statement concerning the presence of hybrid exciton–phonon states [3] was based, first of all, on an increase of the luminescence intensity in the VR range. In describing the effect, the authors of [3] restricted themselves to a general definition of the problem. Degeneracy lifting in the system "exciton + phonon" for a pair of the lowest CuCl QD exciton states in the NaCl

1063-7826/01/3512-1390$21.00

matrix was observed in the two-photon-excited luminescence spectra [6]. However, the authors of [6] failed to provide a satisfactory explanation of the observed features and the problem remained unsolved. Numerical calculation of the energy renormalization of a totally symmetric optical phonon, induced by VR between exciton states of the same parities, was carried out in [7] for spherical CuCl QDs. The results were used to account for the longitudinal optical phonon (*LO*) energy decrease observed in one-photon-excitation luminescence spectra and in persistent hole-burning spectra. However, rather arbitrary simplifying assumptions of an unclear physical nature were made in these calculations.

In this study, the problem of the QD energy spectrum modification under the VR conditions is solved by the method of direct diagonalization of the electron–phonon (exciton–phonon) Hamiltonian. Analytical expressions for energies of the polaron-like states in QDs, in the forms of a rectangular parallelepiped and a sphere with sizes both larger and smaller than the Bohr radius of the exciton in a bulk material, were obtained using this approach. In solving this problem, matrix elements of the *LO* phonon interaction with electrons and excitons in rectangular QDs were calculated for the first time. The theoretical calculations are compared with the experimental data on the modification of the energy spectrum of the rectangular CuCl QDs in the NaCl matrix under conditions of VR between the lowest exciton states, obtained from spectra of the two-photon-excited (TPE) luminescence and resonance fluorescence at 2 K. The model proposed by us is shown to describe quantitatively the VR-induced renormalization of the exciton and phonon energy spectra in QDs.

2. VIBRATIONAL RESONANCE IN QUANTUM DOTS

For describing VR, let us use the electron–phonon Hamiltonian in the secondary quantization representation

$$H = H_e + H_{ph} + H_{e,ph}, \tag{1}$$

where

$$H_e = \sum_n E_n a_n^+ a_n, \quad H_{ph} = \sum_p \hbar\Omega_p (b_p^+ b_p + 1/2) \tag{2}$$

are the Hamiltonians of noninteracting electrons (excitons) and phonons, and

$$H_{e,ph} = \sum_{n_1, n_2, p} (V^{(p)}_{n_1, n_2} b_p + V^{(p)*}_{n_2, n_1} b_p^+) a^+_{n_1} a_{n_2} \tag{3}$$

is the operator of interaction between them. In Eqs. (2) and (3), a_n^+ and a_n are electron (exciton) creation and annihilation operators for the state with energy E_n; b_p^+ and b_p are creation and annihilation operators for phonons with the energy $\hbar\Omega_p$, belonging to the *p*-mode. Under the VR conditions (e.g., at $E_{n_2} - E_{n_1} \approx \hbar\Omega_p$), mixing of electron (exciton) and phonon states occurs and the related wave functions cannot be represented in the form of a simple product of electronic and vibrational states. In this case, polaron-like states appear in QDs, which are eigenfunctions of the total Hamiltonian (1) of the system "electrons + phonons." Diagonalization of the Hamiltonian (1) cannot be carried out exactly in the general case; therefore, we shall use simplifying assumptions, which have a clear physical nature. First of all, we take into account only *LO* phonons coupled with the electronic subsystem via the Fröhlich interaction, since it is the most effective in semiconductor compounds (I–VII, II–VI, and III–V) used for fabrication of QDs which are now being studied extensively. We further use the zero-temperature approximation and assume that the interaction satisfies the inequality $V^{(p)}_{n_1, n_2}/\hbar\Omega_p < 1$; i.e., it is not too strong. This allows us to restrict ourselves to the zero- and single-phonon basis of the unperturbed Hamiltonian $H_e + H_{ph}$:

$$|n; 0\rangle = |E_n\rangle|0\rangle_{ph}, \quad |n; p\rangle = |E_n\rangle|\hbar\Omega_p\rangle, \tag{4}$$

where

$$|E_n\rangle = a_n^+|0\rangle_e, \quad |\hbar\Omega_p\rangle = b_p^+|0\rangle_{ph}, \tag{5}$$

and $|0\rangle_{ph}$ and $|0\rangle_e$ are vacuum states of the vibrational and electronic subsystems.

If the electron (exciton) energy level difference $E_2 - E_1$ is near the longitudinal optical phonon energy $\hbar\Omega_{LO}$, then zero-approximation states can be taken in the expansion of the total Hamiltonian wave functions, except for those with an energy not differing too greatly from E_2. Wave functions of the latter are linear combinations of the almost degenerate states

$$|\mathscr{E}_k\rangle = c_1^{(k)}|2; 0\rangle + c_2^{(k)}|1; 1\rangle + \ldots + c_{p+1}^{(k)}|1; p\rangle, \quad k = 1, 2, \ldots, p+1. \tag{6}$$

Using basis (6), a set of linear homogeneous equations for coefficients $c_l^{(m)}$ can be easily obtained; i.e., we have a standard eigenvalue problem that can be analytically solved only for $k \le 4$. However, as will be illustrated by concrete examples below, of particular interest is the case of interaction with a single vibrational mode ($k = 2$), for which

$$\mathscr{E}_{1,2} = \frac{1}{2}(E_2 + E_1 + \hbar\Omega_1 \pm \delta),$$
$$|\mathscr{E}_{1,2}\rangle = c_{1,2}|2; 0\rangle \pm c_{2,1}|1; 1\rangle, \tag{7}$$

where

$$c_1 = (E_2 - E_1 - \hbar\Omega_1 + \delta)/\Delta, \quad c_2 = 2V_{2,1}^{(1)}/\Delta, \quad (8)$$

$$\Delta = [(E_2 - E_1 - \hbar\Omega_1 + \delta)^2 + 4|V_{2,1}^{(1)}|^2]^{1/2},$$
$$\delta = [(E_2 - E_1 - \hbar\Omega_1)^2 + 4|V_{2,1}^{(1)}|^2]^{1/2}. \quad (9)$$

It follows from (7) that at the exact resonance $E_2 - E_1 = \hbar\Omega_1$ the degeneracy of $|2; 0\rangle$ and $|1; 1\rangle$ states is totally lifted by the electron–phonon interaction so that the energy level splitting equals $2|V_{2,1}^{(1)}|$. The lower-energy state E_1 remains unchanged despite resonant coupling to E_2.

For simplicity, we take into account only one conduction (c) band and one valence (h) band for description of the semiconductor material and assume the depth of the potential well for electrons and holes to be infinite. Let us consider a QD in the form of a sphere with radius R and a rectangular parallelepiped with the edge lengths $L_i (i = x, y, z)$. In the case when the Bohr radius R_{ex} of the bulk exciton is larger than the QD characteristic size $\tilde{R} = \{R \text{ or } \max(L_i/2)\}$, i.e., in the "strong confinement mode," the size-quantization energy levels and the envelopes of electron and hole wave functions are given by

$$E_{nlm}^c = \frac{\hbar^2 k_{nl}^2}{2m_c}, \quad E_{nlm}^h = E_g + \frac{\hbar^2 k_{nl}^2}{2m_h}, \quad (10)$$

$$\psi_{nlm}^{c(h)}(x) = \sqrt{\frac{2}{R^3}} \frac{j_l(k_{nl}x)}{j_{l+1}(\xi_{nl})} Y_{lm}(\theta, \varphi), \quad (11)$$

$$E_{\mathbf{n}}^c = \frac{\hbar^2 k_{\mathbf{n}}^2}{2m_c}, \quad E_{\mathbf{n}}^h = E_g + \frac{\hbar^2 k_{\mathbf{n}}^2}{2m_h}, \quad (12)$$

$$\psi_{\mathbf{n}}^{c(h)}(x) = \sqrt{\frac{8}{L_x L_y L_z}} \sin k_{n_x} x \sin k_{n_y} y \sin k_{n_z} z, \quad (13)$$

where m_c and m_h are, respectively, electron and hole effective masses; E_g is the band gap; ξ_{nl} is the nth root of the equation $j_l(x) = 0$; $j_l(x)$ and $Y_{lm}(\theta, \varphi)$ are, respectively, the spherical Bessel function and the spherical harmonic; l and m are the angular momentum and its component; $k_{nl} = \xi_{nl}/R$; $\mathbf{n} = (n_x, n_y, n_z)$; $k_{n_i} = \pi n_i/L_i$; and $\mathbf{k}_\mathbf{n} = (k_{n_x}, k_{n_y}, k_{n_z})$ is the vector with length $k_\mathbf{n} = \pi(n_x^2/L_x^2 + n_y^2/L_y^2 + n_z^2/L_z^2)^{1/2}$. Applying the method developed in [8], matrix elements of the Fröhlich interaction (3) of electrons and holes with *LO* phonons in a spherical or rectangular QD can be easily calculated; i.e.,

$$V_{n_2 l_2 m_2;\, n_1 l_1 m_1}^{(nlm)} = -e f_{nl} \sqrt{\frac{(2l_1+1)(2l+1)}{4\pi(2l_2+1)}} \times I_{n_2 l_2;\, n_1 l_1}^{nl;\, l} C_{l0;\, l_1 0}^{l_2 0} C_{lm;\, l_1 m_1}^{l_2 m_2}, \quad (14)$$

$$f_{nl} = \frac{1}{\xi_{nl} j_{l+1}(\xi_{nl})} \left[\frac{4\pi\hbar\Omega_{LO}}{R}\left(\frac{1}{\varepsilon_\infty} - \frac{1}{\varepsilon_0}\right)\right]^{1/2}, \quad (15)$$

$$I_{n_2 l_2;\, n_1 l_1}^{nl;\, p} = \frac{2}{j_{l_2+1}(\xi_{n_2 l_2}) j_{l_1+1}(\xi_{n_1 l_1})} \times \int_0^1 dx x^2 j_{l_2}(\xi_{n_2 l_2} x) j_{l_1}(\xi_{n_1 l_1} x) j_p(\xi_{nl} x), \quad (16)$$

$$V_{\mathbf{n}_2;\, \mathbf{n}_1}^{(n)} = e f_\mathbf{n} G_x G_y G_z, \quad (17)$$

$$f_\mathbf{n} = \left[\frac{16\pi\hbar\Omega_{LO}}{L_x L_y L_z k_\mathbf{n}^2}\left(\frac{1}{\varepsilon_\infty} - \frac{1}{\varepsilon_0}\right)\right]^{1/2}, \quad (18)$$

$$G_i = \frac{4}{\pi} \frac{n_{2i} n_{1i} n_i [1 - (-1)^{n_{2i} + n_{1i} + n_i}]}{(n_{2i}^2 + n_{1i}^2 - n_i^2)^2 - 4n_{2i}^2 n_{1i}^2}, \quad i = x, y, z, \quad (19)$$

where $C_{lm;\, l_1 m_1}^{l_2 m_2}$ are the Clebsch–Gordon coefficients; ε_∞ and ε_0 are, respectively, the high- and low-frequency dielectric constants of the semiconductor; $\hbar\Omega_{LO}$ is the energy of the limiting *LO* phonon; and quantum numbers with indices 1 and 2 stand for the electron (hole) states, whereas quantities without indices are related to the phonon mode. Expressions (14)–(19) indicate that the size dependence of the Fröhlich electron–phonon interaction in scaling transformations is given by the expression $\propto \tilde{R}^{-1/2}$.

The selection rules contained in the above matrix elements restrict the number of phonon modes binding the pair of electronic states. However, the number of the remaining modes is too large for obtaining an analytical solution to the eigenvalue problem for polaron-like states that appear under VR conditions. For example, for spherical QDs, the selection rules are determined by the rules of the vector addition of angular momenta and are contained in the combination of the Clebsch–Gordon coefficients (14). At the same time, any restriction on the optical-phonon principal quantum number n stemming from the problem symmetry is absent. For rectangular QDs, the selection rules are determined by the functions G_i (19) and reduce to the requirement that the sum of quantum numbers $n_{2i} + n_{1i} + n_i$ ($i = x, y, z$) should be odd. Calculation of the electron–phonon interaction matrix elements with the use of (14)–(19) shows that, in the most interesting case for the description of the experimental data of VR between lowest electron (exciton) states, the coupling of one phonon

mode to these states is an order of magnitude stronger than that for other modes. The physical nature of this restriction can be easily understood with the example of rectangular QDs if the nature of the G_i functions is considered. These result from integration of the related spatial parts of the electron and phonon wave functions along the QD edge. For sufficiently large lengths, such integrals can be approximated by Kronecker deltas or even by Dirac delta functions expressing mathematically the wave vector conservation law. Thus, G_i functions are discrete analogues of the Kronecker delta and have a sharp peak at some values of the phonon quantum numbers n_i. In particular, G_i functions are maximum for the phonon mode $\mathbf{n} = (2, 1, 1)$ connecting the two lowest electronic states $\mathbf{n}_1 = (1, 1, 1)$ and $\mathbf{n}_2 = (2, 1, 1)$; they asymptotically fall as n_i^{-3} with increasing n_i. A similar analysis can also be carried out for spherical QDs. It is this feature that allows us to restrict ourselves to the single-mode approximation for the electron–phonon interaction in describing the VR.

The strong confinement in QDs occurs in semiconductors with a large exciton Bohr radius R_{ex}. These conditions are satisfied, e.g., for III–V compounds, in which $R_{ex} \approx 10$ nm. However, VR is only possible in the valence band since the effective electron mass is very small in these materials. Estimates show that this is also true for QDs based on II–VI semiconductor compounds (CdSe, CdS, etc.). Results of the calculation of the energy $\mathscr{E}_{1,2}$ in accordance with (7), for the case when the VR with *LO*-phonon occurs for a pair of the lowest hole states, are presented in Fig. 1 in order to illustrate the size-dependence of the energy spectrum renormalization in spherical and cubic QDs. The related matrix element of the electron–phonon interaction is given in the insert as a function of the characteristic size of a QD. The following values of InP parameters [9] were used in the calculations: $\varepsilon_0 = 12.61$, $\varepsilon_\infty = 9.61$, $\hbar\Omega_{LO} = 43.3$ meV, $m_c = 0.079m_0$, $m_h = 0.65m_0$ and $R_{ex} = 10.3$ nm, where m_0 is the free electron mass. Energies $E_1 + \hbar\Omega_1$ and E_2 crossing for a QD with a size corresponding to the exact VR are shown also in Fig. 1. At the same time, the renormalized energies $\mathscr{E}_1$ and $\mathscr{E}_2$ do not cross. Such behavior of the energy spectra is named anticrossing.

Under the weak-confinement conditions ($R_{ex} < \tilde{R}$), the QD optical spectra near the fundamental edge are determined by the Wannier exciton states, which are to be classified using six, instead of three, quantum numbers for the electron (hole) states. Three quantum numbers are related to the translation motion of the exciton as a whole, and three numbers describe the relative motion of the electron and hole in the exciton. The following expressions for the size-quantization energy levels and the envelopes of exciton wave functions in spherical and rectangular QDs are usually applied for

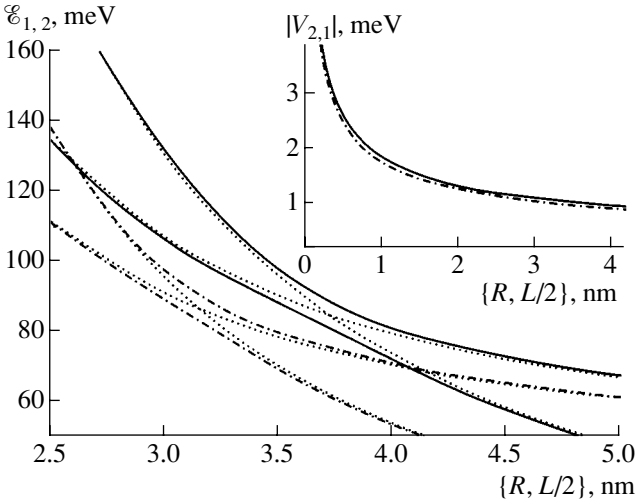

Fig. 1. InP QDs in the strong confinement mode: dependence of the polaron-like state energy $\mathscr{E}_{1,2}$ on QD size (R, L) for the VR of a pair of lowest hole states with the *LO* phonon. Solid and dash-dot lines refer, respectively, to spherical QDs of radius R and cubic QDs with edge L. Dotted lines show the size dependence of the $|2; 0\rangle$ and $|1; 1\rangle$ states. *Insert*: matrix element of electron–phonon interaction as a function of the characteristic linear size of QD.

analytical calculations in the case of weak confinement [4]:

$$E_{nlm;\, n'l'm'} = E_g - \frac{Ry}{n'^2} + \frac{\hbar^2 k_{nl}^2}{2M},$$
$$\varphi_{nlm;\, n'l'm'}(x, X) = \psi_{nlm}(x)\Psi_{n'l'm'}(X), \tag{20}$$

$$E_{\mathbf{n};\, n'l'm'} = E_g - \frac{Ry}{n'^2} + \frac{\hbar^2 k_{\mathbf{n}}^2}{2M},$$
$$\varphi_{\mathbf{n};\, n'l'm'}(x, X) = \psi_{\mathbf{n}}(x)\Psi_{n'l'm'}(X), \tag{21}$$

Here, the primed quantum numbers describe the relative motion; $Ry = \mu e^2/2\varepsilon_0^2\hbar^2$ is the exciton Rydberg; $M = m_c + m_h$; $\mu = m_c m_h/M$; $\psi_{nlm}(x)$ and $\psi_{\mathbf{n}}(x)$ are defined by (11) and (13), respectively; and $\Psi_{n'l'm'}(X)$ are the hydrogen-like wave functions of Wannier excitons. The Fröhlich-type electron–phonon interaction in spherical QDs was studied by two of the authors previously [4, 10]. Matrix elements of this interaction in rectangular QDs are given by

$$V^{(n)}_{\mathbf{n}_2, n_2' l_2' m_2';\, \mathbf{n}_1 n_1' l_1' m_1'} = e f_{\mathbf{n}} G_x G_y G_z \sqrt{\frac{2l_1' + 1}{2l_2' + 1}}$$
$$\times \sum_{q=0}^{\infty} (-1)^q (4q+1) C^{l_2' 0}_{2q0;\, l_1' 0} C^{l_2' m_2'}_{2q0;\, l_1' m_1'} J^{\mathbf{n};\, 2q}_{n_2' l_2';\, n_1' l_1'}, \tag{22}$$

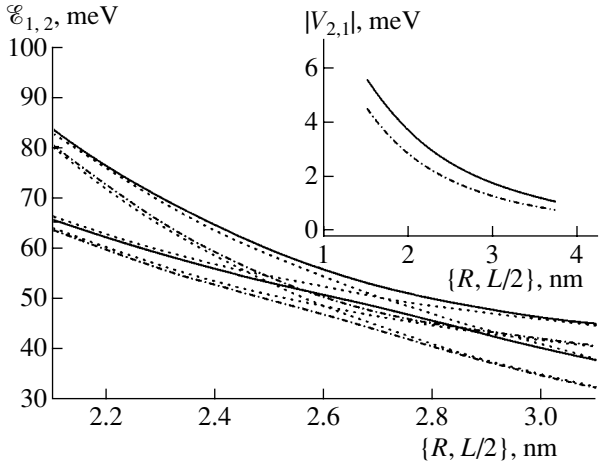

Fig. 2. CuCl QDs in the weak confinement mode: dependence of the polaron-like state energy $\mathscr{E}_{1,2}$ on QD size for the VR of a pair of lowest exciton states with the *LO* phonon. Solid and dash-dot lines refer, respectively, to spherical QD of radius R and cubic QD with edge L. Dotted lines show the size dependence of the $|2; 0\rangle$ and $|1; 1\rangle$ states. *Insert*: matrix element of exciton–phonon interaction as a function of the characteristic linear size of QD.

where $f_{\mathbf{n}}$ and G_i coincide with (18) and (19),

$$J^{\mathbf{n};\,s}_{n_2'l_2';\,n_1'l_1'} = \int_0^\infty dX X^2 [j_s(\rho_h k_{\mathbf{n}} X) - (-1)^s j_s(\rho_c k_{\mathbf{n}} X)] \times F_{n_2'l_2'}(X) F_{n_1'l_1'}(X), \quad (23)$$

$F_{n'l'}(X)$ is the radial hydrogen-like wave function, $\rho_h = m_h/M$, and $\rho_c = m_c/M$. Of particular interest for applications is the Fröhlich interaction of excitons in the ground state of the relative motion of an electron and a hole $n' = 1$, $l' = 0$, $m' = 0$. Matrix elements of the exciton–phonon interaction in spherical and rectangular QDs are then appreciably simplified and differ from the strong-confinement expressions (14) and (17) only by the additional factor

$$B(k) = \frac{1}{(1 + \alpha_k^h/4)^2} - \frac{1}{(1 + \alpha_k^c/4)^2}, \quad (24)$$

where $\alpha_k^{c(h)} = (\rho_{c(h)} R_{\text{ex}} k)^2$, $k = k_{nl}$ for spherical and $k = k_{\mathbf{n}}$ for rectangular QDs. The presence of this factor is extremely important since it is sensitive to the energy-band parameters of the semiconductor (electron and hole effective masses) and affects the size dependence of the interaction. In particular, if the effective masses are equal, this part of the interaction vanishes. If $kR_{\text{ex}} \ll 1$, then $B(k) = k^2 R_{\text{ex}}^2 (m_h - m_c)/2M$ and the matrix elements are, therefore, proportional to $\tilde{R}^{-5/2}$.

Since the exciton–phonon interaction rapidly decreases with increasing QD size, a semiconductor material with not-too-high R_{ex} should be chosen to observe VR in the weak confinement mode. CuCl QDs ($\varepsilon_0 = 5.95$, $\varepsilon_\infty = 4.84$, $\hbar\Omega_{LO} = 25.6$ meV, $m_c = 0.5m_0$, $m_h = 1.6m_0$, and $R_{\text{ex}} = 0.7$ nm [3]) are the most suitable in this regard. The results of the calculation of the energy spectrum renormalization for spherical and cubic CuCl QDs in the case of VR between two lowest exciton states are presented in Fig. 2. The insert shows the size dependence of the exciton–phonon interaction matrix element. It is seen that anticrossing also takes place for VR in the weak confinement mode.

3. EXPERIMENT

In order to study the QD energy spectrum renormalization induced by VR between low-energy exciton states, we obtained and analyzed spectra of the two-photon-excited emission (TPE) in the inhomogeneously broadened ensemble of CuCl QDs in the NaCl matrix. The crystal matrix was used since the QD luminescence bands are narrower in it, compared with glass matrices, and this allowed us to measure more precisely the spectral positions of these bands. At the same time, the exciton parameters in CuCl QDs in the NaCl matrix are sufficiently well known [11–13]. It has been established that CuCl nanocrystals have a cubic shape [11, 12] or even that of a rectangular parallelepiped [13], rather than a spherical one. It has been reliably established that the size dependence of the lower exciton states [13] is well described by expression (21).

The CuCl-doped NaCl crystal was grown by the transverse Bridgman method and annealed at a temperature suitable for the growing of CuCl nanocrystals. The sample had a QD mean size of about 2.4 nm and was characterized by wide size scatter. The one-photon absorption spectrum taken on this sample at the temperature of 2 K is depicted in Fig. 3a. The oscillating fine structure modulating the absorption band is related to a layer-by-layer increase of the nanocrystal size [11]. A range of energy gap values between the lowest (111) and next in energy (211) exciton states is located in the bulk CuCl *LO* phonon range and can be scanned in a single sample without essential loss of the signal intensity. Henceforth, we denote the exciton states by the translation motion quantum numbers (see the preceding section).

The TPE spectra were excited by the pulse radiation of a tunable titanium-sapphire laser pumped by the second harmonic radiation of an Q-switched Nd^{3+}:YAG laser. The linearly polarized excitation radiation had the following parameters: pulse duration, 100 ns; repetition frequency, 1 kHz; pulse power, 3 kW; and spectral width, 1 meV. The radiation was focused by means of a lens with a focal length of 60 mm onto a sample placed in superfluid helium. The secondary emission was collected in the forward direction, spectrally analyzed with a monochromator (0.25 m) with a single diffraction grating (1200 grooves/mm), and detected by a liquid-nitrogen-cooled CCD-camera in the spectral range of the doubled incident-photon energy. The overall spec-

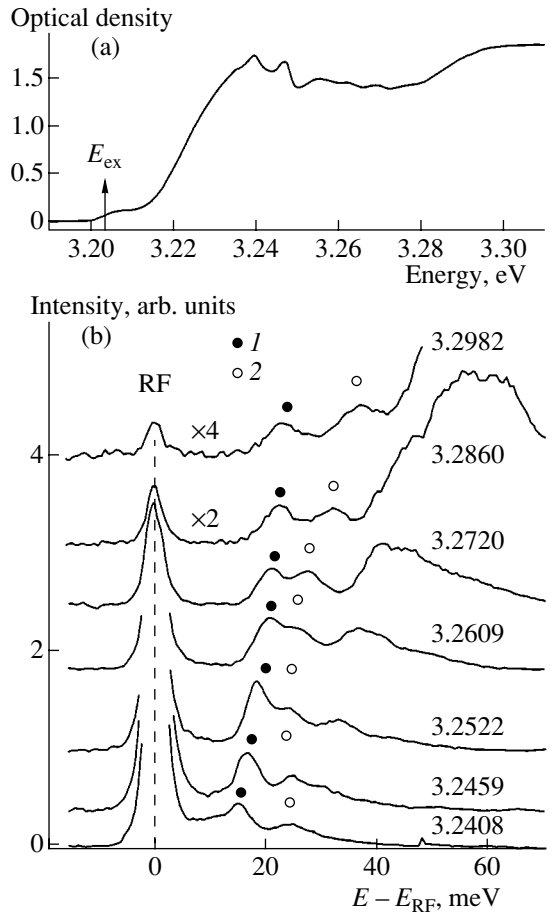

Fig. 3. (a) One-photon absorption spectrum of CuCl QDs grown in the NaCl crystal; sample thickness 0.3 mm, temperature 2 K; E_{ex} is the exciton energy in the bulk. (b) TPE secondary emission spectra of CuCl QDs grown in the NaCl matrix for different excitation energies (doubled photon energies are given in eV). *Abscissa*: Stokes shift $E - E_{RF}$ of the TPE secondary emission energy relative to the resonance fluorescence band RF. (*1*, *2*) Bands under analysis.

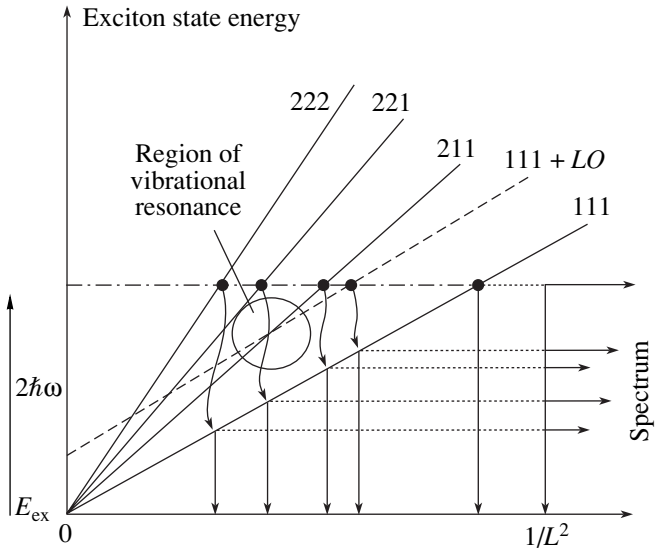

Fig. 4. Diagram illustrating the formation of a TPE secondary emission spectrum for the example of an ensemble of cubic QDs with wide size distribution upon excitation with radiation with doubled photon energy $2\hbar\omega$. L is the cube edge length, E_{ex} is the exciton energy in the bulk. Solid lines show the size dependence of the lower exciton state energies (for designations, see text), dashed line represents the "exciton + *LO* phonon" state. Wavy lines show channels of intraband relaxation of excitons from excited into ground state. The VR region between the lowest and next in energy exciton states is marked.

tral resolution of the experiment equaled 1.5 meV. The excitation radiation passed through the sample was absorbed by a filter based on a saturated aqueous $CuSO_4$ solution. The TPE intensity was quadratic with respect to the exciting radiation intensity, which confirmed the two-photon character of the exciton generation. The spectra were corrected for the absorption of emitted light, since the optical density of the sample changed rapidly in the spectral range being studied.

The QD-size-selective excitation of spectra makes it possible to test the energy structure of QDs of various sizes by changing the incident photon energy. A diagram illustrating the formation of a spectrum of secondary emission from a QD ensemble with a wide size distribution is presented in Fig. 4. The incident radiation with photon energy $\hbar\omega$ simultaneously generates excitons in the lowest energy state of the QDs of an appropriate size and in high-energy states of larger QDs, satisfying the equation $2\hbar\omega = E_{\mathbf{n};000}$, where $E_{\mathbf{n};000}$ is defined by (21). The secondary emission spectra are then formed due to the annihilation of the exciton in the lowest energy state (111), both excited directly by light (Fig. 3b, band RF) and populated due to intraband relaxation from the high-energy states. Analysis of the dependence of band energies on the incident photon energy, using (21), allows us to obtain data on the QD energy structure. This analysis is commonly performed using the dependence of the energy gap (Stokes shift) between the RF band and other bands, $E - E_{RF}$, on the energy shift of the lowest exciton state, $E_{111} - E_{ex}$, induced by a spatial confinement where $E_{ex} = E_g - Ry$ is the exciton energy in the bulk material. It is clear that, in the case of size-selective excitation, $E_{111} = 2\hbar\omega$. An example of such an approach to determining the exciton spectrum of the spherical CuCl QDs in the glass matrix can be found in [14]. Here, we restrict ourselves to the analysis of the bands related to 211 and 111 + *LO* states upon the excitation of QDs in the range of VR between the two lowest exciton levels (Fig. 4). As shown above, the degeneracy of 211 and 111 + *LO* states is lifted in the case of VR, which is manifested as the anticrossing effect.

A representative set of TPE secondary emission spectra corresponding to excitation with different photon energies is shown in Fig. 3b. The symbols *1* and *2* denote the bands under analysis. It is seen that the spec-

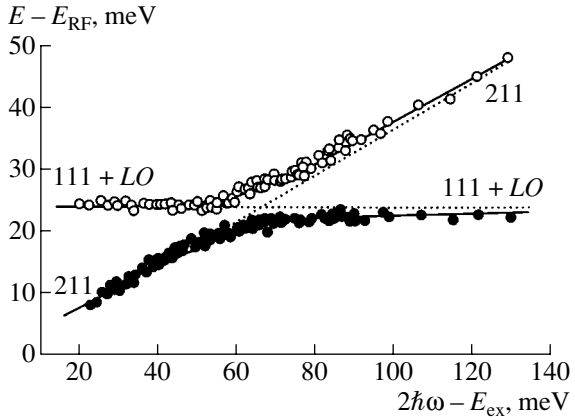

Fig. 5. Stokes shift of the TPE secondary emission bands on $2\hbar\omega - E_{ex}$, demonstrating anticrossing of the 211 and 111 + *LO* states in VR between 211 and 111 states in CuCl QDs. Circle diameter corresponds to experimental errors in determining the band energies. Dotted lines show the energies of the corresponding states in the absence of exciton–phonon interaction; solid lines represent calculation results for QDs in the shape of a rectangular parallelepiped.

tra essentially depend on the excitation energy. The dependences of the Stokes shifts of these bands on $2\hbar\omega - E_{ex}$, clearly demonstrating anticrossing in the VR range, are presented in Fig. 5.

4. DISCUSSION

We have compared the experimental data with the calculations, carried out within the framework of the model developed by us, of the VR between the lowest exciton states in QDs having a rectangular parallelepiped shape (21). The best agreement between theory and experiment (Fig. 5) is achieved for the parallelepiped with two equal edges, L_y and L_z, and the third, L_x, α times longer. In this case, the polaron-like state energies are described by (7)–(9), in which the lowest exciton energies have the following form:

$$E_{111} = E_{ex} + \frac{\hbar^2\pi^2}{2ML^2}\left(\frac{1}{\alpha^2} + 2\right),$$
$$E_{211} = E_{ex} + \frac{\hbar^2\pi^2}{2ML^2}\left(\frac{4}{\alpha^2} + 2\right); \quad (25)$$

the matrix element of exciton–phonon interaction, $V^{(1)}_{2,1} = V^{(211)}_{211,111} B(k_{211})$, where $V^{(211)}_{211,111}$ and $B(k_{211})$ are defined by expressions (17) and (24), respectively. It can be seen from Fig. 5 that the results of the calculation of the Stokes shifts of the bands under consideration are in agreement with experimental data at α = 1.45, which was found by the least-squares method.

Our model also describes similar experimental data obtained in [6], which differ from ours only by the slope of the asymptotic 211 (see Fig. 5). Excellent agreement between calculation and experiment occurs at α = 1.55. This means that CuCl nanocrystals in the cited work had a rectangular parallelepiped shape with a long edge somewhat larger than that in our case. This is quite natural since the conditions of sample preparation were different.

It is noteworthy that, in accordance with the selection rules, the phonon with quantum number 211 is involved in the VR. The energy of this phonon (24 meV), used in calculations, was determined from the Stokes shift of the 111 + *LO* band, measured in the limit of small $2\hbar\omega - E_{ex}$. Detailed analysis shows that far from the resonance, at large $2\hbar\omega - E_{ex}$ corresponding to the excitation of small QDs, the energy of the polaron-like state tends towards the asymptotic value $E_{111} + \hbar\Omega_{211}$ at a much slower rate than that in the case of small $2\hbar\omega - E_{ex}$. Such behavior is related to the strong size-dependence of the electron–phonon interaction (see the insert of Fig. 2). This dependence implies that the effect of the VR on the energy spectrum is important for small QDs even far from the VR. The exciton–phonon interaction becomes proportional to $\tilde{R}^{-5/2}$ with increasing QD size, and the influence of VR on the energy spectra can be neglected at large $\tilde{R}$.

5. CONCLUSION

In conclusion, we formulate the main results of this study.

The problem of the renormalization of the semiconductor QD energy spectrum, induced by VR, was solved. Analytical expressions have been obtained for energies of the polaron-like states in spherical and rectangular QDs in the cases of weak and strong confinement. Expressions for the matrix elements of the interaction of *LO*-phonons with electrons and excitons are derived for rectangular QDs.

Renormalization of the QD energy spectrum under conditions of VR between the lowest exciton states is studied experimentally for the example of rectangular CuCl QDs in the NaCl matrix at 2 K by means of TPE resonance spectroscopy of secondary emission.

Quantitative agreement of the calculation results with experimental data demonstrated the adequacy of the model developed by us for energy spectrum modification in semiconductor QDs under VR conditions.

ACKNOWLEDGMENTS

Two of the authors (A. V. F. and A. V. B.) thank the Russian Foundation for Basic Research (project nos. 99-02-16323 and 01-02-17060) and the program “Physics of Solid-State Nanostructures” (project no. 99-1136) for financial support.

REFERENCES

1. I. B. Levinson and É. I. Rashba, Usp. Fiz. Nauk **111**, 683 (1973) [Sov. Phys. Usp. **16**, 892 (1973)].
2. U. Woggon, *Optical Properties of Semiconductor Quantum Dots* (Springer-Verlag, Berlin, 1997).
3. T. Itoh, M. Nishijima, A. I. Ekimov, *et al.*, Phys. Rev. Lett. **74**, 1645 (1995).
4. A. V. Fedorov and A. V. Baranov, Zh. Éksp. Teor. Fiz. **110**, 1105 (1996) [JETP **83**, 610 (1996)].
5. A. V. Fedorov, A. V. Baranov, and K. Inoue, Phys. Rev. B **54**, 8627 (1996).
6. K. Edamatsu, M. Tsukii, K. Hayashibe, *et al.*, Nonlinear Opt. **18** (2–4), 295 (1997).
7. L. Zimin, S. V. Nair, and Y. Masumoto, Phys. Rev. Lett. **80**, 3105 (1998).
8. M. C. Klein, F. Hache, D. Ricard, and C. Flytzanis, Phys. Rev. B **42**, 11123 (1990).
9. *Landolt-Börnstein, New Series, Group III*, Vol. 17a: *Semiconductors*, Ed. by O. Madelung, M. Schulz, and H. Weiss (Springer-Verlag, Berlin, 1982).
10. A. V. Fedorov, A. V. Baranov, and K. Inoue, Phys. Rev. B **56**, 7491 (1997).
11. T. Itoh, S. Yano, N. Katagiri, *et al.*, J. Lumin. **60–61**, 396 (1994).
12. N. Sakakura and Y. Masumoto, Phys. Rev. B **56**, 4051 (1997).
13. J. Zhao, M. Ikezawa, A. Fedorov, and Y. Masumoto, J. Lumin. **87–89**, 525 (2000).
14. A. V. Baranov, Y. Masumoto, K. Inoue, *et al.*, Phys. Rev. B **55**, 15675 (1997).

Translated by S. Ktitorov

Semiconductors, Vol. 35, No. 12, 2001, pp. 1398–1403. Translated from Fizika i Tekhnika Poluprovodnikov, Vol. 35, No. 12, 2001, pp. 1460–1465.

AMORPHOUS, VITREOUS, AND POROUS SEMICONDUCTORS

Scanning Tunneling Spectroscopy of *a*-C:H and *a*-C:(H, Cu) Films Prepared by Magnetron Sputtering

T. K. Zvonareva*, V. I. Ivanov-Omskiĭ*, V. V. Rozanov, and L. V. Sharonova*, [1]**

** Ioffe Physicotechnical Institute, Russian Academy of Sciences, Politekhnicheskaya ul. 26, St. Petersburg, 194021 Russia*

[1] e-mail: shar@nano.ioffe.rssi.ru

*** Institute of Analytical Instrument Making, Russian Academy of Sciences, Rizhskiĭ pr. 26, St. Petersburg, 198103 Russia*

Submitted July 30, 2001; accepted for publication August 29, 2001

Abstract—Scanning tunneling spectroscopy was used to study *a*-C:H and *a*-C:(H, Cu) films under atmospheric conditions; these films were formed on semiconductor (Si) and metallic (Cr/Si) substrates using dc magnetron sputtering of graphite or graphite/copper targets. The local density of electron states was determined from normalized differential tunneling conductance with the aim of probing the individual sp^2-phase clusters. The well-defined valence-band edge and the varying (i.e., dependent on the scanning coordinate) shape of the distribution of the density of electron states within the conduction band are characteristic of the *a*-C:H films; also, the largest experimental value of the band gap in these films is ~ 3 eV; finally, the tendency towards the stable position of the Fermi level at a level of ~ 1 eV above the valence-band top is observed in *a*-C:H films. The *a*-C:(H, Cu) films are homogeneous with respect to the local density of electron states, which is accounted for by the formation of a homogeneous surface layer in the course of growth. © *2001 MAIK "Nauka/Interperiodica".*

1. INTRODUCTION

Various modifications of amorphous carbon, including amorphous hydrogenated carbon (*a*-C:H), continue to attract attention as promising materials for numerous applications. The possibility of using carbon films in electronics (for example, for the development of single-electron transistors [1] or cold cathodes for displays [2]) has been discussed more and more actively. The microstructure and nanostructure of the above materials should be studied in order to efficiently solve application-oriented problems.

Previously [3] (see also the later publications [4–6]), amorphous carbon has been considered as an inhomogeneous medium that includes the fragments of two phases, i.e., atoms with tetragonal and trigonal coordination, which feature the sp^3 and sp^2 hybridization of atomic orbitals, respectively. The volume ratio of the phases depends on the methods and conditions of the film growth. For the sp^3 phase, the electron energy bands (the filled and empty ones) are formed by the σ and σ^* states, with the HOMO–LUMO gap being equal to ~ 5 eV. For the sp^2 phase, there are bands of the π and π^* states (occupied and unoccupied) in addition to the σ and σ^* bands with an even smaller energy gap; the π and π^* bands are located close to the Fermi level and control the electronic properties (such as electrical conductivity or optical absorption) of these materials.

The presence of atoms in the sp^2 configuration and the resulting emergence of the electronic π and π^* states represent specific features that distinguish amorphous carbon from other amorphous materials of Group IV, in particular, amorphous silicon. As a result, the model applied to amorphous silicon is found to be inapplicable to amorphous carbon. According to this model, tetrahedral coordination inherent in the crystalline analogue is preserved in amorphous material, whereas the positional disordering of atoms is accounted for in terms of the tails in the density of states in the band gap [7]. Therefore, the model of a two-phase mesoscopic medium, consisting of a system of sp^2 graphite or graphite-like clusters, has recently been used more and more frequently in order to interpret the experimental data on amorphous carbon; these clusters are assumed to be either embedded into the sp^3 phase or connected to each other by the sp^3 bridges. The model of graphite clusters has been used to interpret the results of various experiments, for example, those involving Raman scattering [6, 8] or the optical-absorption edge [9] in *a*-C:H. According to this cluster-based model, the observed electronic effects should include the additive contributions of individual clusters; however, these contributions are supposed to be nonseparable in macroscopic experiments, in which case the density of electron states manifests itself as a spatially integrated characteristic.

At the same time, it is well known that experimental data on the local density of states (DoS) in the vicinity of the Fermi level can be obtained using scanning tunneling spectroscopy (STS). In this method, the density

of both occupied and unoccupied states (in the valence and conduction bands) is probed; the band gap can be determined as well [10]. STS has been used recently to study amorphous carbon (*a*-C) films [11, 12]. However, only tetrahedral *a*-C (*ta*-C) films were studied; some of the films were doped with nitrogen. From the standpoint of the practical implementation of *a*-C films, the issue concerning the electron-state spectrum as a spatially varying characteristic (in particular, in the *a*-C:H films) is of special interest; this issue has not been considered thus far.

In this paper, we report the results of using STS to study films of undoped *a*-C:H and *a*-C:H doped with copper [*a*-C:(H, Cu)]. Similar a-C:H films have been studied previously using various methods; in a number of studies, as mentioned above, the model of graphite (graphite-like) clusters was employed to interpret the results. We included *a*-C:(H, Cu) films in our studies in connection with recent interest in the modification of *a*-C using metals (embedment of metallic clusters in carbon). On the basis of previous experiments, it was concluded that copper can be partially incorporated into a carbon network in the form of individual atoms and, thus, can dope (intercalate) the graphite cluster. If the copper concentration is high, Cu can precipitate in the form of metallic drops; i.e., it can form its own system of nanoclusters [13–16]. The objective of this study was to measure the local DoS in *a*-C:H and *a*-C:(H, Cu) films by scanning their surface in order to assess to what extent the local DoS, measured on a scale of tens–hundreds of nanometers, varies from point to point.

2. EXPERIMENTAL

The *a*-C:H films were obtained by the dc magnetron sputtering of a graphite target in an argon–hydrogen plasma (80%Ar + 20%H_2). In order to obtain the *a*-C:(H, Cu) films, we covered the graphite target with copper plates. Substrates for deposition of the films were transferred to the sputtering chamber after they had been heated to 200°C. Residual pressure in the chamber was 10^{-6} Torr. The films were deposited in the operating-gas flow under a pressure of 10^{-2} Torr and with an ion-current density of 10^{-1} A/cm^2; the negative self-bias at the substrate was no higher than 10 V. According to our preliminary studies [17], the ratio between atomic concentrations of copper and hydrogen in the *a*-C:(H, Cu) films was [Cu]/[C] = 0.3–0.4 under the employed technological conditions of sputtering.

The *a*-C:H and *a*-C:(H, Cu) films with a thickness in the range of 70–130 nm were deposited on substrates of two types: (1) chemically polished wafers of silicon of the brand KEF-1 (*n*-Si:P, $\rho = 1\ \Omega$ cm) with a ~ 1.5-μm-thick heavily doped surface layer (phosphorus was diffused from the surface; the electron concentration in the layer was ~ 10^{21} cm^{-3}); and (2) chemically polished wafers of silicon of the brand KDB-20 (*p*-Si:B, $\rho = 20\ \Omega$ cm) with a ~ 200-nm-thick Cr layer deposited by high-frequency ion–plasma sputtering (in this case, the actual substrate for the deposited film was the Cr layer). The different types of substrates, i.e., semiconducting (Si) and metallic (Cr), were chosen from considerations of the possible effect of the substrate properties on the structure of the films.

The tunneling current–voltage (*I–V*) characteristics I(*V*) were measured under atmospheric conditions using a scanning tunneling microscope; the bias voltage *V* applied to the gap between the probe and the sample ranged from –2.5 to +2.5 V, with positive voltages corresponding to a positive potential of the sample. A tungsten tip, fabricated using electrochemical etching, was used as the probe. The functional capabilities of the tunneling microscope employed have been described elsewhere (see, for example, [18]).

The measurements were performed under conditions of a constant tip–surface gap that corresponded to the current of $I_0 = 1$ nA at a bias voltage of +2.5 V (the reference current). We found from preliminary measurements of the tunneling *I–V* characteristics at various reference currents in the range of $I_0 = 0.5$–4.0 nA (for different gaps) that the shape of *I–V* characteristics and the general behavior of the derivative dI/dV are independent of the gap. However, in connection with the fact that the current fluctuations amounted to ~0.002 nA (this corresponded to the accuracy of setting the current), measurements at large gaps were found to be insufficiently precise; therefore, all the measurements were performed at the reference current of $I_0 = 1$ nA.

We measured the *I–V* characteristics 25 times at each point under scanning conditions with the step ranging from 15 to 300 Å; the scanned sites were chosen within different areas of the film surface. The *I–V* characteristic was averaged over 25 measurements and was additionally smoothed using a Fourier filter; the normalized differential conductance $(dI/dV)/(I/V)$ was then calculated. In order to eliminate the zero-point anomaly in $(dI/dV)/(I/V)$, a small quantity was added to I/V. According to [10], the dependence of $(dI/dV)/(I/V)$ on the bias voltage is representative of the distribution of the density of electron states over the energy $E = eV$ (e is the elementary charge); $V = 0$ corresponds to the Fermi level (E_F), negative bias voltages correspond to occupied states ($E < E_F$), and positive bias voltages correspond to unoccupied states ($E > E_F$).

3. RESULTS AND DISCUSSION

The obtained dependences of $(dI/dV)/(I/V)$ on the bias voltage *V* for the *a*-C:H films on the Si substrate are shown in Fig. 1. Two of the most differing curves were chosen from numerous measured dependences in order to illustrate most clearly the range of variations in the spectrum of electron states. In both cases, the edges of occupied states (conventionally, in the valence band) and of unoccupied states (conventionally, in the con-

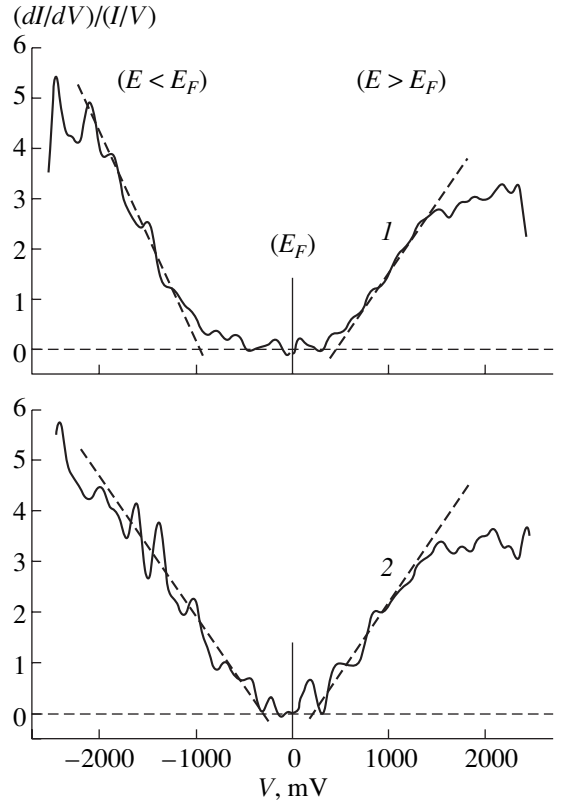

Fig. 1. Normalized differential conductance as a function of the bias voltage; the dependences were derived from the averaged tunneling current–voltage characteristics measured for *a*-C:H films on the Si substrate. Curves *1* and *2* represent typical dependences that illustrate the range of variations in the local density of electron states at the film surface.

duction band) are clearly observed; these edges are approximated by the straight lines in Fig. 1. The cutoffs at the voltage axis at a level of $(dI/dV)/(I/V) = 0$ (the zero tunneling current) make it possible to determine the band gap E_g: E_g = 1.45 eV for curve *1*, and E_g = 0.5 eV for curve *2*. In other measurements, we obtained intermediate or identical values of E_g; i.e., 0.5 eV $\lesssim E_g \lesssim$ 1.5 eV. The data represented in Fig. 1 were obtained under scanning conditions with a step of ~300 Å; we note that alternation of curves of the *1* and *2* types was observed for this scanning step. Approximating curves to the right and left of the Fermi level have the same slope; i.e., the energy distributions of electron states for $E < E_F$ and for $E > E_F$ are identical. As can be seen from Fig. 1, curves *1* and *2* differ not only in E_g, but also in the fact that the Fermi level E_F is located symmetrically in reference to the band edges for curve *2*, whereas E_F is shifted to the conduction-band edge for curve *1*. Thus, the spectrum of electron states varies substantially in the course of scanning. If we rely on the concepts of the previous model [3], the compact clusters consisting of hexagonal (of the graphite type) rings may be formed with high probability in the *a*-C films; in this case, the experimental curves of the local DoS may be considered as the characteristics of individual clusters of this type. However, a more thorough analysis shows that such a simplified model is inconsistent with experimental results. We now dwell in more detail on experimental spectra.

First, the lower boundary of the experimental values of E_g ($E_g \approx 0.5$ eV) is too small a value compared to the optical band gap in the *a*-C:H films (see [3]). The value of E_g = 1.92 eV has been reported previously [19] for films grown similarly. At the same time, the value of $E_g \approx 0.5$ eV is in the range of band gaps characteristic of nonhydrogenated *a*-C. In the context of the model of sp^2 clusters, the value of $E_g \approx 0.5$ eV implies the existence of large clusters that consist of dozens of hexagonal rings, which are considered as characteristic of *a*-C and as unlikely for *a*-C:H [3].

Second, the density of the π and π^* states in the compact sp^2 clusters should be symmetric in reference to the Fermi level. In fact, it follows from curve *2* in Fig. 1 that the edges of the bands of occupied and unoccupied states are symmetric with respect both to the general form of these edges and to their location relative to the Fermi level. The pattern is also symmetric for curve *1* (the same slope of the left- and right-hand portions of the approximating curves) if we consider the form of the band edges; however, in this case, the Fermi level is located closer to the unoccupied-state band than to the occupied-state band. We note that a shift of the Fermi level to the conduction band has been observed previously [11, 12], however, only as a result of doping of the *a*-C films.

Third, as was assumed previously [3], individual hexagonal clusters with an energy gap between the bands of the π and π^* states equal to ~ 5 eV should have the highest probability of being formed. As was mentioned above, values of E_g larger than 1.5 eV were not obtained in our experiments. However, a detailed analysis of the experimental data makes it possible to reduce this discrepancy. The point is that, although we are dealing with the local DoS, the measurements are actually performed over a finite film area comparable to the grain size; thus, individual rings may simply remain undetected. At the same time, when measuring a number of *I–V* characteristics, disruptions of tunneling current occur occasionally; it is because of this fact that the averaged *I–V* characteristics were reported above. It is quite probable that the disruptions are related to instability of the current channels and to switching between these channels (switching from one cluster to another in the course of measurements). If we consider a set of individual (unaveraged) *I–V* characteristics, we find among them those whose transformation into normalized differential conductance yields a band gap as large as 3 eV. One of such curves is shown in Fig. 2.

It is noteworthy that pronounced oscillations are observed in the range of both positive and negative bias voltages in the curves shown in Fig. 1; these oscilla-

tions are regular and are not eliminated by smoothing. As shown previously [10], such oscillations are characteristic of amorphous carbon with a high concentration of atoms in the sp^2 configuration; these oscillations were identified phenomenologically [10] with the localized π states. In the context of the cluster model, such states may be attributed, for example, to dangling bonds at the surface (at the outer shell) of graphite clusters or to local distortions of the carbon rings.

The results obtained for a *a*-C:H film on the Cr/Si substrate are shown in Fig. 3. Here, as in Fig. 1, two typical dependences $(dI/dV)/(I/V) = f(V)$ are shown. It can be seen that these dependences differ markedly from those shown in Fig. 1 for the films deposited on the Si substrate: they are asymmetric; in addition, we observe a sharp cutoff of $(dI/dV)/(I/V)$ in the region of negative bias voltages and a slow increase for positive bias voltages. The difference between the curves in Figs. 1 and 3 indicates that the structure of films grown under identical conditions depends heavily on the substrate material. We have shown previously [18] that the substrate material affects the properties deposited on the quartz and silicon substrates. We have observed [18] differences in the growth rate and in the refractive index of the films; however, these differences have not been great. By comparing the curves in Figs. 1 and 3, we may conclude that the use of metallic coating as the substrate affects the film structure. It is not quite clear so far which factor plays the determining role—the distribution of potentials in the growth chamber when a metallic substrate is used, the chemical nature of the metal, or the structural characteristics of the metal coating.

Examination of the data in Fig. 3 and identification of the curves with the DoS hardly gives us any indication of the band gap at all. A sharp edge in the region of negative bias voltages can apparently be identified with the valence-band edge. It is noteworthy that the Fermi level (E_F) position in reference to the valence-band edge for this film (an *a*-C:H film on the Cr/Si substrate) remains almost unchanged at various points of the scanned surface and is close to E_F deduced from curve *1* in Fig. 1 and from Fig. 2; i.e., it is close to E_F for an *a*-C:H film on the Si substrate, in which case the widest band gap is observed. The conduction-band edge does not manifest itself explicitly; only a gradual, almost linear increase in the DoS from the Fermi level (curve *1*) or an increase with a step at $V \approx 0$ (curve *2*) are observed.

In spite of differences in the representative spectra shown in Figs. 1–3, we can detect a number of special features common to the *a*-C:H films. As a rule, a drastic change in the value of $(dI/dV)/(I/V)$ is distinguished in the curves in the region of negative bias voltages ($E < E_F$); this change can be identified with the valence-band edge. Moreover, the intersection of the approximating straight line with the line, $(dI/dV)/(I/V) = 0$, yields almost the same values of the cutoff voltage (about –1 V)

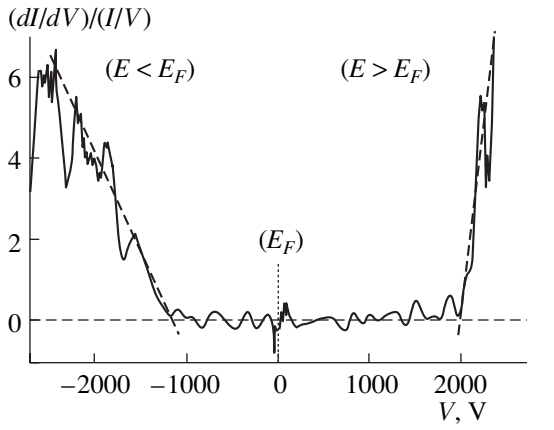

Fig. 2. Normalized differential conductance as a function of the bias voltage; the dependence was derived from a single current–voltage characteristic (without averaging) for an *a*-C:H film on the Si substrate.

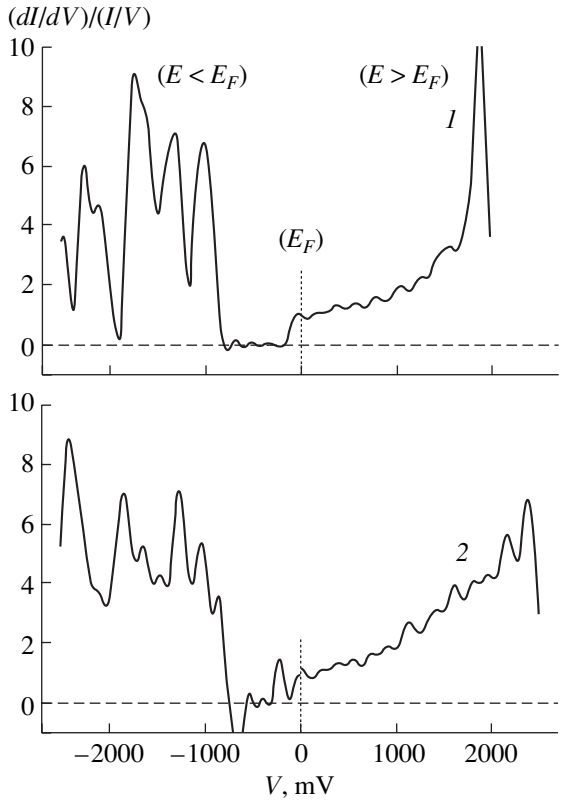

Fig. 3. Normalized differential conductance as a function of the bias voltage; the dependences were derived from the averaged tunneling current–voltage characteristics for an *a*-C:H film on the Cr/Si substrate. Curves *1* and *2* represent typical dependences that illustrate the range of variations in the local density of electron states at the film surface.

for most of the curves. This means that there is a distinct tendency towards a stable position of the Fermi level at an energy of ~ 1 eV above the valence-band edge. The shape of the spectra in the region of positive

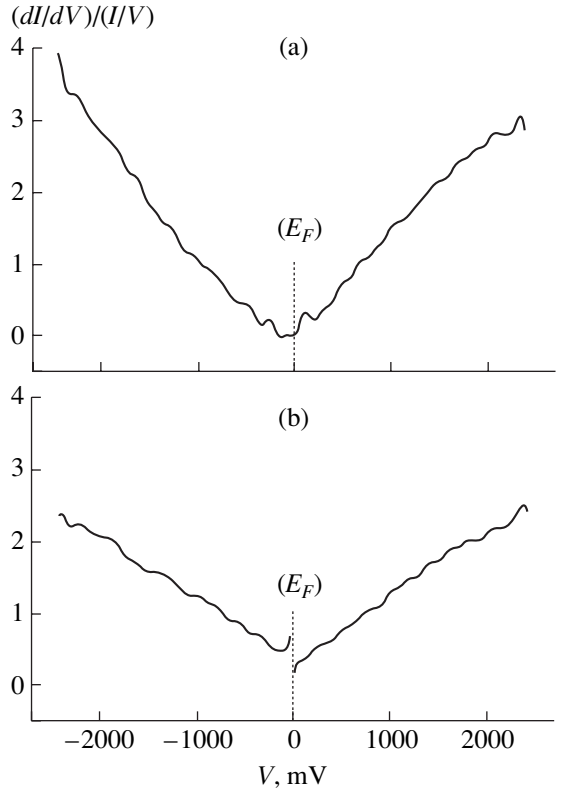

Fig. 4. Normalized differential conductance as a function of the bias voltage; the dependences were derived from the averaged tunneling current–voltage characteristics for the *a*-C:(H, Cu) films on the (a) Si and (b) Cr/Si substrates.

bias voltages ($E > E_F$) is more changeable; on the one hand, the shape of the $(dI/dV)/(I/V) = f(V)$ curves varies appreciably if the scanning step is equal to 300 Å, whereas, on the other hand, this shape is different for the films deposited onto dissimilar substrates. Apparently, we may assume that the "true" edge of the valence band (the band of delocalized states) is distinguishable in Fig. 2. This assumption is based on the following two circumstances: (i) the density of electron states changes rapidly from the value close to zero, and (ii) the band gap determined in this case has the largest value determined from all experiments ($E_g \approx 3$ eV). In other spectra, the valence-band edge is diffuse, which may be naturally related to the localized states that are distributed in energy, with the spectrum depending on the coordinate of scanning. Apparently, curve *2* in Fig. 1 represents the situation where a broad spectrum of localized stated emerges not only in the vicinity of the conduction band but also near the valence band.

In Fig. 4, we show the dependences $(dI/dV)/(I/V) = f(V)$ for two *a*-C:(H, Cu) films grown on the Si and Cr/Si substrates using the same technological process. The results of the measurements for these films differed radically from those for the *a*-C:H films; specifically, the *I–V* characteristics were reproduced with a high accuracy in the course of multiple measurements. The shape of the $(dI/dV)/(I/V) = f(V)$ curves also differs from that of the curves considered previously for *a*-C:H: the spectra for *a*-C:(H, Cu) are smoother and do not feature any oscillations.

We have previously measured the macroscopic electrical conductivity in the films of the same type on the silicon and quartz substrates; the results have been interpreted using a high-resistivity matrix model that contains the conducting clusters composed of either graphite (or graphite-like material) or copper (if the copper concentration is high) [20]. Based on these data, we expected that scanning of the film surface would lead to radically different tunneling *I–V* characteristics related to the clusters of dissimilar types. However, in both cases (i.e., for the films on the Si and Cr/Si substrates), we failed to observe the aforementioned differences.

The bands of unoccupied and occupied states concentrated in the vicinity of the Fermi level (as in the case of the bands in graphite) are observed in the spectrum of the *a*-C:(H, Cu) film on the Si substrate (Fig. 4a). Notwithstanding the fact that the shape of the spectra varies somewhat with the coordinate of scanning, it is impossible to find the regions with a nonzero band gap. According to the measurements of the tunneling *I–V* characteristics, it turns out that the *a*-C:(H, Cu) films appear more homogeneous compared to the *a*-C:H films. At first glance, this contradicts the previous data [21] on similar *a*-C:(H, Cu) films; these data indicate that bulk structural inhomogeneities oriented from the substrate to the surface are present in these films. The absence of the effect of these inhomogeneities in the measured spectra of the density of electron states suggests that a homogeneous surface layer is formed in the course of growth of the carbon film with the involvement of copper; this layer differs in its structure from the bulk, and it is this layer that is probed in the method of tunneling spectroscopy.

Even more smoothed dependences are observed for a *a*-C:(H, Cu) film on the Cr/Si substrate (Fig. 4b); these dependences are well reproduced at any scanned area and feature a small amplitude of variation in the value of $(dI/dV)/(I/V)$. Obviously, in the situation under consideration, copper plays an even more important role in the formation of the structure of the film (or the surface layer) than in the case of *a*-C:(H, Cu) film on the silicon substrate.

4. CONCLUSION

Thus, we may advance the following conclusions on the basis of the data obtained by using scanning tunneling spectroscopy to study the *a*-C:H and *a*-C:(H, Cu) films produced by dc magnetron sputtering.

(i) Consistent with the results of our previous studies, we ascertained that the properties of *a*-C:H and *a*-C:(H, Cu) films depend heavily on the substrate material [semiconducting (Si) or metallic (Cr)]. In our

experiments, this manifests itself in the density of electron states.

(ii) The local density of electron states in the *a*-C:H films varies appreciably on the nanometer scale. Diversity in the shapes of electron spectra may be considered as a manifestation of the variability in the material's structure components represented by the clusters of carbon atoms in the sp^2 configuration. Each spectrum is related to an individual cluster.

(iii) The general pattern of the local density of electron states in the *a*-C:H films is as follows. The valence-band edge (a sharp change in the density of electron states in the region of $E < E_F$) manifests itself in the majority of the obtained spectra. For $E > E_F$, the energy dependences of the density of electron states have various shapes; however, these dependences are represented by a broad smooth distribution, without sharp changes in the form of a step or jump, which may be interpreted as the conduction-band edge. It is not often that one encounters spectra in which both the valence- and conduction-band edges can be clearly detected. The band gap determined from such spectra is the widest and amounts to ~ 3 eV. Another special feature following from experimental spectra consists in the pronounced tendency towards a stable position of the Fermi level at ~ 1 eV above the valence-band top.

(iv) In the measurements of the local density of electron states, the *a*-C:(H, Cu) films appear homogeneous, in contrast to the *a*-C:H films; i.e., clusters in the film structure are not observed (we refer to both the Cu drops and the clusters similar to those observed in *a*-C:H). Thus, copper is conducive to the formation of a homogeneous structure; presumably, copper acts as a dopant or intercalating agent for the graphite component of the film material. It is likely that a homogeneous surface layer (of the graphitized type) is formed when the film is grown on a silicon substrate; the effect of copper is even more pronounced in this layer if the film is grown on a metallic substrate.

ACKNOWLEDGMENTS

This study was supported by the Russian Foundation for Basic Research, project nos. 00-02-16994 and 00-02-17004.

REFERENCES

1. W. Chen, A. N. Korotkov, and K. Likharev, Appl. Phys. Lett. **68** (14), 1954 (1996).
2. J. Robertson, Thin Solid Films **296**, 61 (1997); J. D. Carey and S. R. P. Silva, Diamond Relat. Mater. **10**, 873 (2001).
3. J. Robertson and E. P. O'Reilly, Phys. Rev. B **35** (6), 2946 (1987).
4. J. Robertson, Phys. Rev. B **53**, 16302 (1996).
5. D. R. McKenzie, Rep. Prog. Phys. **59**, 1611 (1996).
6. K. W. R. Gilkes, S. Prawer, K. W. Nugent, *et al.*, J. Appl. Phys. **87** (10), 7283 (2000).
7. A. Madan and M. Shaw, *The Physics and Applications of Amorphous Semiconductors* (Academic, Boston, 1988; Mir, Moscow, 1991).
8. J. Schwan, S. Ulrich, V. Batori, *et al.*, J. Appl. Phys. **80** (1), 440 (1996).
9. V. I. Ivanov-Omskiĭ, A. V. Tolmatchev, and S. G. Yastrebov, Fiz. Tekh. Poluprovodn. (St. Petersburg) **35** (2), 227 (2001) [Semiconductors **35**, 220 (2001)].
10. R. M. Feenstra, J. A. Stroscio, and A. P. Fein, Phys. Rev. Lett. **58**, 1192 (1987); R. M. Feenstra and J. A. Stroscio, J. Vac. Sci. Technol. B **5** (4), 923 (1987); R. M. Feenstra, Phys. Rev. B **50** (7), 4561 (1994).
11. C. Arena, B. Kleinsorge, J. Robertson, *et al.*, J. Appl. Phys. **85** (3), 1609 (1999).
12. S. Bhattacharyya, K. Walzer, M. Hietschold, and F. Richter, J. Appl. Phys. **89** (3), 1619 (2001).
13. V. I. Ivanov-Omskii, A. V. Tolmachev, and S. G. Yastrebov, Philos. Mag. B **73**, 715 (1996).
14. V. I. Ivanov-Omskiĭ, V. I. Siklitskiĭ, and S. G. Yastrebov, Fiz. Tverd. Tela (St. Petersburg) **40** (3), 568 (1998) [Phys. Solid State **40**, 524 (1998)].
15. A. V. Kolobov, H. Oyanagi, S. G. Yastrebov, *et al.*, J. Surf. Anal. **4** (2), 377 (1998).
16. V. I. Ivanov-Omskiĭ and É. A. Smorgonskaya, Fiz. Tekh. Poluprovodn. (St. Petersburg) **32** (8), 931 (1998) [Semiconductors **32**, 831 (1998)].
17. T. K. Zvonareva, V. M. Lebedev, T. A. Polyanskaya, *et al.*, Fiz. Tekh. Poluprovodn. (St. Petersburg) **34** (9), 1135 (2000) [Semiconductors **34**, 1094 (2000)].
18. A. O. Golubok, D. N. Davydov, S. A. Masalov, *et al.*, Poverkhnost, No. 3, 146 (1989).
19. V. I. Ivanov-Omskiĭ, A. V. Tolmatchev, and S. G. Yastrebov, Fiz. Tekh. Poluprovodn. (St. Petersburg) **35** (2), 227 (2001) [Semiconductors **35**, 220 (2001)].
20. T. K. Zvonareva and L. V. Sharonova, Fiz. Tekh. Poluprovodn. (St. Petersburg) **33** (6), 742 (1999) [Semiconductors **33**, 684 (1999)].
21. T. K. Zvonareva, V. I. Ivanov-Omskiĭ, A. V. Nashchekin, and L. V. Sharonova, Fiz. Tekh. Poluprovodn. (St. Petersburg) **34** (1), 96 (2000) [Semiconductors **34**, 98 (2000)].

Translated by A. Spitsyn

Semiconductors, Vol. 35, No. 12, 2001, pp. 1404–1417. Translated from Fizika i Tekhnika Poluprovodnikov, Vol. 35, No. 12, 2001, pp. 1466–1480.

PHYSICS OF SEMICONDUCTOR DEVICES

InAsSb/InAsSbP Double-Heterostructure Lasers Emitting in the 3–4 μm Spectral Range[1]

T. N. Danilova, A. N. Imenkov, N. M. Kolchanova, and Yu. P. Yakovlev*

Ioffe Physicotechnical Institute, Russian Academy of Sciences, Politekhnicheskaya ul. 26, St. Petersburg, 194021 Russia

** e-mail: yak@iropt1.ioffe.rssi.ru*

Submitted April 4, 2000; accepted for publication April 10, 2000

Abstract—Our earlier reports concerning the fabrication by liquid-phase epitaxy and investigation of InAsSbP/InAsSb/InAsSbP double heterostructure lasers emitting at 3–4 μm are reviewed. The dependences of spectral characteristics and the spatial distribution of the laser emission on temperature and current are discussed. Lasing modes are shifted by 0.5–1.0 cm^{-1} to longer wavelengths with increasing temperature. The tuning of the lasing modes by means of current is very fast (10^{-8}–10^{-12} s). With increasing current, the modes are shifted to shorter wavelengths by 50–60 Å at 77 K. The maximum mode shift of 104 Å (10 cm^{-1}) is observed at 62 K. The spectral line width of the laser is as narrow as 10 MHz. Abnormally narrow directional patterns in the *p*–*n* junction plane are observed in some cases in the spatial distribution of laser emission. The current tuning of lasers, due to nonlinear optical effects, has been modeled mathematically in good agreement with the experiment. Transmittance spectra of OCS, NH_3, H_2O, CH_3Cl, and N_2O gases were recorded using current-tuned lasers. © *2001 MAIK "Nauka/Interperiodica".*

1. INTRODUCTION

The first part of the review [1] was concerned with investigations aimed at attaining the low threshold-current density and high limiting temperature of lasing. The present, second part discusses studies of the coherent emission itself from the standpoint of the possible application of lasers fabricated by the authors in high-resolution spectroscopy. The following problems were addressed:

(i) obtaining single-mode lasing in a single longitudinal spatial mode;

(ii) study of the spatial distribution of laser emission;

(iii) tuning of the laser wavelength by means of current and temperature;

(iv) measurement of the spectral line width;

(v) application of the lasers in high-resolution spectroscopy.

2. LASER DIODES

Details of the laser fabrication technique were reported in [1]. InAsSb/InAsSbP lasers were fabricated by means of LPE on (100)InAs substrates doped with Zn to a free carrier density of $\sim 5 \times 10^{18}$ cm^{-3}. The *n*-type active region was nominally undoped and had an electron concentration of $(1–4) \times 10^{16}$ cm^{-3}. The *n*- and *p*-type InAsSbP confinement layers were doped to $(3–5) \times 10^{18}$ cm^{-3} and $(1–2) \times 10^{18}$ cm^{-3}, respectively. The thickness of the active region and confinement layers was (0.5–3) and (2–3) μm, respectively. The laser design was based on a double heterostructure (DHS).

The lasers under study emit in the spectral range λ = 3–4 μm. The emission wavelength λ depends on the cavity length *L*. Figure 1 shows how λ grows with cavity length [2]. As is seen, the λ(*L*) dependence is linear in a wide range of cavity lengths (200–800 μm). The sharp drop in the wavelength at small *L* (*L* < 200 μm), typical of quantum-confinement lasers, results from gain leveling-off [3]. As already noted in [1], it may be assumed that the coherent emission of these lasers results from carrier recombination in quantum-size wells at one of the interfaces of the structure. With increasing *L*, the inter-mode distance Δλ decreases as $\Delta\lambda = \lambda^2/2Ln^*$, where n^* is the refractive index of the

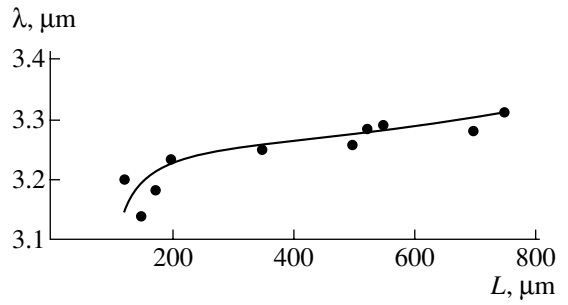

Fig. 1. Coherent emission wavelength λ vs. cavity length *L* at *T* = 77 K.

[1] See [1].

cavity, and, therefore, the number of modes in long-cavity lasers is greater.

Let us now consider laser tuning by varying first the temperature and then the driving current.

3. TEMPERATURE TUNING OF LASER EMISSION SPECTRUM

Temperature variation is the most obvious external factor capable of shifting a spectral mode. The temperature dependence of the spontaneous emission spectrum is due to a decrease in the band gap with increasing temperature and the resulting shift of the gain spectrum to longer wavelengths, as well as its broadening. Lasing modes correspond to cavity frequencies and are shifted due to temperature variation of the refractive index and cavity length.

In [2], the temperature tuning of the emission spectrum was studied in DHS lasers with a 60-μm-wide stripe and a ~350-μm-long cavity. The band diagram of these lasers is presented in Fig. 2a. For studying the temperature dependence, the lasers driven with current pulses of > 300-μs width exhibited, at $T = 77$ K, single-mode operation near the threshold current I_{th} (Fig. 2b). Commonly, lasing occurs at the peak of the spontaneous-emission band. Figure 2c shows that the intensity of radiation passed through an external Fabry–Pérot interferometer varies with time by the sine law. The mode is stable during the current pulse, with the mode wavelength changing by 0.5–1.0 cm^{-1} to smaller wave numbers ν, owing to active region heating. The wavelength grows virtually linearly with increasing temperature, $d\lambda/dT \approx 0.002$ μm/K. For the lasers under study, the estimated line width of coherent emission was 0.005 cm^{-1} [4].

When these lasers were used as components of an automated laser spectrometer [4], transmission spectra of methane and ethylene were recorded with a resolution of no worse than 0.005 cm^{-1}.

Thus, the temperature-tuned InAsSbP/InAsSb/InAsSbP lasers emitting at $\lambda = 3.2$–3.4 μm, fabricated and studied in our works, can be used in high resolution molecular spectroscopy. However, the tuning of lasers by means of current is more promising owing to its faster speed and wider spectral range. The following section presents the results obtained in our studies of how the spectral characteristics of our lasers depend on current.

4. TUNING OF LASER EMISSION SPECTRUM BY MEANS OF CURRENT

4.1. General Concepts

The tuning of the laser emission spectrum by current is enabled by the optical nonlinearity of the semiconductor medium; in particular, by nonlinear refraction, i.e., the dependence of the refractive index in the laser's active region, n, on the emission intensity (F) and free carrier concentration (N). The free carrier concentration

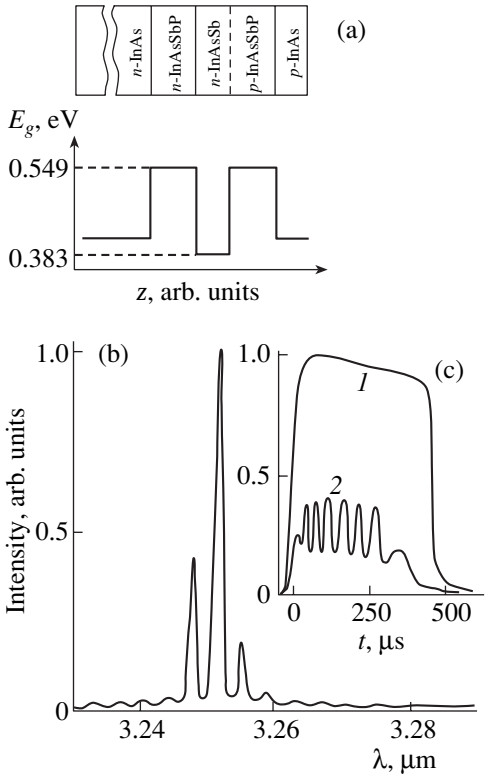

Fig. 2. (a) Laser structure and layer-by-layer profile of the band gap E_g; (b) laser emission spectrum at $T = 77$ K; (c) oscillograms of laser emission passed through (*1*) air and (*2*) Fabry–Pérot cavity. Starting temperature 80 K.

is, in its turn, affected by the emission intensity. This fact is well known [5]. The effect of free carriers on the refractive index has been taken into account from the theory of the semiconductor laser [6, 7]. It has been observed that, in the case of superluminescence, the longitudinal mode frequencies in a planar GaAs cavity are shifted steadily with increasing driving current [5]. This shift is opposite in sign to the temperature effect. The $n(N)$ dependence is stronger in narrower gap compounds, like InAs and InSb, compared with GaAs. The variation of the refractive index with the concentration of induced carriers in an $InAs_{1-x}Sb_x$ solid solution was calculated theoretically by Paskov [8]. The dispersion of Δn at the band gap edge was calculated for carrier densities of 10^{15}–10^{18} cm^{-3} at room temperature. However, lasers emitting in the 3–4 μm range usually operate at lower temperatures. We related the variation of the refractive index to that of the absorption coefficient by the following simplified formula

$$\frac{dn_\alpha}{dN} \approx \frac{(2/3 + kT/F_i)c\alpha_i}{3N_i\pi\omega}B, \qquad (1)$$

where F_i is the Fermi level position in the conduction band, N_i is the electron concentration on reaching the population inversion, c is the speed of light in vacuum, α_i is the refractive index in undoped unexcited material

of the active region at $\hbar\omega = E_g + F_i$, ω is the angular frequency, and E_g is the band gap. The coefficient B, equal to about 1.15, takes into account band gap narrowing with increasing nonequilibrium carrier density, as well as the influence of some simplifications. Plasma oscillations and other effects raise the overall dn/dN value by an additional 15%. At $T = 77$ K, $dn/dN \approx 0.3 \times 10^{-18}$ cm^3 and decreases nearly hyperbolically with increasing temperature.

The tuning of spectra by current is, to some extent, observed in any 3–4 μm laser, but experimental studies of this effect have not been reported yet.

To elucidate the physical mechanisms of laser tuning by current, we investigated, along with the tuning itself, dependences of the spatial distribution of emission on current (Section 4.2) and the effect of current on single-mode lasing characteristics (Section 4.3).

4.2. Dependence of the Spatial Distribution of Laser Emission (Spatial Oscillations) on Current

The spatial distribution of emission depends on the geometrical characteristics of a laser. We studied lasers with a stripe width of 10–13, 18–20, and ~40 μm. Commonly, the cavity length was chosen as optimal for the threshold current (225–350 μm). The dependence of the directional pattern on cavity length was studied at L = 125–2000 μm. At currents close to the threshold value [9] and stripe width of < 13 μm, only the longitudinal spatial mode is generated, with its contour in good agreement with calculations for the cosine distribution of the magnitude of the electromagnetic wave vector **E** at the output mirror of the cavity. The calculation was made using the following simplified formula

$$F(\theta) = \left[\frac{\cos a}{1-(2\alpha/\pi)^2}\right]^2, \quad \alpha = \frac{\pi b}{\lambda}\sin\theta, \qquad (2)$$

where θ is the emission detection angle, λ is the emission wavelength, and b is the stripe width.

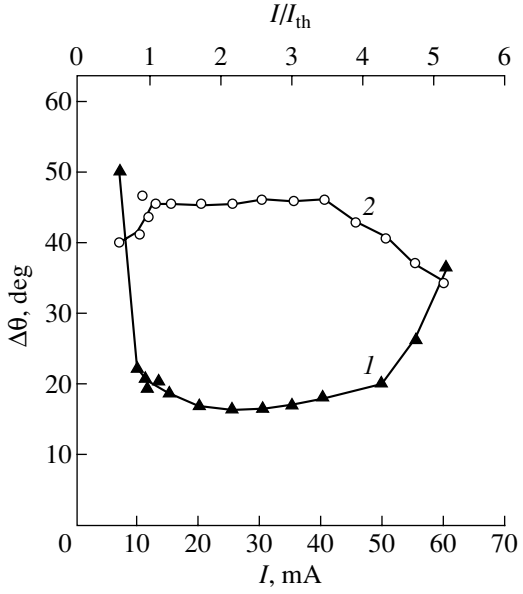

Fig. 3. FWHM of directional pattern, Δθ, vs. current I (*1*) in the *p–n* junction plane and (*2*) in the plane perpendicular to the *p–n* junction plane. V12192-1 laser.

At a stripe width of 18–20 μm and a driving current close to the threshold value, a single longitudinal mode is generated in some lasers, but, more frequent, the superposition of the longitudinal mode and a first-order transverse mode is observed. For the first-order transverse mode, the angular distribution of intensity was calculated at a sine distribution of the magnitude of the light wave vector **E**, using the relation

$$F(\theta) \approx \left[\frac{\sin\alpha}{1-(\alpha/\pi)^2}\right]^2. \qquad (3)$$

Some of the lasers with an 18- to 20-μm-wide stripe demonstrated a directional pattern with two peaks; the angular distance between these was ~11°, whereas for the first transverse spatial mode it should be ~20°.

For lasers with an ~40-μm-wide stripe, second-order transverse modes were observed. The $F(\theta)$dependence was calculated for the second-order transverse mode using the formula

$$F(\theta) \approx \left[\frac{\sin\pi[3/2 - ab/\lambda]}{\pi(3/2 - ab/\lambda)} + \frac{\sin\pi(2/3 - ab/\lambda)}{\pi(3/2 + ab/\lambda)}\right]^2. \qquad (4)$$

In the plane perpendicular to the *p–n* junction plane, no structure was observed in the directional pattern. In this region, the beam divergence is defined by the diffraction on the slit, the active region being about 1 μm thick. The study of the spatial distribution of emission in relation to L demonstrated that the directional pattern both in the *p–n* junction plane and in a plane perpendicular to it becomes narrower with increasing L. For example, with L growing from 150 to 2000 μm, the full width at half-maximum (FWHM) of the directional pattern (Δθ) decreases from 28.18° to 6° in the *p–n* junction plane, and from 83° to 40° in the perpendicular plane. It was assumed that the narrowing of the directional pattern with increasing L may be a consequence of the collimator action of the long cavity.

The dependences of the directional pattern on current were measured for the same groups of stripes. Figure 3 shows Δθ(I) in the *p–n* junction plane (curve *1*) and in the perpendicular plane (curve *2*) for the narrowest stripes (b = 10 μm, L = 225 μm, I_{th} = 12 mA at 77 K, V12192-1 laser) [10]. At currents smaller than the threshold value, Δθ in the *p–n* junction plane decreases rapidly from 50° to 20° with increasing current, owing to the growing share of the stimulated emission. As already mentioned, Δθ corresponds near the threshold to the $F(\theta)$ dependence (2) with a cosine distribution of the **E** vector at the output mirror of the cavity. Δθ reaches its minimum value of ~17° at currents of (2–2.5)I_{th}. In

this case, $F(\theta)$ cannot be described by formula (2). In all likelihood, the distribution of the **E** vector across the beam width ceases to be cosine in this range of currents and becomes nearly uniform. This is possibly the result of the fact that the contribution of the surface recombination diminishes with increasing current, and the injection density at the stripe edges grows to a greater extent than that at the center. For the uniform distribution of **E**, the theoretical curve is calculated using the formula

$$F(\theta) \approx \left[\frac{\sin\alpha}{\alpha}\right]^2. \quad (5)$$

However, the uniform distribution of the electric vector of the light wave at the output mirror of the cavity is impossible since the wave amplitude at the stripe edge must be virtually zero owing to the great difference between the refractive indices of crystal and air. Moreover, the amplitude cannot change stepwise with the coordinate. Therefore, the question of beam broadening with increasing current in narrow-stripe lasers has remained open. With the current increasing further, the directional pattern broadens. This may occur as a result of light beam narrowing because of the strong lateral optical confinement caused by an increase in the density of nonequilibrium carriers at the stripe edges and its decrease in the middle of a stripe. The rise in carrier concentration leads to a decrease in the refractive index. If the refractive index at the stripe edges decreases by more than $(\lambda/2b)^2$, then lateral optical confinement arising within the stripe makes narrower the light beam in the *p–n* junction plane. For the laser in question, the narrowing of the light beam in the *p–n* junction plane was estimated to be about 2 μm at a current $I = 4.65I_{th}$. In the perpendicular plane, the light beam broadens at currents $I > 3.55I_{th}$, owing to its penetration into the wide-band-gap regions, which leads to a narrower directional pattern. For narrow-stripe ($b \approx 10$ μm) lasers, the directional pattern varies with current as a result of variation of the longitudinal mode half-width, which is defined by the distribution of the electric vector of the light wave at the output mirror of the cavity. At the same time, for wider-stripe lasers, the structure of the spatial distribution of emission changes with increasing current. In lasers with an 18–20-μm-wide stripe, exhibiting a single longitudinal mode at currents near the threshold, the mode was split in two with increasing current. If the directional pattern at a near-threshold current has two peaks at an angular distance smaller than that observed for the first transverse mode, then the depth of the dip between the peaks decreases with increasing current (Fig. 4), with the angular position of the peaks hardly changing [11]. For lasers with a 40-μm-wide stripe and a 3-μm-thick active region, the directional pattern is single-lobed, with a narrow peak and broadened base, over the entire range of currents [12]. As stated above, at currents near the threshold ($I/I_{th} = 1.2$), $\Delta\theta \approx 23°$, and the directional pattern peak

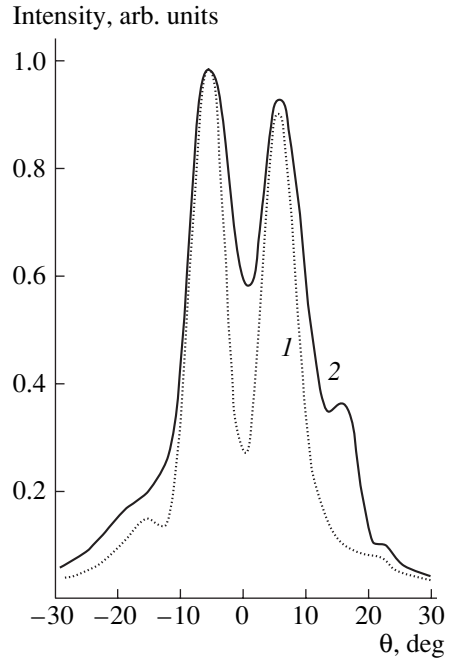

Fig. 4. Directional pattern in the *p–n* junction plane of V1109-3-39 laser at different excesses of current *I* over the threshold I_{th}, I/I_{th}: (*1*) 1.14 and (*2*) 1.8.

is pointed. The lobe becomes narrower with increasing current. For example, $\Delta\theta \approx 9°$ at $I/I_{th} = 1.44$, and the directional pattern peak becomes even more pointed (Fig. 5). In the plane perpendicular to the *p–n* junction plane, $\Delta\theta \approx 63°$, which is close to the value given by the relation $\Delta\theta = \lambda/d$, where *d* is the active region thickness.

The existence of unusual directional patterns of emission from lasers with different stripe widths shows that a new approach to laser beam formation and investigations of the near- and far-field distributions of the emission is required.

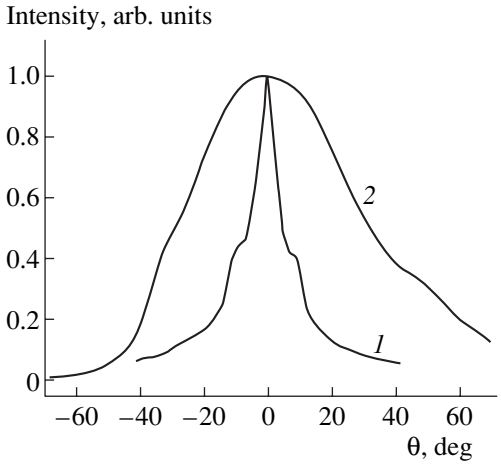

Fig. 5. Directional pattern of laser emission (*1*) in the *p–n* junction plane and (*2*) in the perpendicular plane. Current $I/I_{th} = 1.44$, $T = 77$ K, V1109-1-15 laser.

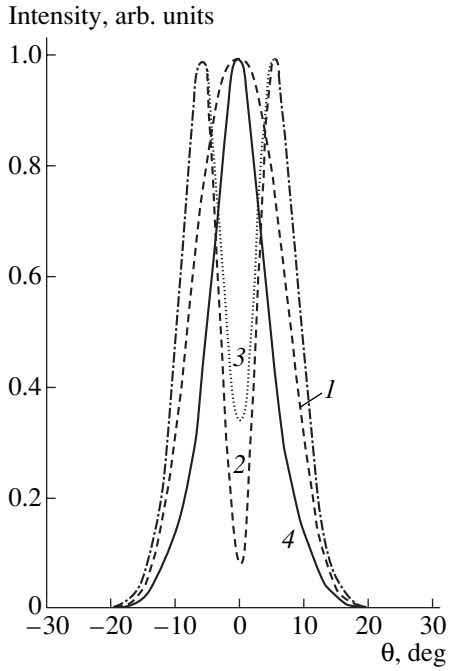

Fig. 6. Directional patterns of laser emission in the *p–n* junction plane for different combinations of beams of spatial oscillations: (*1*) single beam, (*2*) two antiphase beams with equal light wave amplitudes, (*3*) two antiphase beams with light wave amplitudes differing by a factor of 2, and (*4*) two in-phase beams with equal light wave amplitudes.

Our calculations are based on the assumption that the laser waveguide is a nonlinear optical medium. The constant of electromagnetic wave propagation averaged over the cavity length $\bar{\varepsilon}$ is quadratic in the electromagnetic wave amplitude owing to the approximately quadratic increase in the current density toward the mesa structure edges. This was shown by calculations [13] made by the method of conformal transformations, $w = \sin z$, for a finite stripe width (~16 μm) substantially smaller than the substrate width (~500 μm). The solution is valid when the substrate resistance exceeds the differential resistance of the *p–n* junction, which only happens in lasing. The injection at the stripe edges exceeds that in the middle of the stripe only in the case of lasing, when the relative excess of the injection density above the threshold $i = (G\tau - N_{th})/(N_{th} - N_0)$ (here $G\tau$ is the density of the nonequilibrium carrier injection; N_{th} and N_0 are the nonequilibrium carrier densities at, respectively, the generation and inversion thresholds) depends on coordinate y across the stripe width as

$$i \approx i_0\left[1 + k\left(\frac{2y}{b}\right)^2\right], \tag{6}$$

where i_0 is the injection density in the middle of the stripe, b is the stripe width, and $k = (c/2h)$ is the coefficient depending on the ratio of the substrate width (c) to its thickness (h) and equal to $k \approx 1.5$ for our lasers. Such a k value gives a ratio between the current densities at the edges and in the middle of the stripe of ~2.5. If we assume that multiple spatial modes are generated, and, therefore, the emission intensity becomes nearly uniform across the stripe width and is determined by the injection in its middle, i_0, then, at negligible charge spreading in the active region, the Helmholtz wave equation is reduced to the equation of a linear harmonic oscillator [13]

$$-\left(\frac{\lambda}{2\pi}\right)^2\frac{d^2u}{dy^2} + \frac{1}{2}2(-\delta\varepsilon_0)\frac{i_0}{1+i_0}k\left(\frac{2}{b}\right)^2 y^2 u = (\varepsilon_{th} - \bar{\varepsilon})u, \tag{7}$$

where $\delta\varepsilon_0$ is the change in the dielectric constant on raising the excitation level from the inversion threshold to the lasing threshold, and ε_{th} is the dielectric constant at the lasing threshold. A solution to this equation can be described in the form of eigenfunctions. The integers in each of these define the order of the transverse mode.

Therefore, under the adopted conditions, a laser beam can theoretically oscillate within the cavity as a single light beam. The general solution to the Schrödinger equation for a linear harmonic oscillator is a minimized wave packet oscillating around the origin of coordinates at the center of the stripe. It is worth noting that the obtained solution is valid for currents that ensure wave localization through an increase in the carrier density at the stripe edges with increasing current. The minimum stripe width necessary to confine the wave to our structures is evaluated to be 9 μm [13]. The linearity of the differential equation describing the oscillating beam allows for its summation with another beam having a different phase and amplitude. Figure 6 presents calculated [11] directional patterns of laser emission in the *p–n* junction plane for a single oscillating beam, two antiphase oscillating beams with equal light wave amplitudes, two antiphase oscillating beams with light wave amplitudes differing by a factor of 2, and two in-phase oscillating beams with equal light wave amplitudes. A time-dependent distribution of the light wave at the cavity mirror was considered. To obtain the averaged distribution, integration over time is necessary. As seen in Fig. 6, a single beam (curve *1*) and two in-phase beams (curve *4*) give a single-lobed directional pattern. For the case of two beams, the lobe half-width is 1.7 times less than that for a single beam. Antiphase beams (curves *2* and *3*) form a double-lobed directional pattern, with a dip at $\theta = 0$. The depth of the dip decreases with increasing difference between the light wave amplitudes of the beams.

For a laser with a 10-μm-wide stripe at currents exceeding the threshold by a factor of 2.0–2.5, the single-lobed directional pattern is similar in shape and half-width with that calculated for the case of two in-phase beams. The second beam favors narrowing of the directional pattern and decreases the half-width of the intensity distribution at the cavity mirror, which makes

this situation the most probable in narrow cavities. The double-lobed experimental directional pattern of a laser with an 18-μm-wide stripe is similar in shape and angular distance between the two peaks to the directional pattern for the case of two antiphase beams. The depth of the dip at the center of the experimental curve corresponds to a 2–3-fold difference between the light wave amplitudes of the antiphase oscillating beams [11]. The experimental directional pattern obtained for lasers with a 40-μm-wide stripe is consistent with that calculated on the assumption of two in-phase beams, but with account taken of the existence of the second-order spatial modes in the cavity of the laser with a wide stripe [12]. Figure 7 shows calculated directional patterns in the *p–n* junction plane of a laser with a 40-μm-wide stripe for the case of beams with equal light wave amplitudes and dependence of the refractive index on a coordinate identical to that reported in [13]. Curve *1* corresponds to a radiation beam whose center of gravity is shifted from the center of the stripe to the coordinate of the first transverse mode. Curves *2* and *3* correspond to beams oscillating between the extreme maxima of the second and third transverse modes, respectively. The experimental directional pattern is quite consistent with the calculated curve *2*, in accordance with the fact that the second-order transverse mode is observed in lasers with a 40-μm-wide stripe in the case of a single light beam propagation [9]. Side wings appear in the directional pattern of wide-stripe lasers, but their intensity is low.

Thus, all the anomalous experimental directional patterns can be accounted for in terms of spatial light beam oscillations in the laser cavity; this may be either a single light beam, or a sum of two beams, in-phase or antiphase, with equal or different light wave amplitudes. These theoretical conclusions were arrived at with account taken of the increase in the nonequilibrium carrier density from the middle of the laser stripe toward its edges and the corresponding decrease in the dielectric constant due to the increase in this direction of the injection density and a decrease in the emission intensity.

4.3. Study of Single-Mode Operation in Relation to Current

Let us now discuss how the single-mode operation of our lasers depends on current [14–18]. We have determined the temperature and current ranges in which the emission is single-mode.

Single-mode lasing may be accidental, occurring in a situation when the amount of crystal defects in antinodes of emission of one of the modes is lower than that in antinodes of other modes. However, single-mode operation has its specific features. The principal condition for single-mode lasing is that the spectral positions of the modes and the gain spectrum shift with current in the same way. The photon energy of the emission mode $h\nu_L$ changes with the nonequilibrium carrier density mainly owing to a variation in the refractive index n:

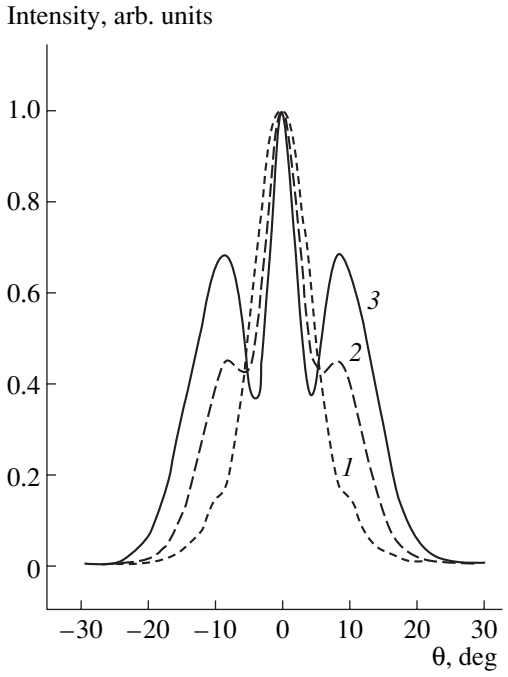

Fig. 7. Directional patterns in the *p–n* junction plane for two in-phase beams with equal light wave amplitudes calculated using formulas from [11]; deviation of beams from the stripe center: (*1*) 5, (*2*) 8, and (*3*) 10 μm.

$$\frac{dh\nu_L}{dN} = \frac{E_g}{n}\frac{dn}{dN}. \quad (8)$$

According to [16], the photon energy in the gain spectrum peak ($h\nu_m$) obeys the relation

$$\frac{dh\nu_m}{dN} = \frac{1}{N_{\text{th}}}\left(\frac{2}{9}F_{\text{th}} + \frac{1}{9}kT + \frac{1}{6}\Delta E_g\right), \quad (9)$$

where F_{th} and N_{th} are the quasi-Fermi level position in the conduction band and the electron density at the lasing threshold, respectively; ΔE_g is the band gap narrowing under injection, related to the nonequilibrium carrier density by $\Delta E_g \sim N^{1/6}$.

According to (9), the magnitude and sign of $dh\nu_m/dN$ at a given temperature is defined by the relation between F_{th} and ΔE_g (at T = const), with $\Delta E_g > 0$. In the semiconductor of the active region of the lasers under study, the effective electron mass is small compared with the hole mass, with the result that $|F_{th}| > |\Delta E_g|$, and, therefore, $dh\nu_m/dN > 0$. The opposite sign can also be obtained in a mechanically strained active region. Hence, the magnitude and the sign of $dh\nu_m/dN$ can be controlled by means of internal mechanical stresses. In the unstrained laser structures under study, $|\Delta E_g| < F_{th}$, $\Delta E_g < 0$, and $dn/dN < 0$. The derivatives $dh\nu_m/dN$ and $dh\nu_L/dN$ are positive.

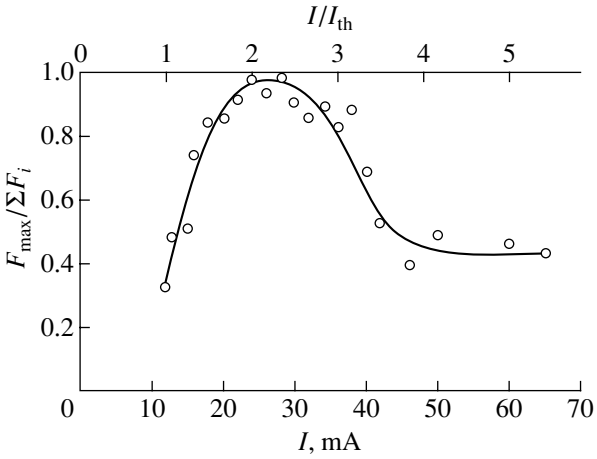

Fig. 8. Dominant mode to overall emission intensity ratio $F_{max}/\sum F_i$ vs. current I.

In the single-mode lasers, the nearest neighbors of the emission mode are suppressed. In [19], the suppression of modes was ascribed to scattering on electron density waves occurring in a range of photon energies that is significantly narrower than the inter-mode distances, and, therefore, this is probably not the principal factor. We have shown that taking into account the photon momentum yields a significantly wider range of suppression [20]. The photon momentum makes the radiative transitions indirect. The energies of carriers involved in transitions become dependent on the angle between the photon and carrier momentum vectors. The time of carrier re-orientation via elastic scattering is 10^{-13} s. Consequently, a single laser mode reduces the carrier concentration in a rather wide range of energies, which define the depletion range. The modes in which carriers from this energy range might be involved are suppressed.

The photon momentum p_p was defined in [21] as

$$p_p = \frac{E_g n}{c}. \tag{10}$$

For our lasers, $p_p = 0.67 \times 10^{-22}$ (g cm)/s. For nearly orthogonal directions, when the carrier momentum magnitude remains unchanged in a transition, the electron momentum magnitude $k_{n0} = 4.18 \times 10^{-22}$ (g cm/s). The depletion range in the conduction band ΔE_n is given by

$$\Delta E_n \approx \frac{2k_{n0}p_p}{m_n + m_p}, \tag{11}$$

where m_n and m_p are the effective electron and hole masses, respectively. The widths of the depletion range are nearly equal in the valence and conduction bands, the allowed bands being close to spherical for the energies in question. The boundaries of the frequency suppression band are defined by the suppression in the valence band, because $m_n \ll m_p$. The long-wavelength edge was calculated as the photon energy

$$h\nu_{p-} \approx h\nu - \frac{2k_{n0}p_p}{m_n} + \frac{2p_p^2}{m_n}\frac{m_p}{m_n + m_p}. \tag{12}$$

The short-wavelength edge of the suppression band corresponds to the photon energy

$$h\nu_{p+} = h\nu + \frac{2k_{n0}p_p}{m_n} + \frac{2p_p^2}{m_n}\frac{m_p}{m_n + m_p}. \tag{13}$$

As can be seen from (12) and (13), $h\nu_{p+} - h\nu > h\nu - h\nu_{p-}$, i.e., the suppression range is wider on the short-wavelength side of the mode, compared with the long-wavelength side. Our estimates for the lasers under study are $h\nu_{p+} - h\nu = 1.77$ meV and $h\nu - h\nu_{p-} = 1.26$ meV. At the same time, the intermode distance is 0.5 meV. Thus, the suppression of neighboring modes, because of the presence of the photon momentum, extends to three and two inter-mode intervals on the short- and long-wavelength sides of the generated mode, respectively. The modes immediately adjacent to the principal mode are suppressed to the greatest extent, because the depletion range in the valence band is involved in their generation to a greater extent than that of distant modes. The depletion range in the conduction band yields a suppression range that is narrower than the inter-mode distance and, therefore, not involved in the suppression of neighboring modes. Transverse spatial modes and the corresponding frequency modes are suppressed in lasers with a tapered waveguide appearing as a result of an increase in the injection density across the cavity width from its center to its edges, low emission intensity at the edges, and weak spreading of carriers across the active region. In the course of the spatial oscillations discussed above, the light beam moves from one edge to the other through the center with lowered gain and changes the gain spectrum, which maintains the arising oscillations; i.e., the beam oscillations are self-sustaining.

Figure 8 presents one of the experimental light–current characteristics for the single-mode operation of a laser with $b = 10$ μm, $L = 225$ μm, and $I_{th} = 12$ mA (V12192-1 laser) at 77 K [14]. The fraction of the dominant mode in the overall emission of all the spectral modes ($F_{max}/\sum F_i$) was measured at various currents. As is seen, the $F_{max}/\sum F_i$ ratio is current-dependent and varies between 0.8 and ~1 in the range of currents $I/I_{th} = 1.5$–3. At $I = I_{th}F_{max}/\sum F_i \sim 0.3$. At high currents, $I/I_{th} > 3.5$, $F_{max}/\sum F_i$ is independent of current and equal to ~0.45. Single-mode lasing has been studied in relation to current and temperature for a V12191 laser with a 16-μm-wide stripe and a 375-μm-long cavity [16]. The operation was single-mode at currents

exceeding the threshold value by 10 to 200–300% in the temperature range T = 12–90 K.

4.4. Fast Tuning of Laser Emission Wavelength by Current

Let us consider the tuning of our lasers by current. The variation of the emission wavelength is defined by the variation of the constant of electromagnetic wave propagation along the stripe ($\bar{\varepsilon}$), characterizing the velocity of the laser emission propagation along the stripe and having a value intermediate between the dielectric constant at the stripe edge and at its center. The variation of $\Delta\lambda$ is related to that of $\bar{\varepsilon}$ ($\Delta\bar{\varepsilon}$) by

$$\Delta\lambda = \frac{\lambda}{2\bar{\varepsilon}}\Delta\bar{\varepsilon}. \tag{14}$$

The nonequilibrium carrier density may significantly exceed the threshold value at the stripe edges, where the laser emission intensity is zero because the wave nodes are located here; consequently, only spontaneous recombination occurs at the stripe edges. Far from the edges, the carrier density may be even lower than the threshold value owing to the high rate of stimulated recombination. Therefore, the dielectric constant decreases toward the stripe edges in an operating laser. The higher the injection uniformity, the stronger is this effect and the weaker is the carrier spreading over the *p*–*n* junction area.

As shown in [5], self-focusing is due to the dependence of the dielectric constant ε on the electromagnetic wave amplitude. This is associated with the nonlinearity of the laser's optical medium. However, dependence of ε on current has not been revealed. We considered a mathematical model for lasers in which the current density is the same over the area and in which no spreading occurs; i.e., the injection is uniform. With account taken of the dependence of the dielectric constant on the nonequilibrium carrier density and the assumed time-independent densities of nonequilibrium carriers and photons, the Helmholtz wave equation takes the form

$$\frac{d^2u}{dy^2} + \left(\frac{2\pi}{\lambda}\right)^2(\varepsilon_i - \bar{\varepsilon})u + \left(\frac{2\pi}{\lambda}\right)^2\delta\varepsilon_0\frac{i+1}{1+u^2/D}u = 0, \tag{15}$$

where u is the electromagnetic wave amplitude; ε_i is the dielectric constant at the inversion threshold; i is the relative excess of current over the threshold; $D = h\omega 8\pi/b\tau n^2$; β is the differential gain; τ is the lifetime of nonequilibrium carriers; $\delta\varepsilon_0 = 2n(dn/dN)(N_{th} - N_0)$; n is the refractive index of the active medium; and N_{th} and N_0 are the carrier densities at the lasing and inversion thresholds, respectively. The variation of $\bar{\varepsilon}$ leads to changes in the emission wavelength (14). It is worth noting that, in contrast to Eq. (7.4) from [5], Eq. (15) includes the quantity i in its third term. Since $\bar{\varepsilon}$ depends on u^2, Eq. (15) reflects the nonlinearity of the laser's optical medium.

The existence of the inflection point in the $U = f(y)$ curve makes it possible to express, in accordance with Eq. (15), $\bar{\varepsilon}$ in terms of the wave amplitude U_1 at this point:

$$\bar{\varepsilon} = \varepsilon_i + \delta\varepsilon_0\frac{i+1}{1+u_1^2/D}. \tag{16}$$

It follows from this relation that at $i \ll 1$ and $u_i^2/D \ll 1$ the inequality $\bar{\varepsilon} < \varepsilon_{th}$ holds, where $\varepsilon_{th} = \varepsilon_i + \delta\varepsilon_0$ and $\delta\varepsilon_0 < 0$. The value of $\bar{\varepsilon}$ decreases sublinearly with increasing i. In this case, the wavelength of our lasers decreases by $\delta\lambda_- \approx 4.5$ Å. At $i \gg 1$, when $u_i^2/D > 1$, the emission self-focusing results in $\bar{\varepsilon} > \varepsilon_{th}$ and grows with increasing current i. These two portions of the $\bar{\varepsilon}(i)$ dependence must be connected by a smooth curve with a positive derivative. The increase in λ can only be observed in lasers with a wide (20 μm) stripe, in which emission self-focusing occurs, with $\Delta\lambda_+$ exceeding $|\Delta\lambda_-|$ severalfold.

If the injection is not uniform [13] (the stripe is much narrower than the substrate, b = 16 μm, and c = 500 μm), the excess of the injection density over the threshold of i depends on the coordinate across the stripe width y as (6), and the wave equation takes the form (7); i.e., the light beam in the crystal oscillates, then the constant of the electromagnetic wave propagation along the cavity, $\bar{\varepsilon}$, depends on the quantum number n on i_0 and, consequently, on current:

$$\bar{\varepsilon}_n = \varepsilon_{th} - \left(n + \frac{1}{2}\right)\frac{2\lambda}{\pi b}\sqrt{(-\delta\varepsilon_0)\frac{i_0 k}{1+i_0}}. \tag{17}$$

The propagation constant $\bar{\varepsilon}_n$ decreases sublinearly with increasing current and gradually levels off. The maximum decrease in the wave packet propagation constant with i_0 increasing from 0 to ∞ is estimated for our lasers to be $\Delta\varepsilon_{max} = 0.032$. The calculated maximum decrease in wavelength, owing to the nonuniform inflow of current into the stripe from the substrate, is estimated to be $\Delta\lambda_{max} = 41$ Å for our lasers.

To evaluate the speed of current tuning, it is necessary to keep in mind that the dielectric constant depends on the density of nonequilibrium carriers, which, in turn, is defined by the rates of stimulated and spontaneous recombination. The influence of the spontaneous recombination is due to the fact that the carrier density grows to a greater extent at the stripe edges than it decreases at the center. This is the main reason for the enhancement of spontaneous emission with increasing current above the threshold. In fact, the above-threshold

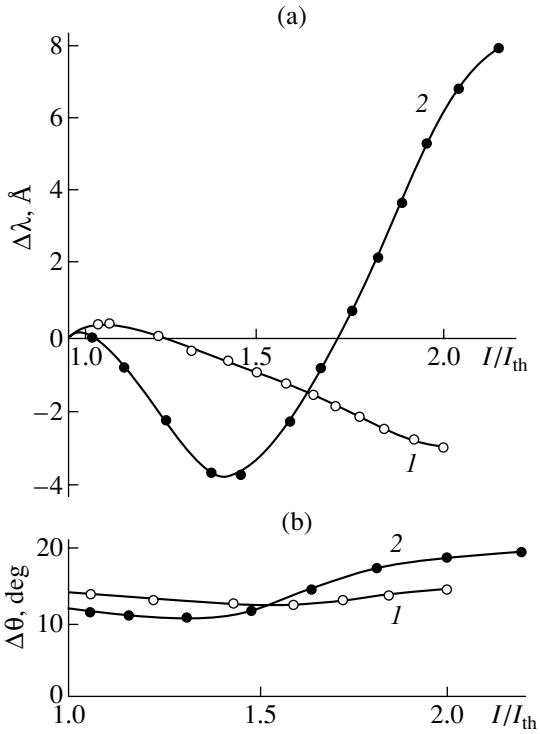

Fig. 9. (a) Variation of the laser emission wavelength $\Delta\lambda$ and (b) variation of the directional pattern half-width $\Delta\theta$ vs. driving current to threshold current ratio I/I_{th} for lasers with stripe width: (*1*) 16 and (*2*) 20 μm.

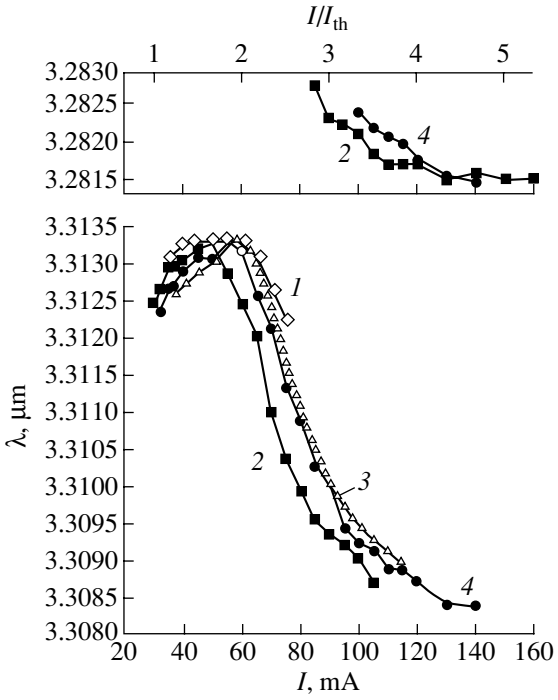

Fig. 10. Emission wavelength of V12152-71 laser vs. current for pumping with (*1*) direct current, (*2*) short pulses, (*3*) saw-tooth pulses, and (*4*) square-wave pulses.

rise in the carrier density is at least three times weaker than the below-threshold one. Consequently, the lasing wavelength is affected to a lesser extent by spontaneous recombination than by stimulated recombination. The photon lifetime in the cavity is $\sim 10^{-12}$ s, and the carrier lifetime in the case of spontaneous recombination is $\sim 10^{-8}$ s. Presumably, the current tuning takes some intermediate time.

Let us consider experimental data on the tuning of our lasers by current.

Different driving modes were used: short pulses of 20–40 μs with the period-to-pulse duration ratio of 100, square pulses with the period-to-pulse duration ratio of 2 and a repetition frequency of 36–80 Hz, direct current, and direct current with a saw-tooth component added [22, 23]. In the last case, the direct current was set equal to the threshold current. The frequency of the saw-tooth component was in the range from 10^2 to 10^4 Hz. With the laser driven by saw-tooth pulses, the coherent emission leaving the laser was passed through an external Fabry–Pérot resonator, fabricated from a 47-mm-thick silicon plate that served as the amplitude-frequency discriminator. Further, the optical signal was passed through a monochromator, detected with an InSb photodiode, and amplified by a differential amplifier with a response time of 0.2 μs. A laser wavelength resolution of 2×10^{-2} Å was achieved by turning the silicon Fabry–Pérot resonator to change its length. The spectra were recorded with a DMR-2 monochromator as the dispersing instrument. The measurements were taken in the temperature range 12–92 K.

Experimental studies of our lasers have shown that the spectral modes of emission shift mainly to shorter wavelengths with increasing current. However, several lasers with a 20-μm-wide stripe exhibited a short-wavelength shift at currents near the threshold and a long-wavelength shift at currents of $(1.5–2)I_{th}$. The range of the long-wavelength shift was several times wider than that of the short-wavelength shift (Fig. 9a). The long-wavelength shift was accompanied by emission self-focusing manifested in the expansion of the directional pattern, caused by diffraction on the slit corresponding to the light beam width at the cavity mirror in the *p–n* junction plane (Fig. 9b). Such a dependence $\Delta\lambda(I)$ stems from the $\bar{\varepsilon}(i)$ dependence expressed by formula (16), derived for lasers with uniform injection and negligible charge spreading across the stripe width. For most of the lasers, a small long-wavelength shift was observed at small above-threshold currents, but a short-wavelength shift appeared with the further increase of current.

We studied coherent emission spectra with different types of driving current: direct current, short 0.04-ms pulses with a period-to-pulse duration ratio of 100, saw-tooth pulses with repetition frequencies of 10^2 to

10^4 Hz, and square pulses with a period-to-pulse duration ratio of 2 and a repetition frequency of 36 Hz [13]. The measurements were done at 77 K. The laser stripe width was 16 μm, and the substrates were 500 μm wide. The $\lambda(I)$ dependences behave similarly at different kinds of injection (Fig. 10). At low currents, a shift to longer wavelengths is observed by a value no less than 10 Å. At low currents, the emission is concentrated in a single longitudinal spatial mode. Nonequilibrium carriers at the center of the active region "burn out" under these conditions, and their density decreases somewhat. This increases the electromagnetic wave propagation constant. With the current increasing further, the spectral mode shifts smoothly to shorter wavelengths, this shift greatly exceeding the preceding long-wavelength shift. The maximum short-wavelength shift was ~50 Å. The experimentally obtained $\lambda(I)$ dependence qualitatively correlates with the theoretical $\bar{\varepsilon}(i)$ dependence for lasers with nonuniform injection over the stripe width, which is caused by a voltage drop in the substrate bulk [Eq. (17)]. The experimental $\Delta\lambda_{max}$ is 22% higher than the theoretical value. A possible reason for this is that not all modes of all orders are generated in our samples, but the longitudinal and first transverse modes are preferentially generated, which additionally increases the carrier density at the stripe edges. Taking this factor into account may give an increase in $\Delta\lambda_{max}$ by 30%. At high currents, $3I_{th}$, the slope of $\lambda(I)$ decreases, the spectrum ceases to be single-mode, and, at $I > 4I_{th}$, the wavelength becomes independent of current. This behavior of $\lambda(I)$ also follows from the theoretical dependence $\bar{\varepsilon}(i)$ (17). Modes with a wavelength shorter than that of the dominant mode, appearing at $I > I_{th}$, shift with current in the same manner as the dominant mode (Fig. 10). The strongest emission wavelength tuning to shorter-wavelengths was observed at the same currents where the transverse modes appear. The coincidence of the spectral characteristics for different types of injection indicates that the active region is not heated by current and that the current tuning is fast, as assumed in theory [24].

The tuning of narrow-stripe (10 μm) lasers with low (~12 mA) threshold current was studied. Experimental data are presented for a laser whose light–current characteristic in single-mode operation is shown in Fig. 8. The dominant mode wavelength, directional patterns in the plane of the *p–n* junction and in the perpendicular plane, and also the relative integral emission intensity were studied as functions of the driving current (Fig. 11) [14]. The lasers were driven with square pulses. In these lasers, the wavelength is shifted by current only to shorter-wavelengths but at different rates in different I/I_{th} ranges; the total mode shift with current was ~55 Å at an intermode distance of ~60 Å (Fig. 11a). There are four current ranges differing in the rate of the mode shift. Special attention was drawn to the fact that, for currents between $1.5I_{th}$ and $2.8I_{th}$ when the operation is single-mode, $F_{max}/\sum F_i$ lies within 0.8–1, and the total mode shift with current is ~2.5 Å. In this range of currents, the directional pattern width $\Delta\theta \sim 17°$. As already shown, such a narrow directional pattern may be due to

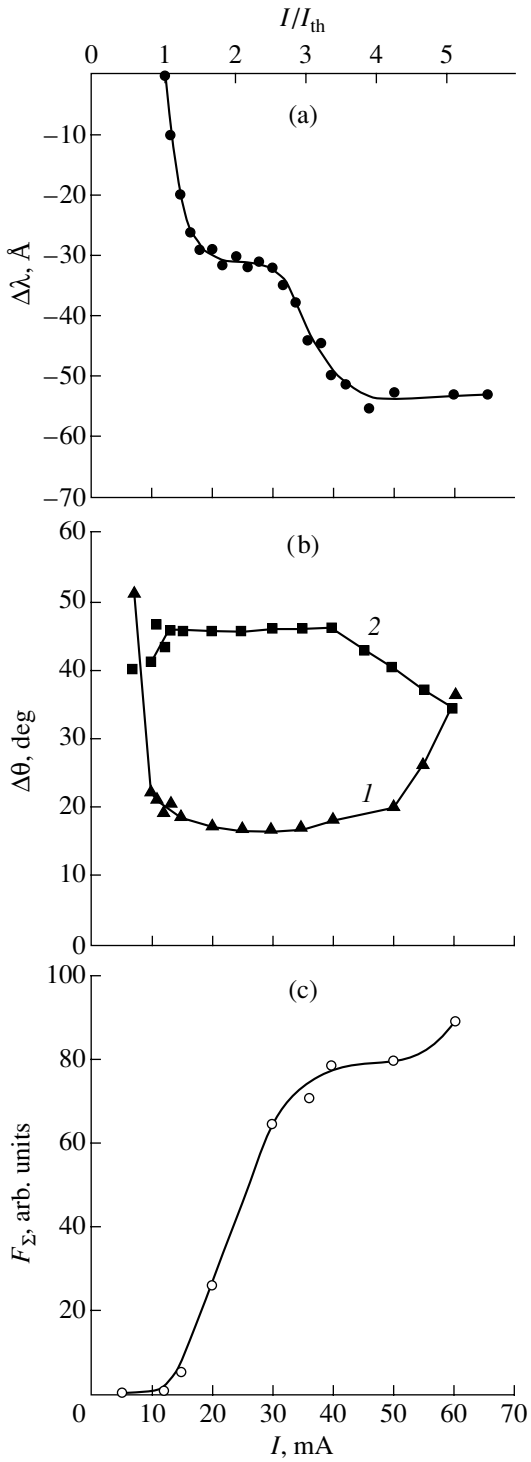

Fig. 11. (a) Spectral mode shift Δλ; (b) FWHM of directional pattern, Δθ, (*1*) in the *p–n* junction plane and (*2*) in the plane perpendicular to the *p–n* junction plane; and (c) integral emission intensity F_Σ vs. current. V12192-1 laser.

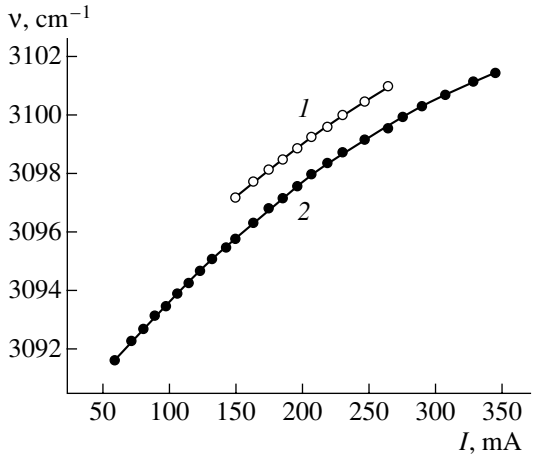

Fig. 12. Wave number of laser modes vs. driving current at laser temperature of (*1*) 77 and (*2*) 62 K.

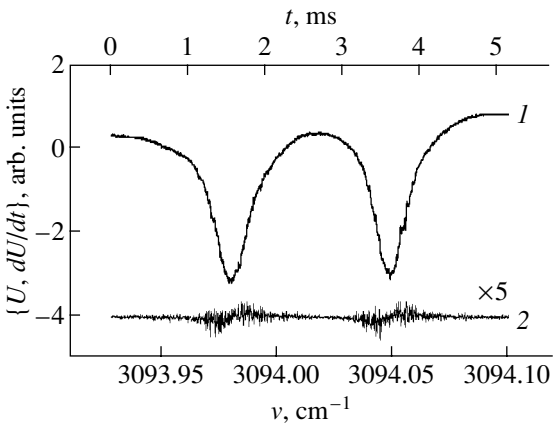

Fig. 13. (*1*) Oscillogram of signal *U* proportional to the intensity of laser emission transmitted through a cell with CH_3Cl gas at saw-tooth driving current and (*2*) its time derivative *dU*/*dt* obtained after the *RC*-circuit.

the superposition of two light beams with equal light wave amplitudes oscillating in-phase. Probably, the spectral characteristics are also defined by these oscillations. In the first range, between I_{th} and 1.5 I_{th}, the shift rate is the highest. The total mode shift is ~30 Å, and the emission is not purely single-mode, $F_{max}/\sum F_i$ being 0.3–0.8 (Fig. 9). The directional pattern narrows in the *p–n* junction plane and gets wider in the perpendicular plane. The integral emission intensity grows superlinearly with increasing current. Presumably, a single light beam oscillates in this current range. In the third range of currents, between $2.5I_{th}$ and $3.5I_{th}$, the mode strongly shifts again to shorter wavelengths (~20 Å). In this range, the single-mode operation is disrupted; $F_{max}/\sum F_i$ changes from 1 to 0.5. The directional pattern in the *p–n* junction plane broadens somewhat (Fig. 11b, curve *1*), and that in the perpendicular plane remains almost unchanged (Fig. 11b, curve *2*). In the fourth range of currents, the emission wavelength does not change with increasing current, which may be due to the leveling-off of the electromagnetic wave propagation constant $\bar{\varepsilon}$ as a function of current, in accordance with (17). The light beam in the *p–n* junction plane gets narrower, and that in the plane perpendicular to the *p–n*-junction plane broadens and penetrates into the confinement regions; this causes narrowing of the directional pattern in the perpendicular plane and decreases the integral emission intensity.

The temperature dependence of laser-mode current tuning was studied in [16, 18] for lasers with 16-μm-wide stripes and a 375-μm-long cavity and driven by square pulses at temperatures of 12–90 K. As stated above, the emission was single-mode in this temperature range. At 77 K, the modes shifted by ~60 Å to a shorter-wavelength, which, for this laser, constituted approximately two intermode distances. The laser emission was single-mode over the entire tuning range. The maximum shift of the spectral mode by current (10 cm^{-1}, 104 Å) was obtained at 62 K. Figure 12 presents the emission wave number as a function of current at 62 and 77 K [18]. At the boundaries of the temperature interval studied, the tuning range is half the maximal value.

The dependence of the laser emission spectrum on current was studied for lasers with a wider stripe (40 μm). The increase in the stripe width from 10–20 to 40 μm did not impair the spectral characteristics of the laser. The 24-Å shift of the wavelength with current at an intermode distance of 62 Å (V1109-1-15 laser) is the average value for InAsSb/InAsSbP heterostructure lasers with a stripe width of 10–20 μm.

4.5. Emission Line Width in Tunable Diode Lasers

In high-precision studies of vibration-rotational spectra of gas molecules, the spectral width of the emission line is the principal characteristic of lasers. The emission line width was studied in current-tuned InAsSbP/InAsSb/InAsSbP heterostructure lasers [25, 26]. The lasers were driven with direct current modulated by a saw-tooth current in the current range of I_{th} to $5I_{th}$ at temperatures of 12–100 K. The emission of a mode was directed into a cell filled with gas or into a reference cavity. The detected signal was fed into a differentiating *RC*-filter and a digital oscilloscope. Figure 13 shows the oscillogram of a laser emission signal transmitted through a cell with CH_3Cl (curve *1*) and the time derivative of this signal (curve *2*). The rate of variation with time, $\tau(\nu')$, of the emission wave number ν' of a laser driven with saw-tooth current was determined from the time interval between two signal minima corresponding to the known absorption lines of CH_3Cl. When separate absorption lines were used, the rate ν' was determined from natural frequencies of the reference cavity. The linear average of the derivative U_R and

its rms deviation $\langle U_\mu \rangle$ from the mean value were recorded by the second channel of the oscilloscope. These quantities were measured at the inflection points of the I curve, where they are at a maximum, and averaged. The half-width of the emission lines was found using the relation

$$\Delta f = 2c\tau\nu'\langle U_\mu \rangle / U_R. \quad (18)$$

The experimental emission line half-widths Δf depend on the driving current I (Fig. 14). The line half-width is the narrowest at some current $I = I_{\min}$. Δf increases steeply with current at $I > I_{\min}$ and gradually at $I_{\min} = (3–4)I_{\text{th}}$. In the described laser, Δf is within 32–18 MHz. In multimode lasers, the half-widths of several simultaneously generated modes differ by no more than 20%. At a temperature deviation of ±10 K from the optimal temperature, when the tuning range is the widest, the half-width of the emission line changes in the same direction as the absolute temperature (at a fixed $I - I_{\text{th}}$ difference).

Along with experimental points, Fig. 14 presents two theoretical curves (dashed and solid). The dashed line is plotted for a V12191-3 laser, using the formula derived by Henry [27] for the half-width of the semiconductor laser emission line

$$\Delta f = R(1 + \alpha_n^2)/4\pi P, \quad (19)$$

where R is the average rate of spontaneous emission, α_n is the ratio of variations of the real and imaginary parts of the refractive coefficient, and P is the number of photons in the cavity. Henry's theory assumes that the average density of nonequilibrium carriers N becomes current-independent after the threshold value N_{th} is achieved. In this case, R, α_n, and Δf are defined by the variation of the number of photons in the cavity P, and Δf is due to fluctuations of spontaneous emission into the mode, in agreement with the Schawlow–Tawnes theory [28]. A hyperbolic decrease in Δf with increasing $I - I_{\text{th}}$ has been observed experimentally [29]. In tunable lasers, the nonequilibrium carrier density grows with current. In this case, the emission line half-width is defined by fluctuations of the natural frequencies of the cavity, which arise from the fluctuation of the number of carriers inside it, with the corresponding variation of the refractive index.

In the absence of lasing, the probability function for the natural frequencies of the cavity has a width

$$\Delta f_0 = 2\frac{f}{\tau}\left|\frac{dn}{dN}\right|\sqrt{\frac{2}{V}(N_{\text{th}} + \delta N)}, \quad (20)$$

where V is the cavity volume, and δN is the excess of the nonequilibrium carrier density over the threshold value attributed to the deviation δf of the lasing frequency from its value at the threshold current,

$$\delta N = \frac{\delta f}{f}\frac{n}{(-dn/dN)}. \quad (21)$$

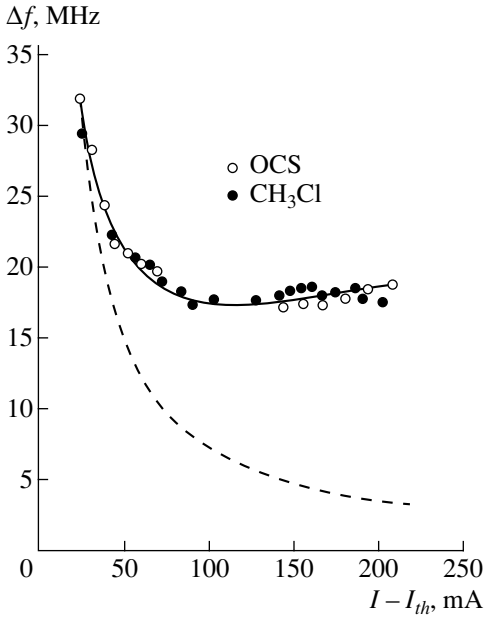

Fig. 14. *Points*: experimental laser line half-widths Δf vs. current, obtained with V12191-3 laser using the absorption lines of CH_3Cl and OCS gases; *curves*: theoretical dependences of Δf on current, calculated on the assumption of current-independent nonequilibrium carrier density (dashed line) or that increasing with current (solid line).

In the case of lasing, the probability function becomes narrower by a factor equal to the factor by which the carrier lifetime decreases (from τ_0 to τ_p). The emission line width is given by

$$\Delta f = \Delta f_0 \frac{\tau_p}{\tau_0}. \quad (22)$$

At a fixed injection rate and gain under the conditions of bimolecular recombination typical of lasers, we use the rate equation for N to obtain

$$\frac{\tau_0}{\tau_p} = 1 + \frac{(I/I_{\text{th}}) - (1 + \delta N/N_{\text{th}})^2}{2(1 - N_0/N_{\text{th}})(1 + \delta N/N_{\text{th}})}, \quad (23)$$

where N_0 is the nonequilibrium carrier density at the population inversion threshold for the mode in question, and $N_0/N_{\text{th}} = 0.75–0.80$. The solid curve in Fig. 14 represents Δf calculated using Eqs. (20)–(23) for $n = 3.6$, $dn/dN = 0.25 \times 10^{-18}$ cm^3, and $N_{\text{th}} = 9.4 \times 10^{16}$ cm^{-3}, which is in good agreement with experimental data. When the emission line width and its dependence on current are governed by fluctuations of the cavity's natural frequencies, arising from fluctuations of the number of carriers in it, the emission line width is inversely proportional to the square root of the active region volume. This fact allows us to depress the emission line width by making the cavity wider. An emission line half-width of 10 MHz was achieved in lasers with a 100-μm-wide cavity [26]. This linewidth is 15–50 times smaller than the width of absorption lines of gases. The

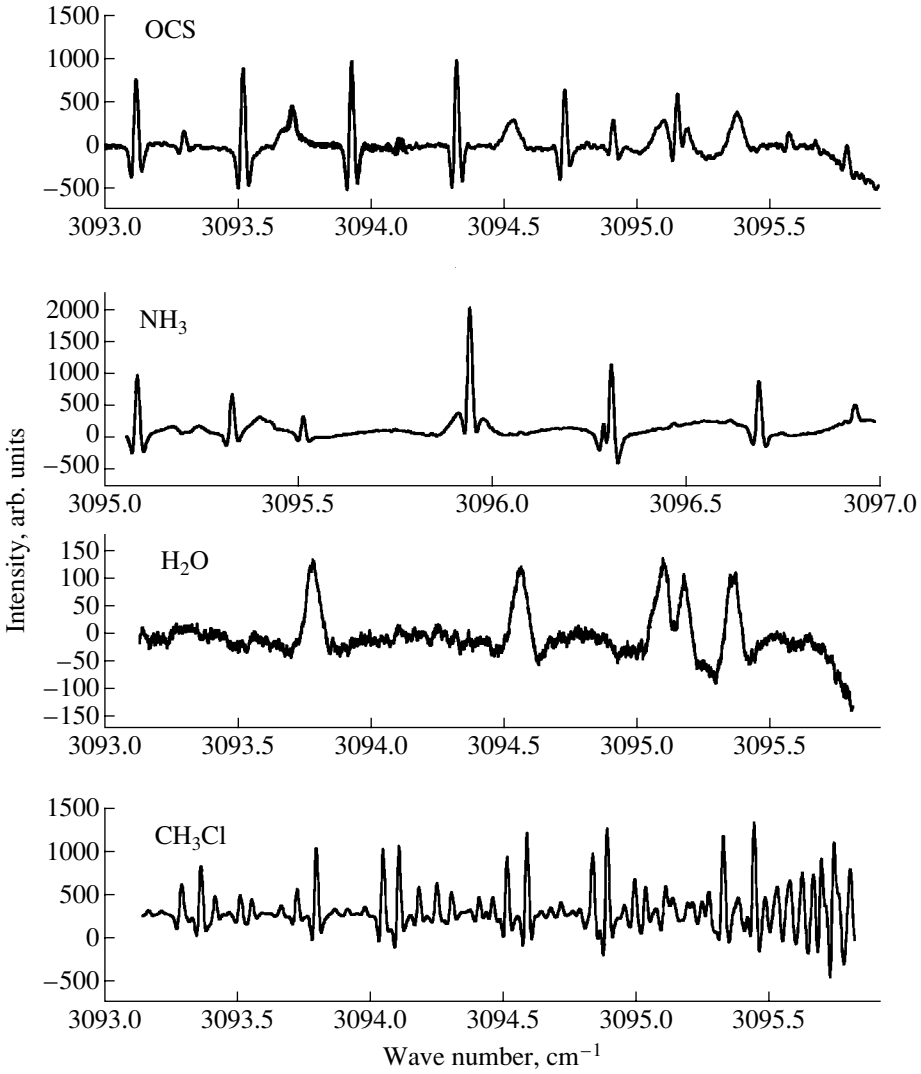

Fig. 15. Transmission spectra of OCS, NH_3, H_2O, and CH_3Cl gases recorded with laser beam scanning.

laser emission was single-mode in the temperature range 60–80 K, with the wave number tunable in the range 2–4 cm^{-1}. The achievement of single-mode, narrow-line emission from wide-cavity lasers demonstrates the high perfection of LPE-grown epitaxial layers and, owing to their high power and narrow emission line, makes lasers of this kind promising for spectroscopic applications. Our tunable lasers have been used to measure the absorption lines of quite a number of gases: N_2O [18], CH_3Cl [16, 18, 25, 26], H_2O [16, 18], OSC [16, 26], NH_3 [16]. Figure 15 shows the transmission spectra of OSC, NH_3, H_2O, and CH_3Cl.

5. CONCLUSION

Thus, we have fabricated and studied InAsSbP/InAsSb/InAsSbP double heterostructure lasers emitting at 3–4 μm. The laser spectrum can be tuned by varying the temperature and current. The emission wavelength increases with temperature almost linearly, $d\lambda/dT \approx 0.002$ μm/K. The mode wavelength changes by 0.5–1.0 cm^{-1} owing to the heating of the active region. The transmission spectra of methane and ethylene have been recorded using the lasers. The time of laser tuning by current is 10^{-8}–10^{-12} s; i.e., it is virtually instantaneous. The operation is single-mode in the range of currents $I/I_{th} = 1.15$–3 at temperatures of 12–90 K. The mode shift at $T = 77$ K is 50–60 Å, the maximum mode shift of 104 Å (10 cm^{-1}) being achieved at 62 K. An abnormally narrow directional pattern of emission in the *p–n* junction plane was observed in some of the lasers. The experimental data have been analyzed theoretically for lasers with a nonequilibrium carrier density that increases across the stripe from its center to its edges, with negligible spreading of carriers in the *p–n* junction plane. It is shown that, in such a laser, the light beam oscillates across the stripe width from one stripe edge to the other

and back. This effect gives rise to a tapered waveguide and results in the electromagnetic wave propagation constant becoming dependent on the relative excess of current over the threshold and on the squared amplitude of the electromagnetic wave. This reflects the nonlinearity of the laser's optical medium and allows tuning of the laser spectrum. The emission line width (FWHM) and its dependence on current have been studied. A line width of 10 MHz was attained in a laser with a wide (100 μm) cavity. The spectral line width is governed by fluctuations of the natural frequencies of the cavity, arising from fluctuations of the nonequilibrium carrier density. The lasers have been used for the scanning of OSC, NH_3, CH_3Cl, H_2O, and N_2O gas media.

ACKNOWLEDGMENTS

This study was supported by the Russian Foundation for Basic Research, project nos. 99-02-1809 and 00-02-17047.

REFERENCES

1. T. N. Danilova, A. N. Imenkov, V. V. Sherstnev, and Yu. P. Yakovlev, Fiz. Tekh. Poluprovodn. (St. Petersburg) **34** (11), 1396 (2000) [Semiconductors **34**, 1343 (2000)].
2. A. N. Baranov, T. N. Danilova, O. G. Ershov, *et al.*, Pis'ma Zh. Tekh. Fiz. **18** (22), 6 (1992) [Sov. Tech. Phys. Lett. **18**, 725 (1992)].
3. D. Z. Garbuzov, A. V. Tikunov, and V. B. Khalfin, Fiz. Tekh. Poluprovodn. (Leningrad) **21**, 1085 (1987) [Sov. Phys. Semicond. **21**, 662 (1987)].
4. Yu. P. Yakovlev, A. N. Baranov, A. N. Imenkov, *et al.*, Kvantovaya Élektron. (Moscow) **20**, 839 (1993).
5. P. G. Eliseev and A. P. Bogatov, Tr. Fiz. Inst. Akad. Nauk SSSR **116**, 15 (1986).
6. F. Stern, in *Radiative Recombination in Semiconductors: Proceedings of the 7th International Conference on Physics of Semiconductors, Paris, 1964* (Academic, New York, 1965), p. 165.
7. W. W. Anderson, IEEE J. Quantum Electron. **1**, 228 (1965).
8. P. P. Paskov, Solid State Commun. **82**, 739 (1992).
9. A. N. Baranov, T. N. Danilova, O. G. Ershov, *et al.*, Pis'ma Zh. Tekh. Fiz. **19** (17), 30 (1993) [Tech. Phys. Lett. **19**, 543 (1993)].
10. T. N. Danilova, A. P. Danilova, O. G. Ershov, *et al.*, Fiz. Tekh. Poluprovodn. (St. Petersburg) **32**, 373 (1998) [Semiconductors **32**, 339 (1998)].
11. A. P. Danilova, T. N. Danilova, A. N. Imenkov, *et al.*, Fiz. Tekh. Poluprovodn. (St. Petersburg) **33**, 1014 (1999) [Semiconductors **33**, 924 (1999)].
12. A. P. Astakhova, T. N. Danilova, A. N. Imenkov, *et al.*, Fiz. Tekh. Poluprovodn. (St. Petersburg) **34**, 1142 (2000) [Semiconductors **34**, 1100 (2000)].
13. A. P. Danilova, T. N. Danilova, A. N. Imenkov, *et al.*, Fiz. Tekh. Poluprovodn. (St. Petersburg) **33**, 1088 (1999) [Semiconductors **33**, 991 (1999)].
14. T. N. Danilova, A. P. Danilova, O. G. Ershov, *et al.*, Fiz. Tekh. Poluprovodn. (St. Petersburg) **31**, 1192 (1997) [Semiconductors **31**, 831 (1997)].
15. T. N. Danilova, A. P. Danilova, A. N. Imenkov, *et al.*, Pis'ma Zh. Tekh. Fiz. **25** (19), 17 (1999) [Tech. Phys. Lett. **25**, 766 (1999)].
16. A. P. Danilova, A. N. Imenkov, N. M. Kolchanova, *et al.*, Fiz. Tekh. Poluprovodn. (St. Petersburg) **34**, 243 (2000) [Semiconductors **34**, 237 (2000)].
17. A. P. Danilova, A. N. Imenkov, T. N. Danilova, *et al.*, Spectrochim. Acta A **55**, 2077 (1999).
18. S. Civis, A. N. Imenkov, A. P. Danilova, *et al.*, Spectrochim. Acta A **56**, 2125 (2000).
19. P. G. Eliseev and A. P. Bogatov, Kvantovaya Élektron. (Moscow) **10**, 826 (1983).
20. A. P. Danilova, A. N. Imenkov, N. M. Kolchanova, *et al.*, Fiz. Tekh. Poluprovodn. (St. Petersburg) **33**, 1469 (1999) [Semiconductors **33**, 1322 (1999)].
21. V. L. Bonch-Bruevich and S. G. Kalashnikov, in *Physics of Semiconductors* (Nauka, Moscow, 1977), p. 592.
22. T. N. Danilova, O. I. Evseenko, A. N. Imenkov, *et al.*, Pis'ma Zh. Tekh. Fiz. **22** (16), 7 (1996) [Tech. Phys. Lett. **22**, 645 (1996)].
23. T. N. Danilova, O. I. Evseenko, A. N. Imenkov, *et al.*, Pis'ma Zh. Tekh. Fiz. **24** (6), 77 (1998) [Tech. Phys. Lett. **24**, 239 (1998)].
24. A. P. Danilova, T. N. Danilova, A. N. Imenkov, *et al.*, Fiz. Tekh. Poluprovodn. (St. Petersburg) **33**, 243 (1999) [Semiconductors **33**, 210 (1999)].
25. A. N. Imenkov, N. M. Kolchanova, P. Kubat, *et al.*, Fiz. Tekh. Poluprovodn. (St. Petersburg) **34**, 1468 (2000) [Semiconductors **34**, 1406 (2000)].
26. A. N. Imenkov, N. M. Kolchanova, P. Kubat, *et al.*, Fiz. Tekh. Poluprovodn. (St. Petersburg) **35**, 375 (2001) [Semiconductors **35**, 360 (2001)].
27. C. H. Henry, IEEE J. Quantum Electron. **QE-18**, 259 (1982).
28. A. L. Schawlow and C. H. Tawnes, Phys. Rev. **112**, 1940 (1958).
29. D. Welford and A. Mooradian, Appl. Phys. Lett. **40**, 560 (1982).

Translated by D. Mashovets